

Nucleic Acid Analysis via Hybridization-Induced Microbead Aggregation:
Opportunities for Genetic Testing

Hillary Sally Sloane
Virginia Beach, VA

B.S., University of Virginia, 2011

A Dissertation presented to the Graduate Faculty
of the University of Virginia in Candidacy for the Degree of
Doctor of Philosophy

Department of Chemistry

University of Virginia
August, 2016

Abstract

The association of genetic alterations with disease onset, progression, and sensitivity to therapeutics has opened exciting opportunities for the implementation of a personalized model of patient care. The practical translation of these findings into our mainstream medical regime requires nucleic acid analysis technology that is affordable, time-efficient, and simple to execute. In an effort to provide an attractive alternative to conventional methods, which are typically unsuitable for routine scenarios, this work builds on a unique, bead-based technique for sequence-specific DNA detection known as Hybridization-Induced Aggregation (HIA). HIA involves a pair of magnetic bead-bound oligonucleotide probes designed to hybridize to a complementary target sequence. Upon target-probe hybridization, the beads become tethered together, resulting in optically-detectable bead aggregation.

Initially, analytical instrumentation, including a “dual-force aggregation” platform as well as a microdevice for integrated PCR amplification and HIA detection, were engineered to maximize the utility of bead aggregation assays in terms of throughput, speed, and sensitivity. In subsequent work, the HIA technique was exploited for the detection of single nucleotide polymorphisms. This was demonstrated for the detection of *KRAS* mutations in lung and colorectal cancers in order to predict patient sensitivity to epidermal growth factor receptor-targeted therapies. Additionally, HIA detection was combined with multiplex allele-specific PCR to detect three important mutations [*CYP2C9* *2, *CYP2C9* *3, and *VKORC1* (1173C>T)] that allow appropriate dosing of the

common oral anticoagulant, warfarin. Overall, this work represents practical steps forward in the development of nucleic acid analysis technology that is amenable for routine clinical care, in order to ultimately reap the rewards of a personalized medical regime.

Acknowledgements

I am profoundly grateful for the meaningful contributions made to this body of work, both direct and indirect, from a number of important people. Most notably, I thank my advisor, Dr. James Landers. It was his guidance and encouragement that initially led me to pursue my doctorate, and for that alone, I am immensely appreciative. I deeply value my experience in the Landers lab and the scientific intuition and diverse skill set this experience has cultivated. I thank Dr. Landers for allowing me to tailor my research to my interests and dig deep into the clinical applications of bioanalytical chemistry and microfluidics. I am also extremely grateful to Dr. Kim Kelly for welcoming me into her lab and fostering my interests in the biological sciences. I truly value my unique, interdisciplinary experience. I thank Dr. Bob Burnett and Dr. Tony Spano for their guidance throughout my time at UVA; they have both been integral in my higher education journey. To my peers in the both the Landers lab and the Kelly lab, past and present - I thank you all. Most notably, I thank Dr. Briony Strachan for her mentorship in my early years as a graduate student and her continued support. Additionally, I thank the undergraduate students I had the pleasure of working with - Jacob Lee, Daniel Miranian, Alexa Cecil, and Morgan Carter. Finally, to my friends and family - your unwavering support and encouragement have been invaluable. To my best friend, Lauren McQuillin, thank you for being there for me always. Ethan Caskey, thank you for standing by my side through the ups and downs of this process. To my sister, Krystina Stoner, and my dad, David Sloane - I am immensely grateful to have you both as my ultimate support

system. Dad - you are my rock, and there is no way to adequately express how much I
appreciate your steadfast support.

Dedication

This dissertation is dedicated to the loving memory of my mother, Julie Sloane. She is
my inspiration and my strength.

Table of Contents

Abstract.....	ii
Acknowledgements.....	iv
Dedication.....	v
Table of Contents.....	vi
List of Figures and Tables.....	x
Chapter 1: Introduction	1
1.1 Precision medicine	1
1.2 Traditional genotyping technologies (SNP genotyping).....	3
1.2.1 Allelic discrimination.....	5
1.2.1.1 Hybridization	7
1.2.1.2 Enzyme-assisted methods of allelic discrimination.....	8
1.2.1 Detection modalities	10
1.3 Point-of-care testing.....	13
1.3.1 Microfluidics: an enabling technology	15
1.4 Nucleic acid testing in a point-of-care format	17
1.4.1 Microfluidic DNA amplification.....	18
1.4.2 Microfluidic DNA hybridization.....	19
1.4.3 Microfluidic DNA detection	21
1.5 Concluding Remarks.....	24
1.6 References.....	25
Chapter 2: Engineering Technologies to Enable Particle-based, Optical DNA Detection	36
2.1 Overview.....	36
2.2 Part One: Dual force Aggregation System.....	38
2.2.1 Introduction.....	38
2.2.2 Materials and Methods.....	40
2.2.2.1 Reagents.....	40
2.2.2.2 Microwell fabrication.....	41
2.2.2.3 Device design.....	41
2.2.2.4 Reagent and sample preparation	42
2.2.2.5 Assay instrumentation.....	42
2.2.2.6 Assay protocol.....	43
2.2.3 Results and Discussion	43
2.2.3.1 The DFA system.....	43
2.2.3.2 Optimization of the DFA system for DNA quantification	45
2.2.3.4 λ -Phage DNA samples	50
2.2.3.5 Human genomic DNA samples.....	52
2.2.3.6 Comparing DFA to spectrophotometric methods	53

	vii
2.2.4 Conclusions.....	56
2.3 Part Two: Development of an Integrated Microdevice for DNA Amplification and Sequence-specific Detection	56
2.3.1 Introduction.....	56
2.3.2 Materials and Methods.....	61
2.3.2.1 Microdevice design.....	61
2.3.2.2 Fabrication of the microdevice, manifold, and rotating magnetic field construct.....	62
2.3.2.3 Reagents.....	63
2.3.2.4 Conjugating oligonucleotide probes to particles.....	63
2.3.2.5 PCR.....	64
2.3.2.6 Oligonucleotide sequences.....	64
2.3.2.7 Image analysis.....	64
2.3.3 Results and Discussion	65
2.3.3.1 Multiplexed IR-PCR.....	65
2.3.3.2 Torque actuated pressure (TAP) system for reagent delivery	66
2.3.3.3 Sealing and pressurization of the microdevice	69
2.3.3.4 Capillary burst valves	70
2.3.3.5 HIA Detection.....	72
2.3.3.6 Integrated amplification and detection of <i>Salmonella enterica</i>	73
2.3.4 Conclusions.....	75
2.4 Concluding Remarks.....	75
2.5 References.....	76

Chapter 3: Development of a Novel Analytical Strategy for Rapid <i>KRAS</i> Mutation Detection using Hybridization-Induced Aggregation	82
3.1 Overview.....	82
3.2 Introduction.....	83
3.3 Methods and Materials.....	90
3.3.1 Oligonucleotides	90
3.3.2 Cell lines and cDNA synthesis.....	90
3.3.3 Tumor samples	93
3.3.4 Sequencing.....	93
3.3.5 PCR.....	94
3.3.5.1 Initial PCR with version 1 primers	94
3.3.5.2 Real-time PCR and quantitative PCR.....	95
3.3.5.3 Optimized PCR for the generation of HIA _{MD} targets	95
3.3.6 Microdevice fabrication	96
3.3.7 HIA instrumentation.....	96
3.3.8 Bead preparation	96
3.3.9 Hybridization buffers	97
3.3.10 HIA _{MD} assays.....	97

	viii
3.3.10.1 Initial feasibility assays.....	98
3.3.10.2 HIA _{MD} studies performed under pre-optimized conditions	98
3.3.10.3 Effect of ionic strength.....	98
3.3.10.4 Optimization of buffer composition.....	98
3.3.10.5 Effect of target concentration.....	98
3.3.10.6 Reaction composition modifications.....	98
3.3.10.7 Final optimized HIA _{MD} reaction	99
3.4 Results and Discussion	99
3.4.1 Establishing initial feasibility	99
3.4.2 Generating the target sequence from biological samples	103
3.4.3 Probe design.....	108
3.4.4 Augmenting the instrumentation to provide temperature control	111
3.4.5 Buffer composition.....	114
3.4.6 Initial attempts with biological samples and subsequent adjustments..	118
3.4.7 <i>KRAS</i> mutation analysis of cancer cell lines.....	122
3.4.8 Resolution of mutant alleles in the background of wild-type DNA.....	124
3.4.9 <i>KRAS</i> mutation analysis of patient samples.....	125
3.4.10 Amplicon doublet phenomenon	129
3.5 Concluding Remarks.....	133
3.6 References.....	137

Chapter 4: Warfarin Genotyping with Hybridization-Induced Aggregation on a Poly(ethylene terephthalate) Microdevice146

4.1 Overview.....	146
4.2 Introduction.....	147
4.3 Materials and Methods.....	152
4.3.1 Oligonucleotides	152
4.3.2 Bead preparation	153
4.3.3 Patient samples.....	154
4.3.4 PCR (conventional).....	154
4.3.5 PCR (microchip)	154
4.3.6 Microchip electrophoresis.....	155
4.3.7 HIA instrumentation.....	155
4.3.7.1 DFA system.....	155
4.3.7.2 Spinning platform	156
4.3.8 Microdevice fabrication	156
4.3.8.1 PMMA device	156
4.3.8.2 PeT devices	157
4.3.9 Hybridization-induced Aggregation assays on a PMMA microdevice.	157
4.3.10 Hybridization-induced Aggregation assays on a PeT microdevice	158
4.3.10.1 HIA on PeT following conventional PCR	158
4.3.10.2 HIA on PeT following chip PCR	159

	ix
4.3.11 Image analysis/data analysis	159
4.4 Results and Discussion	159
4.4.1 Multiplex allele-specific PCR.....	159
4.4.2 Mutation detection with HIA	160
4.4.2.1 DFA system	162
4.4.2.2 PeT platform	163
4.4.3 Analysis of patient samples.....	170
4.4.4 Transitioning PCR onto a PeT chip: establishing proof-of-concept for integration	172
4.5 Concluding Remarks.....	176
4.6 References.....	178
Chapter 5: Final Remarks.....	182
5.1 Summary	182
5.2 Future Prospects.....	184
5.4 References.....	188

List of Figures and Tables

Chapter 1: Introduction

Figure 1-1 Opportunities for precision medicine.....	2
Figure 1-2 Principles underlying allelic discrimination.....	6
Figure 1-3 Principle of hybridization for SNP genotyping.....	7
Table 1-1 SNP genotyping platforms.....	13
Figure 1-4 Processes included in nucleic acid analysis	17
Table 1-2 Examples of bead-based hybridization assays.....	21
Figure 1-5 Magnetic bead-based hybridization assay using fluorescence detection.....	22
Figure 1-6 Magnetic bead-based hybridization assay using electrochemical detection.....	23
Figure 1-7 DNA detection based on aggregation of gold nanoparticles with DNA.....	24

Chapter 2: Engineering Technologies to Enable Particle-based, Optical DNA Detection

Figure 2-1 Proposed mechanism of chaotrope-driven aggregation (CDA)	39
Figure 2-2 Dark area analysis for DNA quantification.....	40
Figure 2-3 Multiplexing with RMF below device	44
Figure 2-4 Study of magnet height above device	46
Figure 2-5 Effects of individual forces	48
Figure 2-6 Dual force aggregation system.....	50
Figure 2-7 λ -Phage DNA standard curves	51
Figure 2-8 Human genomic DNA standard curves.....	53
Figure 2-9 Comparison of DFA to a fluorospectrophotometer	54
Table 2-1 Comparison of DFA to a fluorospectrophotometer.....	55
Figure 2-10 Proposed mechanism of hybridization-induced aggregation	59
Figure 2-11 Image of the integrated PMMA microdevice	61
Figure 2-12 Multiplex PCR with a halogen bulb.....	66
Figure 2-13 Demonstration of torque actuated fluid delivery	67
Figure 2-14 Top-view photographs of PCR chambers at 95°C	69
Figure 2-15 Capillary burst valve characterization.....	71
Figure 2-16 Placement of discrete individual magnetic field for HIA detection...	72
Figure 2-17 Integrated analysis for the detection of <i>Salmonella enterica</i>	74

Chapter 3: Development of a Novel Analytical Strategy for Rapid *KRAS* Mutation Detection using Hybridization-Induced Aggregation

Figure 3-1 The <i>KRAS</i> gene product functions as a GDP/GTP-regulated binary on-off switch	85
---	----

	xi
Figure 3-2 HIA assay principles	89
Table 3-1 Oligonucleotide sequences	91
Table 3-2 Cell lines	92
Figure 3-3 Detection of a 50-base target sequence with HIA.....	100
Figure 3-4 Detection of mismatch(s) in a 50-base target sequence	101
Figure 3-5 Optimization of the hybridization reaction time	102
Figure 3-6 Demonstrating initial feasibility of the HIA _{MD} method	103
Figure 3-7 PCR with version 1 primers to generate a 58 bp <i>KRAS</i> target for HIA _{MD} analysis.....	104
Figure 3-8 Melting curve analysis of PCR product with version 1 primers	105
Figure 3-9 Investigating the sequence fidelity of PCR product generated with version 1 primers.....	106
Figure 3-10 Quantitative PCR to determine concentration of first-strand <i>KRAS</i> cDNA	106
Figure 3-11 Real-time PCR with version 1 primers	107
Figure 3-12 PCR primers with version 2 primers to generate a 95 bp <i>KRAS</i> target for HIA _{MD} analysis.....	107
Figure 3-13 Real-time PCR with version 2 primers	108
Figure 3-14 Probe design.....	109
Figure 3-15 HIA _{MD} studies performed under pre-optimized conditions.....	111
Figure 3-16 Optimization of temperature-controlled HIA reactions using a PID- controlled resistive heater	112
Figure 3-17 Characterization of temperature homogeneity using a Peltier device	113
Table 3-3 Optimization parameters for Labview program.....	114
Figure 3-18 Effect of ionic strength.....	115
Table 3-4 Buffer composition	116
Figure 3-19 Optimization of buffer composition.....	116
Figure 3-20 Initial attempts with biological samples.....	118
Figure 3-21 Assay troubleshooting	119
Figure 3-22 Effect of target concentration	120
Figure 3-23 Reaction composition modifications.....	121
Figure 3-24 <i>KRAS</i> mutation analysis of cancer cell lines	124
Figure 3-25 Resolution of mutant DNA in a background of wild-type DNA.....	125
Figure 3-26 Representative sequencing results of 3 patient samples	126

Figure 3-27 HIA _{MD} results from <i>KRAS</i> mutation analysis of patient tissue samples.....	127
Table 3-3 Patient tumor samples.....	128
Figure 3-28 Amplicon doublet phenomenon — c.34G>T patient samples	130
Figure 3-29 Amplicon doublet phenomenon — wild-type patient samples	131
Figure 3-30 Amplicon doublet phenomenon — c.35G>A patient samples	133

Chapter 4: Warfarin Genotyping with Hybridization-Induced Aggregation on a Poly(ethylene terephthalate) Microdevice

Figure 4-1 Assay principles	152
Table 4-1 Oligonucleotide sequences	153
Figure 4-2 Validation of multiplex allele-specific PCR for warfarin genotyping.....	161
Figure 4-3 RMF speed optimization for HIA-based detection of <i>CYP2C9</i> *2.....	162
Figure 4-4 Warfarin genotyping assay on a PMMA microdevice with the DFA system	163
Figure 4-5 HIA PeT microdevice and instrumentation.....	164
Figure 4-6 Initial HIA studies on a PeT device.....	166
Figure 4-7 Exploring the effect of sample dilution on HIA results	167
Figure 4-8 Effect of adding formamide to the hybridization buffer	168
Figure 4-9 Optimized HIA-based warfarin genotyping assay on a PeT device ..	169
Figure 4-10 HIA-based genotyping of 23 patient samples	170
Table 4-2 Genotyping results of 23 patient samples.....	171
Figure 4-11 PeT microdevice for PCR.....	172
Figure 4-12 Thermal cycling profile for chip-based PCR	173
Figure 4-13 Validation of multiplex allele-specific PCR on a PeT microdevice.....	173
Figure 4-14 Initial HIA assay with PCR products generated on a PeT microdevice.....	174
Figure 4-15 Optimized HIA assay from PCR products generated on a PeT microdevice.....	175

1 Introduction

1.1 Precision medicine

Consider a paradigm in which the genetic information of an individual is strategically exploited to guide medical decisions. Imagine a regime where disease risk, progression, and response to therapeutics can be predicted with exceptional precision based on genetic characteristics. This vision, backed by key scientific and technological advances, is poised to transform our medical landscape from a reactive, “one-size-fits-all” system to an evidence-based, proactive, and, importantly, patient-centered model of care. This concept has historically been labeled as *personalized medicine*; however, this term was replaced by *precision medicine* in a 2011 report by the National Research Council (1), so as to avoid any inference that the intention was to create personalized medications (i.e., synthesize personalized therapeutics) for every individual.

The promise of precision medicine was largely born out of the successes of the Human Genome Project (HGP) (2). The HGP was the first large-scale project in biology and a pioneering effort of modern medicine, completed 50 years after Watson and Crick first described the fundamentals of the DNA double helix (3). With the elucidation of the human genome sequence, there emerged a new set of tools that could be used to identify sources of inter-individual variations, and further, understand the biological underpinnings of disease and its variability. Initially, genome-wide association (GWA) studies were launched, which made use of catalogued genetic variations to search for

common links in disease susceptibility (4). These studies led to the identification of causal genes for hereditary diseases, as well as possible genetic risk factors for certain diseases, such as diabetes, heart disease, and common cancers (5). Another consequence of the HGP was the increased understanding of diseases on an intricate molecular level. This provided a basis for the development of more effective, targeted therapeutics (6).

The overwhelming implications of precision medicine are evident when considering its application to multiple dimensions of clinical care (refer to **Fig. 1-1**). Genetic variants can be used to predict disease susceptibility (e.g., BRCA1/BRCA2 mutations to identify women with a high risk for breast or ovarian cancer (7)), which provides an opportunity to shift the current paradigm of care from disease treatment to disease prevention, when it is most cost-effective (2). Additionally, genetic markers can be applied for screening, diagnosis, prognosis, and monitoring of diseases. Perhaps one of the most exciting and promising applications of precision medicine is the ability to predict drug response based on genetic associations; this idea is known as

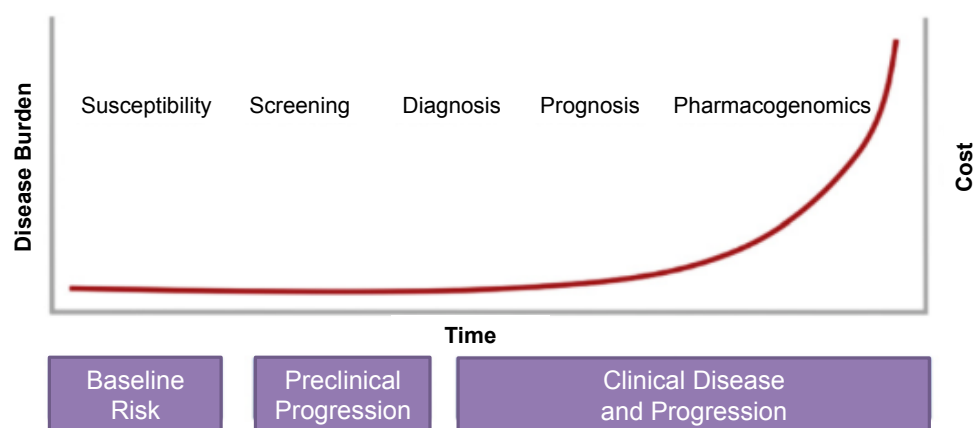


Figure 1-1. Opportunities for precision medicine. Diagram of the course of a disease over time (red curve), illustrating the opportunities (over time) to use various molecular and clinical tools to refine the risk of developing a disease, as well as screening, diagnosis, prognosis, and therapeutic selection. Adapted from Ginsburg and Willard (2).

pharmacogenetics (8). Important examples of pharmacogenetics in practice include predicting response to EGFR-mediated therapies in lung and colorectal cancers (9,10) (discussed further in **Chapter 3**) and dosing of the common oral anticoagulant warfarin (11) (discussed further in **Chapter 4**).

The concept of precision medicine has been championed for decades, from the initial plans for the HGP, through the genomic revolution born out of the HGP, to the endorsement of President Barak Obama in January 2015 in the form of the Precision Medicine Initiative (12). However, precision medicine remains largely an ideology rather than a practice. Of course, there have been iterative successes and steady progress, but the full realization of this regime is an audacious goal and faces complex challenges. Among these challenges are key ethical, social, legal, regulatory, and economic factors that will need to be addressed (13,14). Another important challenge, and relevant to the work presented in this dissertation, is the necessity for appropriate technologies and heuristics that will enable the practical translation of precision medicine into mainstream patient care. Although a daunting task, overcoming these challenges to realize the vision of precision medicine will undoubtedly revolutionize our medical landscape and has the potential to improve human health outcomes in unprecedented ways.

1.2 Traditional genotyping technologies (SNP detection)

A defining consequence of the HGP was the discovery of millions of DNA sequence variants in the human genome. Genetic variations take form as nucleotide insertions,

deletions, copy number variations, rearrangements, and, most commonly, Single Nucleotide Polymorphisms (SNPs). A SNP is a single nucleotide variation in the genome that is by definition found in more than 1% of the population (15). SNPs are the most abundant source of genetic variation (>95% of variants are SNPs) and occur in about 1 out of every 1,000 bases in the human genome (16,17). SNPs have been identified in GWA studies as important markers of disease onset, rate of progression, and therapeutic response (18). Because of the prevalence of SNPs and significance to precision medicine, genotyping technologies are discussed here with a focus on SNP analysis.

For this discussion, it is important to differentiate *genome-wide* genotyping from *targeted* genotyping. Genome-wide genotyping involves interrogation of the entire genome, or large sections of the genome, with whole-genome sequencing methods (including next-generation sequencing platforms) or high throughput DNA arrays. Targeted genotyping, on the other hand, provides detection of known genetic variations (at specific loci) with established disease associations. As of now, targeted genotyping will serve as the predominant mechanism for implementing precision medicine into mainstream clinical care. There are at least two fundamental reasons for this. First, even though the cost whole genome sequencing has dropped tremendously over time, it remains too expensive to be accessible or practical in routine scenarios (19). Second, whole genome sequencing is data overkill; at this point, we simply don't know what the vast majority of information derived from whole genome sequencing means. The data acquisition, processing, and storage is too complex, and indeed, not clinically useful, to

apply just yet (20). Thus, the focus in the context of this discussion is on targeted genotyping.

Detecting a single nucleotide variation in the 3 billion bases of the human genome is clearly a challenging task. As such, PCR (polymerase chain reaction), the technique that allows replication and amplification of a DNA sequence to billions-fold amplitude (21), is an indispensable tool for genotyping, as well as nearly all aspects of biological research. Truly, it is difficult to overstate the importance of PCR. While other DNA amplification formats have also been applied to genotyping methods, PCR is the basis for the overwhelming majority of traditional methods as well as developing techniques.

Following amplification, genotyping reactions require a form of allelic discrimination and detection. Allelic discrimination can be achieved during amplification (referred to as a homogenous assay), and detection can also be performed during amplification (referred to as real-time detection) (22). Following discussion of allelic discrimination approaches and detection modalities, examples of commercial platforms for SNP detection are summarized (**Table 1-1**).

1.2.1 Allelic discrimination

Allelic discrimination can be achieved using a hybridization-based approach or in enzyme-assisted formats, including primer extension, ligation, and enzymatic cleavage (**Fig. 1-2**).

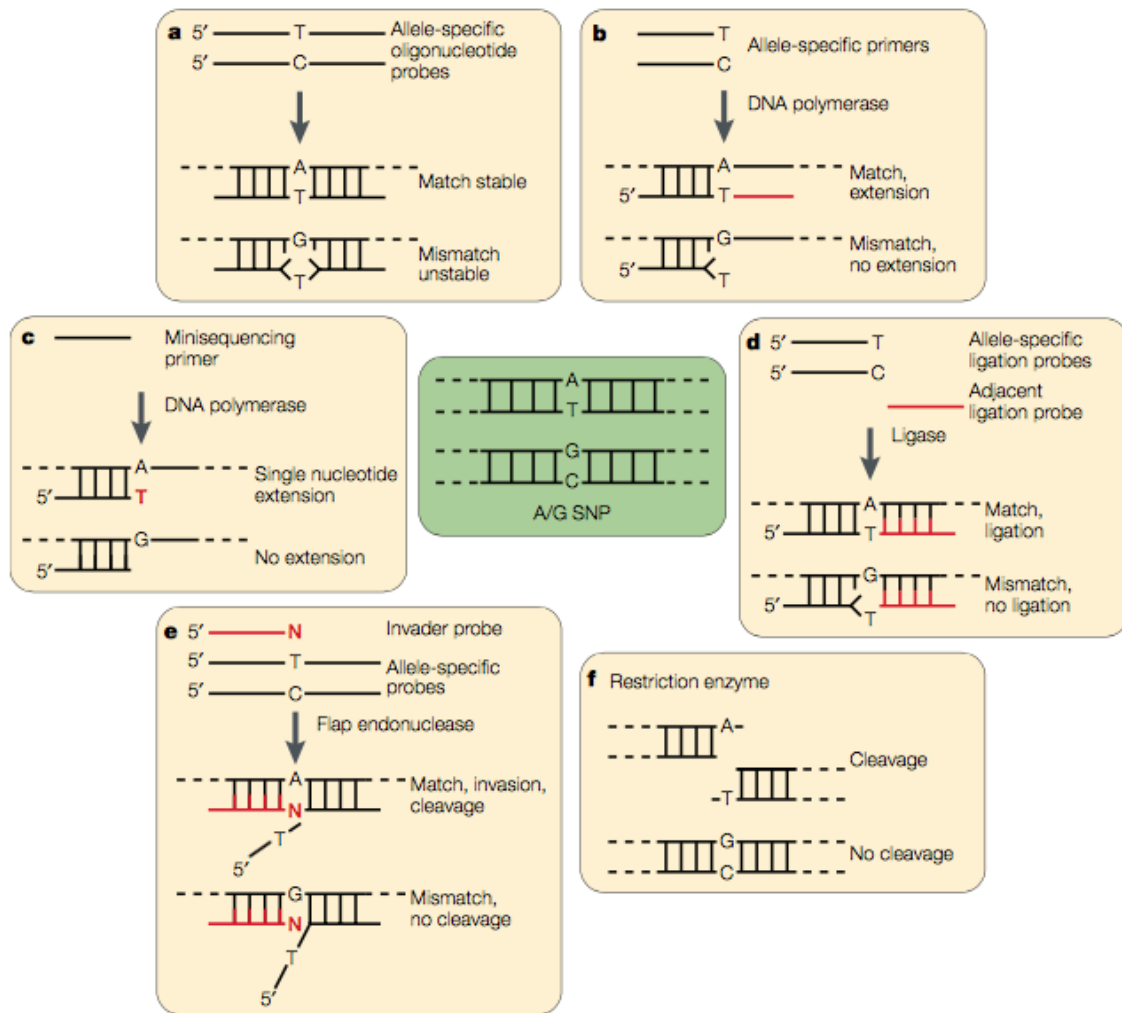


Figure 1-2. Principles underlying allelic discrimination for SNP genotyping. The panels illustrate detection of the A-allele of an A-to-G transition. *a*) Hybridization with allele-specific oligonucleotides. The hybridization of the A-allele to its complementary probe results in a stable complex; however, the mismatched target results in an unstable target-probe hybridization complex. *b*) Allele-specific primer extension. Only when the primer is perfectly matched to the target sequence at its 3' end will DNA polymerase extend the primer. *c*) Single nucleotide primer extension, or minisequencing. A primer that anneals to its target sequence immediately adjacent to a SNP site is extended by DNA polymerase with a single nucleotide that is complementary to the nucleotide at the SNP site. The identity of the extended nucleotide reveals the identity of the SNP. *d*) Oligonucleotide ligation. When an allele-specific probe is perfectly matched to the target sequence, it can be ligated to an adjacent ligation probe using DNA ligase. A mismatch between the allele-specific probe and the target will inhibit ligation. *e*) Invasive cleavage. When an allele-specific probe is perfectly matched to the target, its hybridization to the target, in combination with the hybridization of an invader probe, will form a three dimensional structure that results in cleavage of the 5' end of the allele-specific probe using FLAP endonuclease. *f*) Restriction site cleavage. When a SNP alters the recognition site of a particular restriction endonuclease, the target sequence will not be cleaved. Figure taken from Syvanen (22).

1.2.1.1 Hybridization

Hybridization-based SNP detection is based on the abilities of probe oligonucleotides to bind specifically and selectively with their complementary target nucleic acids to form a double-stranded hybrid molecule. Differences in the thermal stabilities of hybridization complexes allow discrimination

between perfectly matched and mismatched target-probe pairs (23) (**Fig. 1-2a** and **1-3**). The

thermal stability of the probe-target hybrid is affected not only

by the stringency of the reaction conditions, but also by the nucleotide sequence that flanks the SNP site, the secondary

structure of the target sequence, and the specifications of the probe sequence (24). When designing optimal probes for the detection of point mutations, several factors must be considered, including the length and sequence of the probe, as well as the location of the mismatch within the probe. As selectivity is also affected by the difference in kinetics of complex formation for perfectly-matched and mismatched duplexes, (25) the optimal hybridization reaction time must also be established. Although there is a great deal of knowledge about nucleic acid hybridization, the assay parameters that will allow the

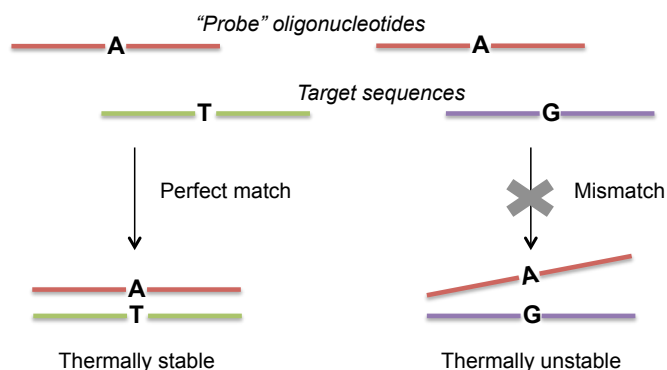


Figure 1-3. Principle of hybridization for SNP genotyping. Under optimized assay conditions, a target sequence bearing a single base mismatch will result in a target-probe hybridization complex that is thermally unstable; thus, the formation of the hybridization complex is unfavorable. This can be detected by a decrease in the analytical signal as compared to the perfectly matched target sequence.

optimal distinction between two target sequences that differ by a single nucleotide are difficult to predict and must be established empirically and separately for each SNP (26).

Hybridization fundamentals are important in nearly every form of allelic discrimination, in every instance where allele-specific probes or primers are used. Thus, understanding the dynamics of hybridization is critical for the development of genotyping technologies.

1.2.1.2 Enzyme-assisted methods of allelic discrimination

Enzyme-assisted methods for SNP genotyping include primer extension, ligation, and enzymatic cleavage. The various formats of the primer extension approach can be grouped into two categories: allele-specific nucleotide incorporation (also called single nucleotide extension, single base extension, or minisequencing) and allele-specific PCR. In the allele-specific PCR approach, a primer with its 3'-end complimentary to the SNP site is used in combination with a common reverse PCR primer (**Fig. 1-2b**) (27). The forward primer only gets extended by DNA polymerase if the nucleotide at its 3' end is perfectly complimentary to the SNP; thus, PCR product is only generated when the SNP is present. Allele-specific PCR can be performed in homogenous, real-time assays using intercalating dyes or labeled allele-specific PCR primers. Otherwise, a subsequent target-specific detection reaction or separation step is required. A limitation of allele-specific PCR is that, like hybridization-based assays, it requires fairly extensive empirical optimization for each SNP.

Allele-specific nucleotide incorporation relies on the high accuracy of nucleotide incorporation by DNA polymerases for genotype discrimination. A primer is designed to anneal with its 3' end adjacent to a SNP site, and the identity of the base incorporated, commonly determined by mass or fluorescence, reveals the SNP genotype (**Fig. 1-2c**) (28). Nucleotide incorporation boasts simple assay design and allows genotyping of multiple SNPs under the same conditions. A limitation of primer extension methods is that pre-assay PCR cleanup is critical, since both PCR and nucleotide incorporation reactions contain primers, nucleoside triphosphates and a DNA polymerase.

Ligation-based allelic discrimination involves three oligonucleotide probes – two allele-specific probes and a common probe. Upon hybridization of an allele-specific probe and the adjacent common probe, DNA ligase joins them together to form a single oligonucleotide; however, a mismatch at the junction between the two oligonucleotide probes inhibits ligation (**Fig. 1-2d**) (29). The allele-specific probes are commonly designed with its 3' end at the SNP site, as ligases are more sensitive to mismatches at the 3' end. The ligation product is detected using various means (e.g., fluorescence or size-based separation) to reveal the identity of the SNP.

Enzymatic cleavage can be used for allele discrimination when SNP sites are located in an enzyme recognition sequence and allelic differences affect recognition. The RFLP (restriction fragment length polymorphism) technique exploits restriction enzymes, which recognize particular sequences in double-stranded DNA and cleave both strands at a specific site in the sequence or near it to create shorter fragments (**Fig. 1-2f**) (30).

When a SNP is located in a restriction enzyme site, the target can be reacted with the corresponding restriction enzyme; the product is then separated so that the sizes of the products can be used to determine the genotype. With RFLP, no probes are required, which makes it fairly inexpensive; however, this technique is limited in throughput capabilities.

Another format of enzymatic cleavage for allelic discrimination is invasive cleavage, as used by the Invader[®] assay (Third Wave Technologies, WI). An allele-specific probe is used, which has a 5'-overhang region (i.e., region that is non-complimentary to the target sequence), in combination with an upstream invader probe (**Fig. 1-2e**) (31). Both probes hybridize to the target, and when the allele-specific probe is perfectly matched at the SNP site, the three-dimensional structure formed at the SNP site is recognized by a 5'-endonuclease, called a FLAP endonuclease. This enzyme cleaves the 5' overhang of the allele-specific probe at the SNP site, and released fragment is detected by fluorescence. While a distinct advantage of this method is that PCR amplification can be avoided, it also must be noted that a large amount of input DNA is required.

1.2.2 Detection modalities

Amplified product can be examined at the end of the amplification reaction (end-point detection) or while the reaction is progressing (real-time detection). Formats for detection include optical detection [i.e., fluorescence, (chemi)luminescence, and

absorbance (colorimetry)], electrochemical detection, and mass-based detection. Here, some of the common detection modalities used in genotyping reactions are briefly described. Additional biosensing technologies for nucleic acid detection are discussed in *Section 1.4.3, Microfluidic DNA detection*.

Fluorescence-based detection is the most commonly employed detection format in genotyping reactions. Fluorescence-based detection can take on many forms, including fluorescence polarization (32) and fluorescence resonance energy transfer (33). Fluorescence detection can be highly sensitive; however, complex laser optics and imaging components are required, making this strategy fairly expensive. Fluorescence detection can be monitored with the use of an intercalating dye to detect double-stranded DNA molecules; however, this detection format is non-specific. Alternatively, and more commonly, oligonucleotide probes, primers, or the DNA target itself are labeled with fluorescent tags to achieve sequence-specific detection. In this case, successful hybridization of a target to its probe results in an increase in fluorescence intensity.

Fluorescence detection is the basis for direct sequencing (i.e., Sanger sequencing), in which dideoxynucleotides are labeled with different fluorescent dyes and incorporated in a primer extension dideoxy chain termination reaction (34). The products are separated using capillary array electrophoresis, and the specific fluorescent signal from each extension product reveals the identity of the base. Sequential arrangement of the extension products decodes the template sequence. Direct sequencing was the workhorse for the HGP and initial GWA studies. This method is also useful for targeted SNP

genotyping; in fact, direct sequencing is considered to be the gold standard method in SNP genotyping.

Another optical detection modality involves chemiluminescence, which relies on the emission of light from chemical reactions possessing high quantum efficiency. A popular example of chemiluminescence detection in SNP genotyping is pyrosequencing. Pyrosequencing is a derivation of the allele-specific nucleotide incorporation approach, where primer extension is monitored by enzyme-mediated luminescence, which is released upon incorporation of deoxynucleotide triphosphates (35). Because the background is extremely low, chemiluminescence-based detection has the advantage of a high signal-to-noise ratio. However, the enzymatic reagents required can be costly.

An attractive alternative to optical detection methods is electrochemical detection. Electrochemical detection is typically carried out using oligonucleotides deposited on electrodes (36). The hybridization of a complimentary target sequence to the probe changes its electrical properties and therefore can be detected. This occurs optimally when an electroactive label is used.

Finally, mass spectrometry (MS) methods can be used for the detection of discriminated alleles, such as in primer extension reactions (37). Because MS measures the molecular weight of the products formed, direct detection can be achieved without the use of additional labels. High-resolution MS methods are sensitive enough to distinguish between DNA molecules that differ by a single base. A limitation to MS-based detection methods is the exquisite purity required of the sample product.

Name (company)	Reaction principle	Assay format, separation step	Detection method	References
MassEXTEND (Sequenom)	Single nucleotide primer extension	Solid-phase microparticles	Mass spectrometry	38,39
SNaPshot (Applied Biosystems)	Single nucleotide primer extension	Gel electrophoresis	Fluorescence	40,41
GeneChip (Affymetrix)	Hybridization with allele-specific probes	Solid-phase microarrays	Fluorescence	42,43
Dynamic allele-specific hybridization (DASH) (ThermoHybaid)	Hybridization with allele-specific probes	Semi-homogenous	Fluorescence	44
TaqMan assay (Applied Biosystems)	Hybridization with allele-specific probes	Solution-phase homogenous	Fluorescence resonance energy transfer	45,46
Invader assay (Third Wave Technologies)	Enzymatic cleavage	Solution-phase homogenous	Fluorescence resonance energy transfer	31
Pyrosequencing (Pyrosequencing AB)	Single nucleotide primer extension	Semi-homogenous	Chemiluminescence	47,35
BeadArray (Illumina)	Hybridization, primer extension, and ligation	Microbead-based array	Fluorescence	48
SNPlex (Applied Biosystems)	Hybridization and ligation	Gel electrophoresis	Fluorescence	49
Arrayed Primer Extension (APEX)	Single nucleotide primer extension	Solid-phase microarrays	Fluorescence	50
Tag-It (Tm Bioscience Corp)	Allele-specific primer extension	Flow cytometry	Fluorescence	51

Table 1-1. SNP genotyping platforms. Examples of technologies for SNP genotyping.

1.3 Point-of-care testing

Conventional methodologies for genetic analysis require expensive, technically sophisticated instrumentation and involve complicated, time-consuming processes that necessitate the expertise of trained personnel. This sort of testing format makes genetic analysis impractical for mainstream clinical care; thus, it represents a substantial barrier

in translating precision medicine tactics into our medical paradigm. As such, there has been a push in the field to shift the standard of testing from a centralized laboratory to the *point-of-care* (POC) (52, 53). POC testing, or “near patient” testing, refers to a format that provides rapid, ideally low cost, analysis with minimal instrumentation, and boasts simple operation and results interpretation. POC testing offers the ability to access and respond to results quickly and efficiently. By bringing the analysis closer to the patient, several processes are eliminated; samples are not sent to a secondary location where they await the attention of a skilled technician and results do not wait to be transmitted and acquired. Rather, the physician, caregiver, or even the patient themselves, can perform the test at the time of need. Thus, rapid time-to-result is a key advantage of POC testing and facilitates faster management response. Additionally, POC testing has significant cost reduction potential, as a result of decreased resource utilization (in terms of both equipment and personnel). Overall, increasing the time and cost efficiency of clinical testing through POC technology has the power to make testing more practical and accessible, such that all patients can reap the rewards of precision medicine tactics.

POC testing has been applied for a range of important analytes, including nucleic acids, proteins, metabolites, and whole cells (52). Perhaps the best-known protein-based POC device is the home pregnancy test for the detection of the pregnancy hormone human chorionic gonadotropin (hCG) (54). The home pregnancy test is an example of a lateral flow assay (LFA), which is among the most common POC testing formats today. LFAs are typically coupled with a visual read-out, obviating the need for any detection

instrumentation, and therefore serve as an ideal platform for POC device development. Another popular POC test, and the well-established leader in the POC market, is the glucose sensor, which is based on electrochemical detection of glucose oxidation (55). These early examples of applied POC technology have clearly demonstrated the practical benefits associated with the adoption of POC testing formats.

POC testing is particularly relevant for resource-limited areas and the developing the world (56). Although developing countries face high disease burden, they lack the sophisticated healthcare infrastructure including centralized laboratories, and are therefore burdened with high mortality rates. This has provided impetus for the development of POC devices in their simplest form that allow important analyses such as infectious disease detection.

The benefits of POC testing extend beyond the context of medical diagnostics. POC testing platforms have important implications for environmental monitoring (e.g., air, soil, and water contamination), food safety testing, and public security (e.g., detection of bioterrorism agents) (52). Thus, POC testing is relevant for a range of applications, and progress in POC technology development has the potential for widespread impact.

1.3.1 Microfluidics: an enabling technology

The power of microfluidics has been a driving force in the development of POC tests. As its name suggests, microfluidics is the science and technology of processing small amounts of fluids, with the use of micron-scale components (e.g., channels, pumps, and

valves) ranging from tens to hundreds of micrometers (57). Microfluidics offers important benefits including low sample and reagent requirements, low power consumption, small footprint/portability, rapid analysis, low cost, parallel processing capabilities, and functional integration of multiple processes (58). The defining characteristics of microfluidics and its associated advantages are so obviously suited for the ideals of POC testing.

The field of microfluidics was derived from the microelectronics industry, which provided strategies for miniaturization and microfabrication (57). With silicon micromachining technology as the foundation, the initial phase of microfluidic development involved silicon-based microdevices and components. However, silicon was phased out of continuing development due to the high cost, low biocompatibility, and opaque quality that precluded its use with optical detection methods. Microfabrication techniques were extended to glass, which was later displaced by polymers, including elastomers (e.g., PDMS) and hard plastics (e.g., PMMA). Polymer-based microdevices can be fabricated rapidly and inexpensively, using soft lithography, hot embossing and injection molding, as well as laser ablation, with bonding technologies such as adhesive, thermal, and plasma treatment bonding (52, 59). While polymer-based microdevices currently dominate the field, paper microdevices are becoming increasingly popular (60).

Because the inherent advantages of microfluidics align precisely with the goals of POC testing, the fields of microfluidics and POC testing have evolved in parallel. The

emergence of “lab-on-chip” systems to perform POC analyses, including the detection of clinical biomarkers (i.e., *molecular diagnostics*), has been extensive.

1.4 Nucleic acid testing in a point-of-care format

Given the significance of nucleic acid analysis in molecular diagnostics, including genotyping assays and other important applications such as infectious disease diagnosis, considerable effort has been focused on the development of POC-compatible nucleic acid testing (NAT) strategies. In fact, nucleic acid assays are the fastest growing component of biomedical diagnostics (52).

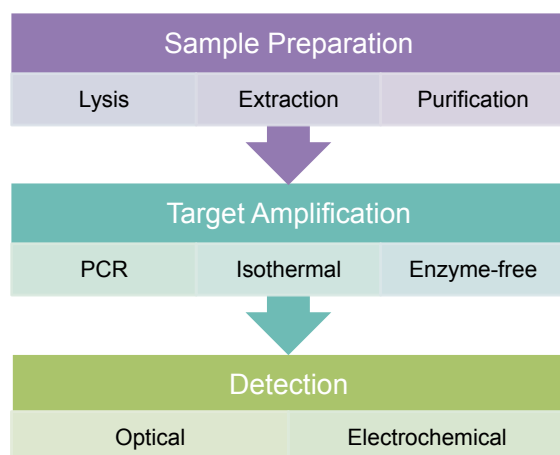


Figure 1-4. Processes included in nucleic acid analysis. Adapted from Hartman et al (61).

NAT comprises three core processes: sample preparation, amplification, and detection (**Fig. 1-4**) (61). For genotyping reactions, an allelic discrimination method is required after, or in concert with (homogenous format), amplification. The integration of all components on a single device for automated analysis with

“sample-in-answer-out” capabilities encompasses the vision of a micro total analysis system (μ TAS). While sample preparation is critical in preparing a raw sample (e.g., blood) for downstream analysis, the majority of innovation in the field has been directed toward amplification and detection strategies.

1.4.1 Microfluidic DNA amplification

The amount of nucleic acid content acquired from sample preparation or from the raw sample is typically insufficient for immediate detection, and therefore, a method of target amplification is required (62). There are a number of fundamental advantages to target DNA amplification. First, by increasing target concentrations with amplification, the sensitivity requirements of the downstream detection method are lessened. This is particularly important in POC scenarios, since the necessity for simpler instrumentation may compromise the detection sensitivity. Second, amplification introduces a level of sequence specificity to the assay. Third, increased target concentrations as a result of amplification enable faster kinetics for hybridization (the basis for allelic discrimination and/or detection in most NAT platforms), thus reducing the time-to-result (61).

Isothermal amplification techniques are attractive for microfluidic devices, since amplification occurs at a single constant temperature, which reduces the complexity of instrumentation required. Popular isothermal amplification methods include loop-mediated isothermal amplification (63), nucleic acid sequence-based amplification (64), rolling circle amplification (65), and helicase dependent amplification (66). These methods use enzymes to perform strand separation rather than relying on temperature increase for denaturation.

Among the various nucleic acid amplification techniques, PCR has been the most popular. Numerous on-chip PCR devices have been demonstrated, with thermal management provided by contact heaters such as thin film resistors, metal heating blocks,

and Peltier units, as well as non-contact heaters such as infrared-mediated and laser-assisted heating sources (67).

The implementation of DNA amplification onto a microfluidic platform introduces key advantages over conventional macro-scale methods (68). First, and perhaps most the obvious, is the decrease in sample and reagent requirements, which, in turn, decreases the cost of the assay. Additionally, faster amplification can be achieved in a microdevice. This is a result of enhanced kinetics as well as the characteristic high surface-to-volume ratio of a microfluidic reaction chamber, which allows efficient heat transfer and rapid thermal cycling.

1.4.2 Microfluidic DNA hybridization

DNA hybridization is the cornerstone of nucleic acid analysis. By transitioning DNA hybridization to a microfluidic platform, this technique becomes even more powerful; the micro-scale aspects allow increased hybridization efficiency, leading to better sensitivity, as well as enhanced kinetics, rendering a faster reaction time (69).

The immobilization of target-specific oligonucleotide probes onto a solid support serves as the basis for microarray technology. Microarrays are attractive methods for high-throughput mutation detection and have served as an indispensable tool for GWA studies. While the high-throughput capabilities are advantageous, there are limitations associated with the inherent set-up of a microarray. The complexity of the probe immobilization process increases the assay's cost and diminishes ease of operation.

Additionally, the hybridization reaction generally depends solely on the diffusion of target to surface-bound probes; this translates to a relatively long analysis time and necessity for large amounts of target DNA (70). These factors limit the usefulness of microarrays for targeted genotyping or other POC applications.

Micro- and nano-scale spherical particles (or beads), such as gold nanoparticles, polystyrene particles, latex beads, and liposomes have emerged as promising tools for DNA hybridization assays (78-82). The surface chemistry of many varieties of beads is conducive for simple conjugation to labeled oligonucleotide probes. For example, using streptavidin-coated beads allows simple immobilization of biotin-labeled oligonucleotides due to the favorable streptavidin-biotin interaction. Likewise, gold nanoparticles can be easily conjugated to oligonucleotides based on thiol chemistry. In addition to simplicity in probe immobilization, the use of probe functionalized beads has a number of advantages over typical microarray formats for DNA hybridization (69). In comparison to a traditional solid support on a flat surface or in a microfluidic channel, beads offer a significantly higher surface to volume ratio. This allows for a higher number of hybridization sites, and therefore enhanced sensitivity. Additionally, the inherent properties of the beads can be exploited for mixing or detection. For example, with the use of magnetic beads, an external magnetic source can be used for mixing within the hybridization channel or chamber (71, 72). The use of beads for detection is discussed in the following section. Examples of bead-based hybridization methods are listed in **Table 1-2**.

Bead type	Sample type	Hybridization time	Chip substrate	Detection method	Reference
Superparamagnetic beads and liposomes	RNA	20 min.	PDMS and PMMA	Fluorescence	73 (Fig. 1-5)
Paramagnetic beads	Synthetic DNA	90 min.	Commercial platform (DiagnoSwiss S.A.)	Electrochemical	74 (Fig. 1-6)
Carboxylated silica beads	Fluorescently-labeled DNA	1 h	Glass	Fluorescence	75
Paramagnetic beads	RNA	15 min	PDMS	Fluorescence	76
Magnetic beads	DNA	10 min	PDMS and glass	Absorbance/optical density analysis	77

Table 1-2. Examples of bead-based DNA hybridization assays. Adapted from Weng et al. (69)

1.4.3 Microfluidic DNA detection

DNA detection on a microfluidic platform has been demonstrated with the miniaturization of conventional techniques in addition to novel approaches. The greatest challenge has been in achieving appropriate detection sensitivity while eliminating the use of complicated and expensive peripheral instrumentation. Fluorescence is generally the most commonly employed method for DNA detection and has been applied in a number of microfluidic formats, including bead-based hybridization methods (for an example, see **Fig. 1-5**). While sensitive, fluorescence detection requires complex laser optics and imaging components, such as charge-coupled devices with large footprints; this presents a challenge for POC adaptation. Less expensive light emitting diodes and

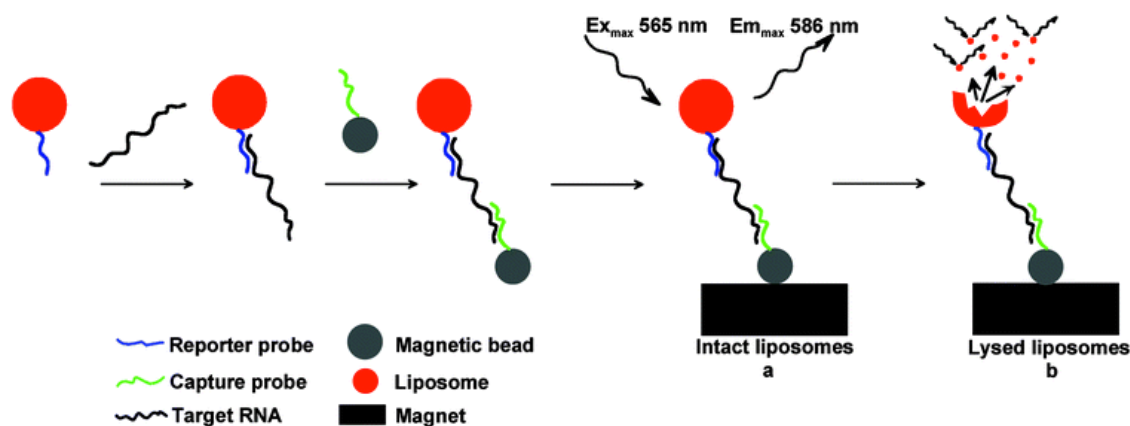


Figure 1-5. Magnetic bead-based hybridization method using fluorescence detection. A biotinylated capture probe was immobilized on streptavidin-coated superparamagnetic beads. A reporter probe was coupled to liposomes that encapsulated a fluorescent dye, sulforhodamine B. Target RNA was incubated with the bead-bound capture probes and liposome-bound reporter probes prior to introduction into a microchannel. The hybridization complexes were captured magnetically and detected with fluorescence via intact (a) and lysed (b) liposomes. Figure taken from Zaytseva et al. (73)

photodiodes have been used on POC platforms, although the illumination power, bandwidth, and detection sensitivity are limited compared to the conventional laser optic system. Electrochemical detection methods are popular, as the need for complex optics is obviated. An example of a hybridization-based assay exploiting electrochemical detection is depicted in **Figure 1-6**. While electrochemical detection provides an attractive alternative to fluorescence, this detection modality faces its own challenges such as incompatibility with high salt concentrations and high per-test costs, since electrodes are required to be integrated on each device. Indeed, translation of sensitive DNA sensing strategies that are compatible with the goals of POC testing represents a complex engineering challenge.

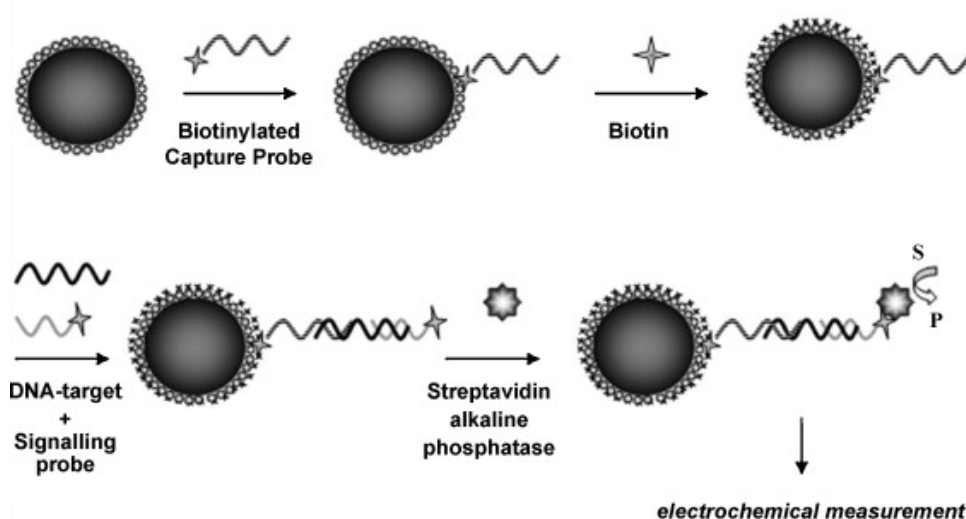


Figure 1-6. Magnetic bead-based hybridization method using electrochemical detection. Streptavidin-coated paramagnetic microparticles were functionalized with a biotinylated capture probe, and the remaining streptavidin sites were blocked with biotin. A complementary target sequence hybridized to the particle-bound capture probe as well as a biotinylated signaling probe. The resulting hybrid complex was labeled with a streptavidin alkaline phosphatase conjugate. The particles were then magnetically absorbed onto the working electrode. Subsequently, the electrochemical cell was covered with the substrate and the enzymatic product was measured. Figure taken from Berti et al. (74)

Creative biosensing strategies, including non-fluorescent optical detection methods have emerged as attractive alternatives to traditional approaches. Labels such as colloidal gold nanoparticles (GNPs) or dyed polystyrene or latex spheres can facilitate colorimetric detection (79). In many cases, visual detection can be achieved. GNPs are most commonly used in this format, and have been applied in lateral flow assays for nucleic acid detection. Additionally, GNP-DNA conjugates can be used in a sandwich hybridization assay to form GNP aggregates, as in the work demonstrated by Mirkin et al. (78, 80-82). The aggregation of the GNPs shifts the absorption peak toward a longer wavelength, resulting in a red-to-purple color change, which indicates the hybridization

event (**Fig. 1-7**). The simplicity in read-out and results interpretation makes visual detection ideal for POC platforms.

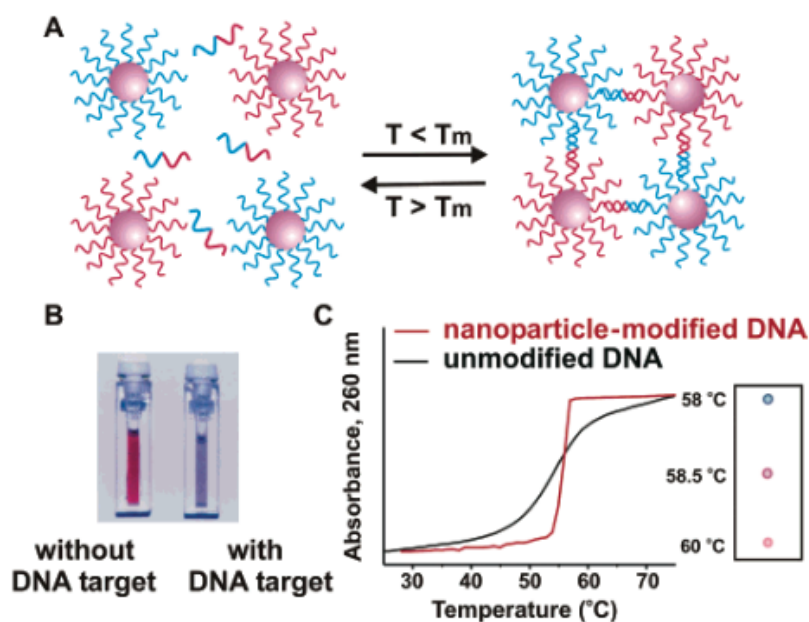


Figure 1-7. DNA detection based on aggregation of gold nanoparticles (GNPs) with DNA. Complimentary DNA targets will hybridize to oligonucleotide-conjugated GNPs to form aggregates (A), resulting in a change in solution color from red to blue (B). The aggregation process can be monitored using UV-vis spectroscopy or by spotting the solution on a silica support (C). Figure taken from Elghanian et al. (80)

1.5 Concluding Remarks

The challenge is on to find innovative ways to integrate genetic testing into mainstream clinical care, such that the ideals of precision medicine can finally be realized. POC technology offers the opportunity to make genetic testing and other analytical techniques practical and accessible, overcoming the barriers associated conventional lab-based testing. Catalyzed by advances in the field of microfluidics, exciting progress in the

development of POC-compatible testing platforms has been made. However, there remains extensive work to be done. Most POC devices still require expensive, bulky peripheral equipment and are associated with complex and/or time-consuming operation procedures. In other cases, the analytical performance (e.g., limit of detection and reproducibility) is inadequate. Herein lies the central conundrum of POC technology development. POC tests are expected to be rapid, inexpensive, and technically undemanding, while providing accurate and reliable results comparable to the conventional technique they are intended to replace.

As the search for innovative technologies that allow us to “have it all” (i.e., simplicity *and* sensitivity) continues, we must move forward by designing testing strategies with the intended application in mind and evaluate these methods in terms of the clinical need. To maximize simplicity, we must consider the minimum analytical specifications necessary to deliver an actionable result.

The work presented in this dissertation is intended to address some of the technical challenges associated with developing adequate analytical methods that are appropriate for use at the POC. The successes described here represent practical steps forward in the grandiose effort of facilitating a patient-centered model of patient care.

1.6 References

1. Toward precision medicine: building a knowledge network for biomedical research and a new taxonomy of disease. National Academies Press (US); 2011

2. Ginsburg GS, Willard HF. Genomic and personalized medicine: foundations and applications. *Transl Res*. 2009;154:277-87.
3. Watson JD, Crick FHC. Molecular structure of nucleic acids. *Nature*. 1953;171:737-8.
4. Chen R, Snyder M. Promise of personalized omics to precision medicine. *Wiley Interdiscip Rev Syst Biol Med*. 2013;5:73-82.
5. Manolio TA, Brooks LD, Collins FS. A HapMap harvest of insights into the genetics of common disease. *The Journal of clinical investigation*. 2008;118:1590-605.
6. Ginsburg GS, McCarthy JJ. Personalized medicine: revolutionizing drug discovery and patient care. *TRENDS in Biotechnology*. 2001;19:491-6.
7. Schwartz GF, Hughes KS, Lynch HT, Fabian CJ, Fentiman IS, Robson ME, Domchek SM, Hartmann LC, Holland R, Winchester DJ. Proceedings of the international consensus conference on breast cancer risk, genetics, & risk management, April, 2007. *The breast journal*. 2009;15:4-16.
8. Relling MV, Evans WE. Pharmacogenomics in the clinic. *Nature*. 2015;526:343-50.
9. Califano R, Landi L, Cappuzzo F. Prognostic and predictive value of K-RAS mutations in non-small cell lung cancer. *Drugs*. 2012;72 Suppl 1:28-36.
10. Baynes RD, Gansert J. KRAS mutational status as a predictor of epidermal growth factor receptor inhibitor efficacy in colorectal cancer. *Am J Ther*. 2009;16:554-61.
11. Johnson JA, Cavallari LH. Warfarin pharmacogenetics. *Trends Cardiovasc Med*. 2015;25:33-41.

12. Obama precision medicine initiative. In press
13. Collins FS, Green ED, Guttmacher AE, Guyer MS. A vision for the future of genomics research. *Nature*. 2003;422:835-47.
14. Hood L, Flores M. A personal view on systems medicine and the emergence of proactive P4 medicine: predictive, preventive, personalized and participatory. *N Biotechnol*. 2012;29:613-24.
15. Brookes AJ. The essence of SNPs. *Gene*. 1999;234:177-86.
16. Wang DG, Fan JB, Siao CJ, Berno A, Young P, Sapolsky R, Ghandour G, Perkins N, Winchester E, Spencer J, Kruglyak L, Stein L, Hsie L, Topaloglou T, Hubbell E, Robinson E, Mittmann M, Morris MS, Shen N, Kilburn D, Rioux J, Nusbaum C, Rozen S, Hudson TJ, Lipshutz R, Chee M, Lander ES. Large-scale identification, mapping, and genotyping of single-nucleotide polymorphisms in the human genome. *Science*. 1998;280:1077-82.
17. Sachidanandam R, Weissman D, Schmidt SC, Kakol JM, Stein LD, Marth G, Sherry S, Mullikin JC, Mortimore BJ, Willey DL, Hunt SE, Cole CG, Coggill PC, Rice CM, Ning Z, Rogers J, Bentley DR, Kwok PY, Mardis ER, Yeh RT, Schultz B, Cook L, Davenport R, Dante M, Fulton L, Hillier L, Waterston RH, McPherson JD, Gilman B, Schaffner S, Van Etten WJ, Reich D, Higgins J, Daly MJ, Blumenstiel B, Baldwin J, Stange-Thomann N, Zody MC, Linton L, Lander ES, Altshuler D. A map of human genome sequence variation containing 1.42 million single nucleotide polymorphisms. *Nature*. 2001;409:928-33.

18. Yu W, Yesupriya A, Wulf A, Hindorff LA, Dowling N, Khoury MJ, Gwinn M. GWAS Integrator: a bioinformatics tool to explore human genetic associations reported in published genome-wide association studies. *Eur J Hum Genet*. 2011;19:1095-9.
19. Alyass A, Turcotte M, Meyre D. From big data analysis to personalized medicine for all: challenges and opportunities. *BMC Med Genomics*. 2015;8:33.
20. Guarnaccia M, Gentile G, Alessi E, Schneider C, Petralia S, Cavallaro S. Is this the real time for genomics? *Genomics*. 2014;103:177-82.
21. Mullis KB, Faloona FA. Specific synthesis of DNA in vitro via a polymerase-catalyzed chain reaction. *Methods Enzymol*. 1987;155:335-50.
22. Syvänen A-C. Accessing genetic variation: genotyping single nucleotide polymorphisms. *Nature Reviews Genetics*. 2001;2:930-42.
23. Zhang DY, Chen SX, Yin P. Optimizing the specificity of nucleic acid hybridization. *Nat Chem*. 2012;4:208-14.
24. Kabilov MR, Pyshnyi DV. Analytical consideration of the selectivity of oligonucleotide hybridization. *Journal of Biophysical Chemistry*. 2011;2:75.
25. Tsourkas A, Behlke MA, Rose SD, Bao G. Hybridization kinetics and thermodynamics of molecular beacons. *Nucleic Acids Res*. 2003;31:1319-30.
26. SantaLucia Jr J, Hicks D. The thermodynamics of DNA structural motifs. *Annu Rev Biophys Biomol Struct*. 2004;33:415-40.
27. Gibbs RA, Nguyen P-N, Caskey CT. Detection of single DNA base differences by competitive oligonucleotide priming. *Nucleic acids research*. 1989;17:2437-48.

28. Sokolov BP. Primer extension technique for the detection of single nucleotide in genomic DNA. *Nucleic Acids Res.* 1990;18:3671.
29. Landegren U, Kaiser R, Sanders J, Hood L. A ligase-mediated gene detection technique. *Science.* 1988;241:1077-80.
30. Botstein D, White RL, Skolnick M, Davis RW. Construction of a genetic linkage map in man using restriction fragment length polymorphisms. *American journal of human genetics.* 1980;32:314.
31. Lyamichev V, Mast AL, Hall JG, Prudent JR, Kaiser MW, Takova T, Kwiatkowski RW, Sander TJ, de Arruda M, Arco DA. Polymorphism identification and quantitative detection of genomic DNA by invasive cleavage of oligonucleotide probes. *Nature biotechnology.* 1999;17:292-6.
32. Chen X, Levine L, Kwok PY. Fluorescence polarization in homogeneous nucleic acid analysis. *Genome Res.* 1999;9:492-8.
33. Tyagi S, Bratu DP, Kramer FR. Multicolor molecular beacons for allele discrimination. *Nat Biotechnol.* 1998;16:49-53.
34. Sanger F, Nicklen S, Coulson AR. DNA sequencing with chain-terminating inhibitors. *Proc Natl Acad Sci U S A.* 1977;74:5463-7.
35. Ronaghi M, Karamohamed S, Pettersson B, Uhlen M, Nyren P. Real-time DNA sequencing using detection of pyrophosphate release. *Anal Biochem.* 1996;242:84-9.

36. Wang J, Cai X, Rivas G, Shiraishi H, Dontha N. Nucleic-acid immobilization, recognition and detection at chronopotentiometric DNA chips. *Biosens Bioelectron.* 1997;12:587-99.
37. Tost J, Gut IG. Genotyping single nucleotide polymorphisms by mass spectrometry. *Mass Spectrom Rev.* 2002;21:388-418.
38. Braun A, Little DP, Köster H. Detecting CFTR gene mutations by using primer oligo base extension and mass spectrometry. *Clinical chemistry.* 1997;43:1151-8.
39. Cashman JR, Zhang J, Leushner J, Braun A. Population distribution of human flavin-containing monooxygenase form 3: gene polymorphisms. *Drug metabolism and disposition.* 2001;29:1629-37.
40. Le Hellard S, Ballereau SJ, Visscher PM, Torrance HS, Pinson J, Morris SW, Thomson ML, Semple CA, Muir WJ, Blackwood DH, Porteous DJ, Evans KL. SNP genotyping on pooled DNAs: comparison of genotyping technologies and a semi automated method for data storage and analysis. *Nucleic Acids Res.* 2002;30:e74.
41. Sanchez JJ, Borsting C, Hallenberg C, Buchard A, Hernandez A, Morling N. Multiplex PCR and minisequencing of SNPs--a model with 35 Y chromosome SNPs. *Forensic Sci Int.* 2003;137:74-84.
42. Kennedy GC, Matsuzaki H, Dong S, Liu WM, Huang J, Liu G, Su X, Cao M, Chen W, Zhang J, Liu W, Yang G, Di X, Ryder T, He Z, Surti U, Phillips MS, Boyce-Jacino MT, Fodor SP, Jones KW. Large-scale genotyping of complex DNA. *Nat Biotechnol.* 2003;21:1233-7.

43. Matsuzaki H, Loi H, Dong S, Tsai YY, Fang J, Law J, Di X, Liu WM, Yang G, Liu G, Huang J, Kennedy GC, Ryder TB, Marcus GA, Walsh PS, Shriver MD, Puck JM, Jones KW, Mei R. Parallel genotyping of over 10,000 SNPs using a one-primer assay on a high-density oligonucleotide array. *Genome Res.* 2004;14:414-25.
44. Prince JA, Feuk L, Howell WM, Jobs M, Emahazion T, Blennow K, Brookes AJ. Robust and accurate single nucleotide polymorphism genotyping by dynamic allele-specific hybridization (DASH): design criteria and assay validation. *Genome Res.* 2001;11:152-62.
45. Livak KJ, Flood SJ, Marmaro J, Giusti W, Deetz K. Oligonucleotides with fluorescent dyes at opposite ends provide a quenched probe system useful for detecting PCR product and nucleic acid hybridization. *PCR Methods Appl.* 1995;4:357-62.
46. Livak KJ. Allelic discrimination using fluorogenic probes and the 5' nuclease assay. *Genet Anal.* 1999;14:143-9.
47. Nyren P, Pettersson B, Uhlen M. Solid phase DNA minisequencing by an enzymatic luminometric inorganic pyrophosphate detection assay. *Anal Biochem.* 1993;208:171-5.
48. Oliphant A, Barker DL, Stuelpnagel JR, Chee MS. BeadArray technology: enabling an accurate, cost-effective approach to high-throughput genotyping. *Biotechniques.* 2002;32:56-8.
49. Tobler AR, Short S, Andersen MR, Paner TM, Briggs JC, Lambert SM, Wu PP, Wang Y, Spoonde AY, Koehler RT. The SNPlex genotyping system: a flexible and

- scalable platform for SNP genotyping. *Journal of biomolecular techniques: JBT*. 2005;16:398.
50. Shumaker JM, Metspalu A, Caskey CT. Mutation detection by solid phase primer extension. *Hum Mutat*. 1996;7:346-54.
 51. Bortolin S, Black M, Modi H, Boszko I, Kobler D, Fieldhouse D, Lopes E, Lacroix JM, Grimwood R, Wells P, Janeczko R, Zastawny R. Analytical validation of the tag-it high-throughput microsphere-based universal array genotyping platform: application to the multiplex detection of a panel of thrombophilia-associated single-nucleotide polymorphisms. *Clin Chem*. 2004;50:2028-36.
 52. Gubala V, Harris LF, Ricco AJ, Tan MX, Williams DE. Point of care diagnostics: status and future. *Anal Chem*. 2012;84:487-515.
 53. Jani IV, Peter TF. How point-of-care testing could drive innovation in global health. *N Engl J Med*. 2013;368:2319-24.
 54. Vaitukaitis JL, Braunstein GD, Ross GT. A radioimmunoassay which specifically measures human chorionic gonadotropin in the presence of human luteinizing hormone. *Am J Obstet Gynecol*. 1972;113:751-8.
 55. Heller A, Feldman B. Electrochemical glucose sensors and their applications in diabetes management. *Chem Rev*. 2008;108:2482-505.
 56. Sharma S, Zapatero-Rodriguez J, Estrela P, O'Kennedy R. Point-of-Care Diagnostics in Low Resource Settings: Present Status and Future Role of Microfluidics. *Biosensors (Basel)*. 2015;5:577-601.

57. Whitesides GM. The origins and the future of microfluidics. *Nature*. 2006;442:368-73.
58. Sia SK, Kricka LJ. Microfluidics and point-of-care testing. *Lab Chip*. 2008;8:1982-3.
59. Kumar S, Kumar S, Ali MA, Anand P, Agrawal VV, John R, Maji S, Malhotra BD. Microfluidic-integrated biosensors: prospects for point-of-care diagnostics. *Biotechnol J*. 2013;8:1267-79.
60. Meredith NA, Quinn C, Cate DM, Reilly TH, Volckens J, Henry CS. Paper-based analytical devices for environmental analysis. *Analyst*. 2016;141:1874-87.
61. Hartman MR, Ruiz RC, Hamada S, Xu C, Yancey KG, Yu Y, Han W, Luo D. Point-of-care nucleic acid detection using nanotechnology. *Nanoscale*. 2013;5:10141-54.
62. Lee TM, Hsing IM. DNA-based bioanalytical microsystems for handheld device applications. *Anal Chim Acta*. 2006;556:26-37.
63. Notomi T, Okayama H, Masubuchi H, Yonekawa T, Watanabe K, Amino N, Hase T. Loop-mediated isothermal amplification of DNA. *Nucleic Acids Res*. 2000;28:E63.
64. Compton J. Nucleic acid sequence-based amplification. *Nature*. 1991;350:91-2.
65. Lizardi PM, Huang X, Zhu Z, Bray-Ward P, Thomas DC, Ward DC. Mutation detection and single-molecule counting using isothermal rolling-circle amplification. *Nat Genet*. 1998;19:225-32.
66. Vincent M, Xu Y, Kong H. Helicase-dependent isothermal DNA amplification. *EMBO Rep*. 2004;5:795-800.

67. Zhang C, Xing D. Miniaturized PCR chips for nucleic acid amplification and analysis: latest advances and future trends. *Nucleic Acids Res.* 2007;35:4223-37.
68. Chen L, Manz A, Day PJ. Total nucleic acid analysis integrated on microfluidic devices. *Lab Chip.* 2007;7:1413-23.
69. Weng X, Jiang H, Li D. Microfluidic DNA hybridization assays. *Microfluidics and nanofluidics.* 2011;11:367-83.
70. Henry OYF, O'Sullivan CK. Rapid DNA hybridization in microfluidics. *TrAC Trends in Analytical Chemistry.* 2012;33:9-22.
71. Lee SH, van Noort D, Lee JY, Zhang B-T, Park TH. Effective mixing in a microfluidic chip using magnetic particles. *Lab on a Chip.* 2009;9:479-82.
72. Leslie DC, Li J, Strachan BC, Begley MR, Finkler D, Bazydlo LAL, Barker NS, Haverstick DM, Utz M, Landers JP. New detection modality for label-free quantification of DNA in biological samples via superparamagnetic bead aggregation. *Journal of the American Chemical Society.* 2012;134:5689-96.
73. Kwakye S, Baeumner A. A microfluidic biosensor based on nucleic acid sequence recognition. *Anal Bioanal Chem.* 2003;376:1062-8.
74. Berti F, Laschi S, Palchetti I, Rossier JS, Reymond F, Mascini M, Marrazza G. Microfluidic-based electrochemical genosensor coupled to magnetic beads for hybridization detection. *Talanta.* 2009;77:971-8.
75. Senapati S, Mahon AR, Gordon J, Nowak C, Sengupta S, Powell TH, Feder J, Lodge DM, Chang HC. Rapid on-chip genetic detection microfluidic platform for real world applications. *Biomicrofluidics.* 2009;3:22407.

76. Zaytseva NV, Goral VN, Montagna RA, Baeumner AJ. Development of a microfluidic biosensor module for pathogen detection. *Lab Chip*. 2005;5:805-11.
77. Wang CH, Lien KY, Wu JJ, Lee GB. A magnetic bead-based assay for the rapid detection of methicillin-resistant *Staphylococcus aureus* by using a microfluidic system with integrated loop-mediated isothermal amplification. *Lab Chip*. 2011;11:1521-31.
78. Storhoff JJ, Elghanian R, Mucic RC, Mirkin CA, Letsinger RL. One-pot colorimetric differentiation of polynucleotides with single base imperfections using gold nanoparticle probes. *Journal of the American Chemical Society*. 1998;120:1959-64.
79. Sato K, Hosokawa K, Maeda M. Colorimetric biosensors based on DNA-nanoparticle conjugates. *Anal Sci*. 2007;23:17-20.
80. Elghanian R, Storhoff JJ, Mucic RC, Letsinger RL, Mirkin CA. Selective colorimetric detection of polynucleotides based on the distance-dependent optical properties of gold nanoparticles. *Science*. 1997;277:1078-81.
81. Demers LM, Mirkin CA, Mucic RC, Reynolds RA, Letsinger RL, Elghanian R, Viswanadham G. A fluorescence-based method for determining the surface coverage and hybridization efficiency of thiol-capped oligonucleotides bound to gold thin films and nanoparticles. *Anal Chem*. 2000;72:5535-41.
82. Storhoff JJ, Lazarides AA, Mucic RC, Mirkin CA, Letsinger RL, Schatz GC. What controls the optical properties of DNA-linked gold nanoparticle assemblies? *Journal of the American Chemical Society*. 2000;122:4640-50.

2 Engineering Technologies to Enable Particle-based, Optical DNA Detection

2.1 Overview

The work presented in this chapter expands upon previous efforts in the development of novel methods for sequence-specific DNA detection (Hybridization-Induced Aggregation, HIA) and sequence-independent genomic DNA quantification (Chaotrope-Driven Aggregation, CDA) (1). Both methods rely on the interaction of DNA with superparamagnetic beads in a rotating magnetic field (RMF) to produce multi-particle aggregates that are visually striking, allowing simple optical detection of the DNA.

Part one: Development of a dual force aggregation system describes the development and optimization of an innovative system that facilitates multiplex processing of CDA and HIA assays for the first time. Previously, CDA and HIA assays were performed using a set-up that permitted effective aggregation in only a single microwell at the center of the RMF. In multi-sample analysis, it was required that each reaction well be exposed to the center of the RMF in a serial manner; thus, the process was tedious, time-consuming and labor-intensive. For a more efficient approach, a unique system was developed, which incorporates agitation as a second force to work in concert with the RMF. Ultimately, this Dual-Force Aggregation (DFA) system allows effective simultaneous aggregation in multiple wells on a single device. The DFA technology for DNA quantification with the CDA assay is investigated in detail in this

chapter, while the transition of the HIA assay onto the DFA system is described in **Chapters 3 and 4** in the context of clinical applications.

It is shown here that the DFA approach allows 12 samples to be interrogated for DNA content in 140 seconds; this provides a ~35-fold improvement in time compared to the previous single-plex approach (80 min) and ~4-fold improvement over conventional fluorospectrometer methods. Furthermore, the increased interaction between DNA and beads provided by DFA improves the limit of detection (LOD) by roughly an order of magnitude (from 4 pg/ μ L to 250 fg/ μ L). The correlation between the DFA results and those from a fluorospectrometer highlight DFA as an inexpensive and rapid alternative to conventional methods.

In Part two: Development of an integrated microdevice for DNA amplification and sequence-specific detection, a microdevice is developed that allows functional integration of HIA detection with upstream infrared-mediated PCR amplification. With this device, visual DNA detection for specific detection of bacterial targets (from purified DNA) is achieved in less than 35 minutes. Fluidic control is achieved using a capillary burst valve laser-ablated in a novel manner to confine the PCR reagents to a chamber during thermal cycling; additionally, a manual, torque-actuated pressure system is created to mobilize fluid from the PCR chamber to the detection reservoir containing oligonucleotide-adducted magnetic particles. Interaction of amplified products with the particles in a RMF allows for near instantaneous (<30 sec) detection based on hybridization-induced aggregation of the particles. The integration of PCR with this rapid, sequence-specific DNA detection method on a single microdevice presents the

possibility of creating point-of-care nucleic acid testing systems that are low cost, easy to use, and involve minimal external hardware.

2.2 Part One: Development of a Dual-Force Aggregation System

2.2.1 Introduction

The detection and quantification of DNA in biological samples is integral in genomic analysis techniques widely used in the biomedical sciences as well as forensic science (2-4). As an important example, DNA is often quantified in order to ensure that a sufficient mass of template DNA is available for amplification by the polymerase chain reaction (PCR), a core component of many nucleic acid based assays (5). This is normally achieved through fluorospectrometry (6) or spectrophotometry (7), both of which require costly instrumentation and assay protocols that can be time-consuming.

The binding of polynucleic acids to silica represents the dominant commercialized technology for nucleic acid purification today, and has for several decades (8-12). More recently, silica particles have been magnetized to enable robotic platforms for nucleic acid purification (13,14), and used for solid phase extraction in microdevices (15,16). Magnetic particles have been further exploited in microscale (nL- μ L) systems in a number of ways, including fluid migration through ferrofluidic pumps (17), reagent mixing (18) and analyte detection and quantification (19).

The binding of DNA to silica coated magnetic particles serves as the foundation for CDA-based DNA detection and quantification. With CDA, a chaotropic salt (i.e., guanidine hydrochloride, GuHCl) dehydrates the DNA and facilitates its binding to the surface of 8 μm silica-coated paramagnetic particles. Application of a RMF enhances the kinetics of this process, where the rapid (minutes) binding of DNA strands to multiple paramagnetic particles causes them to aggregate to the extent where they are visible to the naked eye (**Fig. 2-1**). In the absence of DNA, a homogenous dispersion of the

particles is maintained. The degree of particle aggregation (or dispersion) is measured through digital image analysis with an in-house algorithm described by Leslie et al (1). Briefly, a threshold gray value is set so that beads are counted as “dark,” and areas in the image devoid of beads are counted as “bright.” The number of dark pixels (referred to as “Dark Area”) in the image is used as a measure of aggregation. The tighter

the aggregation (as a result of increased DNA content), the smaller the number of dark pixels and the lower the Dark Area value (refer to **Fig. 2-2**). A sample containing no DNA (i.e., completely dispersed) is set to be 100% Dark Area.

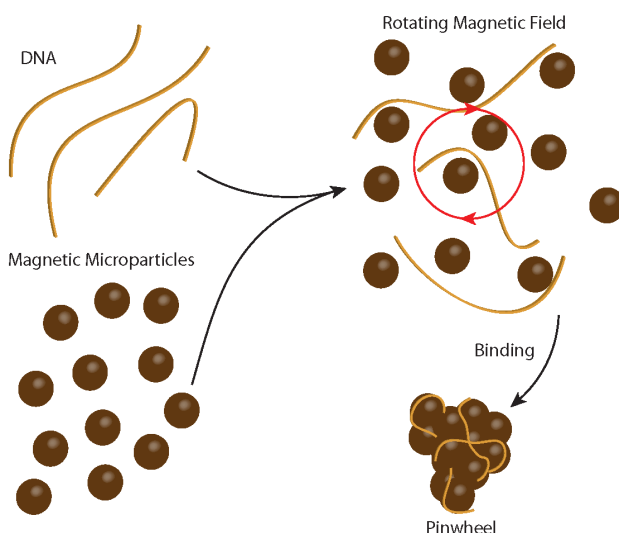


Figure 2-1. Proposed mechanism of chaotrope-driven aggregation (CDA). In a chaotropic environment, DNA binds to silica-coated magnetic beads. The DNA-bead interaction is enhanced using a rotating magnetic field. The DNA becomes entangled around the beads, resulting in visually-distinct bead aggregates that resemble pinwheels. Figure taken from Leslie et al (1).

In previous work, the dynamic range for DNA quantification using the single-plex CDA assay was reported to be 4-80 pg/ μ L (1), and this sensitivity was comparable to commercial fluorescence-based quantitation assays (22).

Furthermore, it was shown that this assay provided an inexpensive alternative to cell counters for white blood cell enumeration (1), an essential tool in bio research and clinical laboratories. Although this phenomena is

associated with attractive economics, accuracy, and ease-of-use, analysis of a single microwell at a time provided inadequate throughput for multiple samples, and needed to be improved dramatically to enable real-world functionality in the laboratory. Here, it is shown that coupling agitation with the RMF not only allows for effective multiplex sample analysis, but also decreases the analysis time by ~35-fold, and increases the sensitivity of DNA detection to an LOD of 250 fg/ μ L.

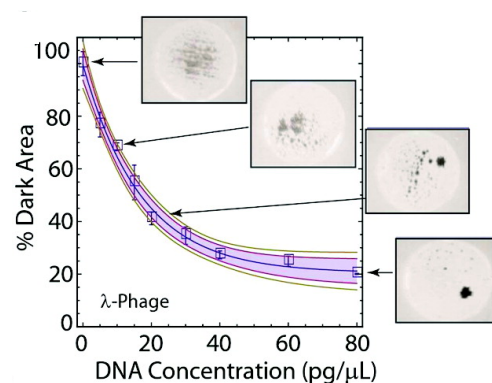


Figure 2-2. Dark Area analysis for DNA quantification. Using a simple image analysis algorithm, % Dark Area is used to measure the extent of bead aggregation. A sample containing no DNA is set as 100% Dark Area, and the % Dark Area is reduced with increasing DNA content. Figure taken from Leslie et al (1).

2.2.2 Materials and Methods

2.2.2.1 Reagents

MagneSil superparamagnetic particles, pre-purified hgDNA (female) were purchased from Promega™ (Carlsbad, CA). Lambda phage genomic DNA (48.5 kb long) from *E. coli* infected with CI8S7Sam7 in storage buffer [10 mM Tris-HCl (pH 7.5, 10 mM NaCl,

1 mM EDTA] was purchased from USB (Cleveland, OH). Guanidine hydrochloride (GdnHCl), 2-(4-morpholino) ethanesulfonic acid (MES, enzyme grade), hydrochloric acid, sodium hydroxide, acetone and ethanol were purchased from Fisher (Fair Lawn, NJ). 2-Amino-2-(hydroxymethyl)- 1,3-propanediol (Trizma base, 99.9%) was purchased from Sigma (St. Louis, MO). All solutions were prepared in Nanopure™ water (Barnstead/Thermolyne, Dubuque, IA). Quant-iT™ PicoGreen® dsDNA assay kit was purchased from Invitrogen, part of Life Technologies™ (Grand Island, NY).

2.2.2.2 Microwell fabrication

A VersaLASER system 3.50 from Universal Laser Systems (Scottsdale, AZ) was used to fabricate microwells, cutting through 1.0 mm-thick PMMA purchased from Astra Products (Baldwin, NY). Each microwell device was prepared as a 12-well circular array of 5-mm-diameter circular wells on a 4-cm square device, designed in AutoCAD. These were then thermally bonded using established methods (23) to a second 4-cm square 1.5-mm-thick PMMA, purchased from McMaster-Carr (Santa Fe Springs, CA). Microwells were sterilized in 2M hydrochloric acid for 30 min, then rinsed with Nanopure™ water prior to use.

2.2.2.3 Device design

Adapting from a device design previously used to perform the pinwheel assay (1), a device consisting of 12 microwells, 5 mm in diameter and 1 mm deep, was fabricated

from poly(methyl methacrylate) (PMMA). Wells were organized so that the center of each well was equidistant from the center of the device.

2.2.2.4 Reagent and sample preparation

Superparamagnetic particles (30 μ L) were washed three times in 6M GdnHCl pH 6.1 and resuspended in 1 mL of 6M GdnHCl pH 6.1. Lambda phage genomic and human genomic DNA were initially prepared at concentrations of 1 ng/ μ L by diluting concentrated stock solutions with 1X TE buffer. Samples were further serially diluted from 1 ng/ μ L to 0.250 pg/ μ L. Fluorospectrometer samples were prepared according the Thermo Scientific PicoGreen® protocol.

2.2.2.5 Assay instrumentation

Images of the microwells were collected by using a T1i DSLR camera with MP-E 65 mm f/2.8 1–5 \times macro lens purchased from Canon U.S.A., Inc. (Lake Success, NY). A Thermix Stirrer model 120S magnetic stir plate was purchased from Fisher Scientific (Fair Lawn, NJ). Three, 5-mm x 5-mm cylinder neodymium magnets were purchased from Emovendo (Petersburg, WV). A MS3 basic vortexer was purchased from IKA (Wilmington, NC). A Ledu compact desk magnifier lamp was purchased from Guy Brown Products (Brentwood, TN) and used without optics to provide lighting around the entire sample. Magnetic and vortexer rotation speeds were determined using a digital photo laser non-contact tachometer, purchased from Amazon.com (Seattle, WA). Mathematica, license obtained through the University of Virginia, was used for image

analysis via the algorithm described previously (1). Fluorospectrometer studies were completed on a NanoDrop 3300 from Thermo Scientific (Wilmington, DE).

2.2.2.6 Assay protocol

A 12-plex microdevice was placed securely inside a foam frame on top of the vortexer. GdnHCl (16 μ L), paramagnetic particles (3 μ L), and sample (1 μ L) were added to each well. The vortexer was placed under the RMF (2400 rpm) and the speed of the vortexer set to 650 rpm. After 60 seconds under the RMF, the speed of the vortexer was reduced to 475 rpm. After another 60 seconds, the speed was reduced to 315 rpm for 5 seconds. After this time the vortexer was removed from the RMF and allowed to run for 15 more seconds. Once the assay was complete, each well was individually photographed, and the photographs analyzed using a Kapur algorithm in the program Mathematica®. The program produced the Dark Area values that were translated to % Dark Area values and plotted versus the concentrations prepared. Fluorospectrometer assays were performed according to the Thermo Scientific protocol (www.nanodrop.com).

2.2.3 Results and Discussion

2.2.3.1 The DFA system

In previous work, a 20 μ L CDA assay was carried out in a single 5 mm microwell positioned directly at the center of the RMF, and allowed for the homogenous distribution of 8 μ m paramagnetic particles in the absence of DNA. However, in proximal wells that were not positioned directly at the RMF center, the particles did not remain

homogeneously distributed, but rather followed a larger circular path in the RMF that resulted in the particles being dragged to the edge of the wells (see **Fig. 2-3**). This was problematic because, in order to maximize the dynamic range of the system, the beads needed to remain in a homogeneously dispersed state in the absence of DNA for effective image processing to define the zero aggregation state (100% Dark Area). In the absence of this effect, processed images from the proximal wells did not allow for significant discrimination between a negative response (no aggregation in the absence of DNA) and a DNA-induced aggregation (at high [DNA]) (**Fig. 2-3**). As a result, analysis could only be carried out in the single well at the center of the RMF.

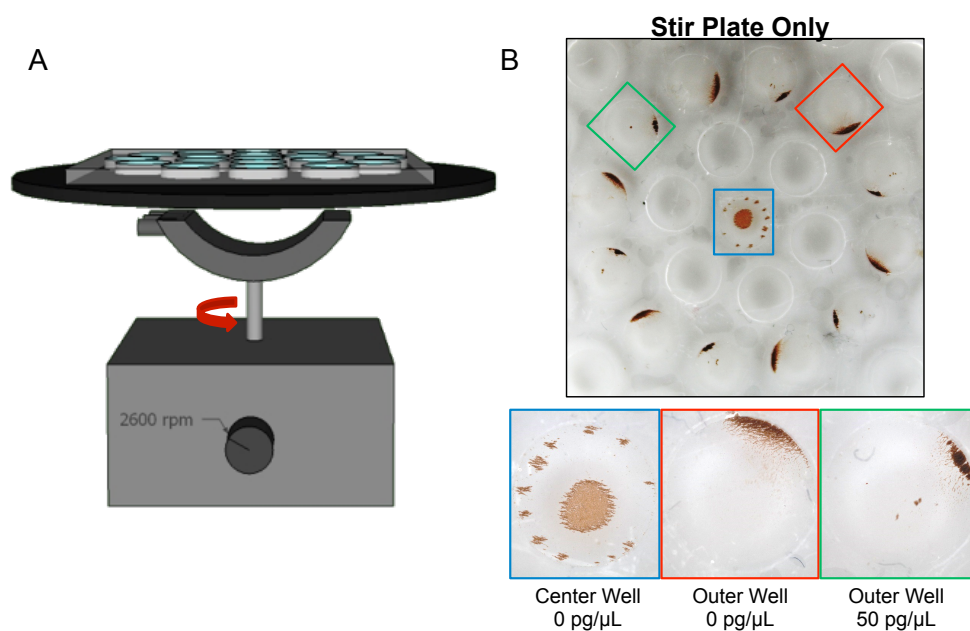


Figure 2-3. Multiplexing with RMF below device. A) A schematic of the previously used RMF system, where the magnet rotates below the device. B) Attempts to quantify DNA samples in wells away from the center of the device proved unsuccessful due to accumulation of beads along the sides of the wells. The data indicated minimal dynamic range between negative controls and DNA-induced aggregation.

In an effort to optimize particle dispersion and minimize the accumulation of the particles at the microwell wall, agitation in the form of irrotational vorticity (IV) (a vortexing motion) was employed as an additional force. This force was added in an attempt to counter the RMF-induced movement of particles to the wall of the microwell by driving the particles towards the center. We refer to this effect as Dual-Force Aggregation, or DFA. The optimization of the DFA system for DNA quantification with acceptable accuracy across different DNA samples is described in the following sections.

2.2.3.2 Optimization of the DFA system for DNA quantification

Due to its uniform length, λ -phage genomic DNA (48.5 kb) was chosen as a standard to optimize quantification with the DFA system. A number of system parameters needed to be simultaneously, yet individually, evaluated, including: 1) the size of the magnetic field (i.e., type, size, and number of magnets), 2) the magnetic field strength (i.e., height of the RMF above the microdevice), 3) the rotation speed of the magnet, and 4) the IV speed.

Several different types and combinations of magnets were explored to find a magnet that would provide the size and strength of magnetic field necessary to obtain consistent aggregation across multiple wells. Tested magnets varied from a large magnet made up of a series of cylindrical neodymium (NdFeB) rare earth magnets, to the original magnet used in previous work, to a combination of both types of magnets. This report will focus on the originally published magnet (1), augmented with cylindrical NdFeB rare earth magnets, which was determined to be optimal. The distance between the rotating magnet and the top surface of the chip was varied, as this controlled the magnetic field

strength. The magnetic field strength was measured as the rotating magnet was raised in 1 mm increments. Not surprisingly, the range of RMF strength varied dramatically with distance from 8 Gauss (1.9 cm above the device) to 30 Gauss (1.1 cm). Using effective bead dispersion in the absence of DNA compared to a positive control of 50 pg/ μ L λ -phage DNA as the metric, the optimal magnetic field strength (in conjunction with IV force, discussed below) was found to be 25 Gauss with the rotating magnet positioned 1.3 cm above the microdevice. At distances less than 1.3 cm, the RMF dominated, reducing the effective bead dispersion in the absence of DNA. Field strengths at distances greater than 1.3 cm did not provide the necessary aggregation to maximize the dynamic range of the system. **Figure 2-4** illustrates the effect of magnet height on the degree of

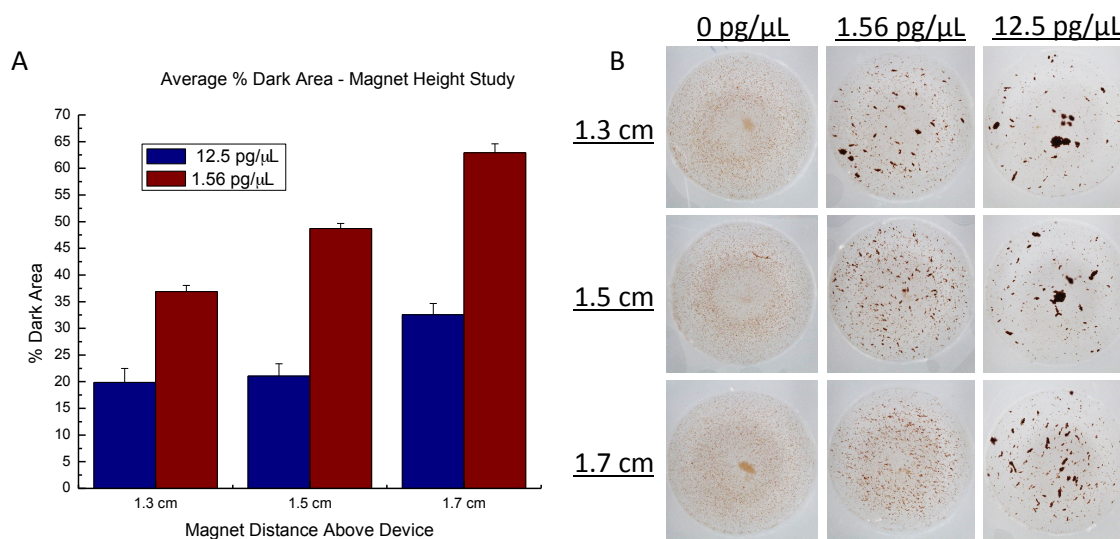


Figure 2-4. Study of magnet height above device. A) A histogram illustrating the differences in % Dark Area as the magnet is moved away from the device. At lower DNA concentrations, the difference in height becomes more apparent. While the difference in % Dark Area between 1.3 cm and 1.5 cm is small for $[DNA] = 12.5 \text{ pg}/\mu\text{L}$, the difference is much larger for $1.56 \text{ pg}/\mu\text{L}$. This indicates a loss of sensitivity and smaller dynamic range as the magnet is moved away. A magnet distance of 1.3 cm was determined to be optimal, in part due to the fact that the magnet could not be placed closer without being impeded by the IV instrument. B) Images of wells illustrating the difference in dark area for both concentrations at different magnet heights.

aggregation. As the magnet is moved away from the device, the degree of aggregation is reduced while the dispersion of beads in the absence of DNA remains the same. It is noted that at high concentrations, a reduction in aggregation due to the change in height was less prominent; however, at lower concentrations the degree of aggregation was much more sensitive to the height of the magnet. As a result, the dynamic range of the system was reduced when the magnet moved above 1.3 cm from the device.

Equally as important as the distance between the rotating magnet and the microdevice is the speed of both the RMF and IV. In a multiwell system, the RMF below the device drastically reduced the difference in aggregation between a well with 50 pg/ μ L of DNA and one with no DNA (**Fig. 2-5A**); positioning the RMF above the device improved the results, although the results were not optimal (**Fig. 2-5B**). The IV force alone provided no distinguishable difference between wells with DNA and those without (**Fig. 2-5C**). Thus, it became clear that the balance between the RMF and IV forces would be critical in providing optically-distinguishable aggregations that were DNA-dependent, and ultimately providing reproducible quantification of DNA.

Using the augmented bar magnet, which had a magnetic strength of 25 Gauss, there was a fine tipping point with the IV rotation speed. Above 650 rpm, the IV effect overpowered the RMF-induced movement of beads to the wall and, thus, the beads began to concentrate in the center of each well, similar to **Figure 2-5C**. If the IV speed was reduced below 315 rpm, it became ineffective, the RMF effect dominated, and the beads mobilized to the wall; under these conditions, the negative controls began to resemble

those in **Figure 2-5B** and caused a reduction in sensitivity and dynamic range of the system.

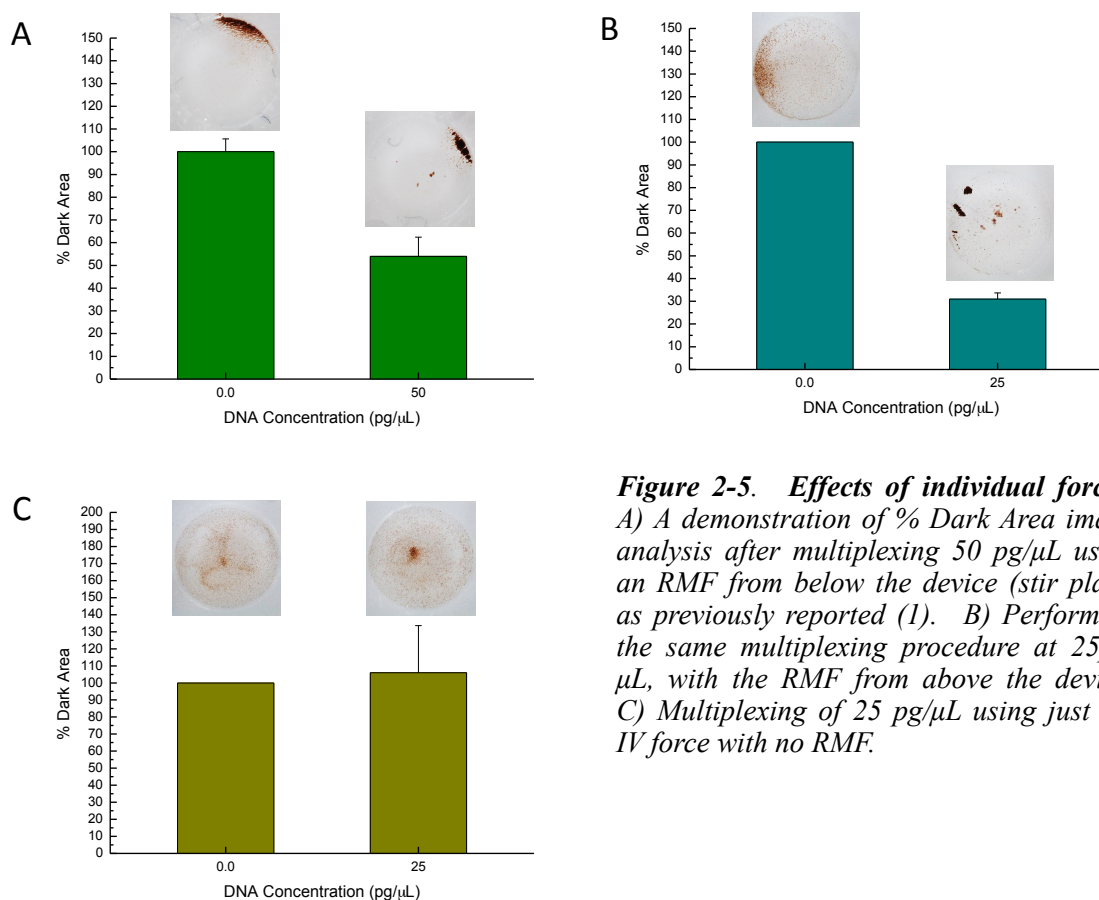


Figure 2-5. Effects of individual forces.

A) A demonstration of % Dark Area image analysis after multiplexing 50 pg/μL using an RMF from below the device (stir plate) as previously reported (1). B) Performing the same multiplexing procedure at 25pg/μL, with the RMF from above the device. C) Multiplexing of 25 pg/μL using just the IV force with no RMF.

Using the effective aggregation of beads at a given DNA concentration across the 12 wells as the metric, the rotation speed of the magnet was varied from 1000-3000 rpm at IV speeds varying from 300-800 rpm (100 rpm increments). In addition to using the IV to counter the RMF, a step-wise control in IV speed was also studied to explore further improving the overall aggregation by taking advantage of the effect of different IV speeds. This involved exploring a “mixing step” (high speed IV, vortexing each well), an “aggregation step” (intermediate speed IV, RMF and IV forces balanced), and a

“mobilization step” (low speed IV, no RMF, centering aggregates). These studies were completed systematically by varying the IV rpm (300-800 rpm) during the assay (all other parameters constant) until a combination of IV speeds resulted in the most favorable aggregation of the particles compared to a single rpm for the length of the assay. It was determined that the three speeds that provided optimal, reproducible, aggregation were 650, 475, and 315 rpm.

The metric for optimization of all aforementioned parameters (i.e., field size, magnetic strength, RMF speed, and IV speed) was comparable aggregation in each of the 12 wells containing equivalent DNA concentrations, with a % Dark Area that varied by less than 10% (i.e., the relative standard deviation <10%). Ultimately, the system was considered optimized with the following parameters: RMF of 25 Gauss at a velocity of 2400 rpm, at a 1.3 cm distance between the top surface of the device and the magnet, and IV decreasing step-wise from 650 rpm (60 sec) to 475 rpm (60 sec) and finally to 315 rpm (20 sec). The final 15 sec of IV at 315 rpm takes place in the absence of an RMF in order to mobilize the aggregates to the center of the wells, while beads in the negative control wells remain dispersed. This reduces variability in % Dark Area between aggregations induced by the same concentration of DNA in different wells. These parameters provided the ideal system; tight DNA-bead aggregates centered in the wells with positive samples, and dispersed beads with negative samples or blanks. **Figure 2-6A** shows a schematic representation of the DFA system while **Figure 2-6B** demonstrates the difference between negative controls and positive samples across 12 wells under the optimal conditions described above.

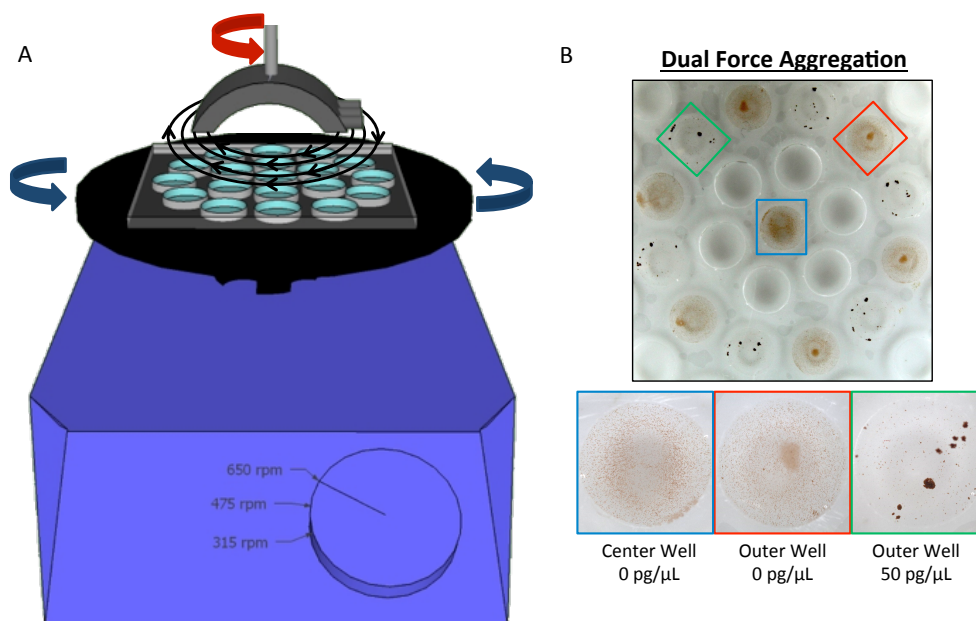


Figure 2-6. Dual force aggregation (DFA) system. A) Schematic representation of the DFA set-up. The microdevice is placed in a foam frame atop an agitator while the MF rotates from above the device. B) A photograph of the 12-well microdevice with alternating concentrations of 0 pg/μL (red) and 12.5 pg/μL (green).

2.2.3.4 λ -Phage DNA samples

With operational parameters determined, standard curves relating the % Dark Area of aggregated beads with λ -phage DNA concentrations ranging from 0-25 pg/μL were generated. The standard curves that resulted were similar to those reported previously (1) (Fig. 2-7A) with an exponential decay in Dark Area as DNA concentration increased; a plot of the natural log of both the DNA concentration and the % Dark Area is shown in Figure 2-7A (inset). The LOD for the DFA system for λ -phage genomic DNA is ~1.5 pg/μL, representing more than a 2-fold decrease in LOD compared to the 4 pg/μL achievable with the previously reported system. The increased sensitivity likely emanates from the ability of the IV to enhance DNA-particle interaction, allowing for the

formation of tighter aggregates at lower DNA concentrations, while still maintaining the dispersion of particles not bound to DNA. While the sensitivity improved with the DFA system, the dynamic range of the system did not. Instead, improved interaction of the particles and the DNA saturates the binding of the DNA at a lower concentration, plateauing at a Dark Area of 20%.

To test the accuracy of DNA quantification, a second set of DNA samples ranging in concentration from 2 pg/ μ L to 16 pg/ μ L was interrogated on the same chip at the same time as a standard curve. **Figure 2-7B** shows the relationship between prepared concentrations and the measured values from the standard curve, where the dotted line denotes a 1:1 correlation. A fit of the data shows an R^2 value of 0.9990 and a y-intercept of 0.975, demonstrating the ability for the system to accurately determine random DNA concentrations from a standard curve generated on the same device. It is

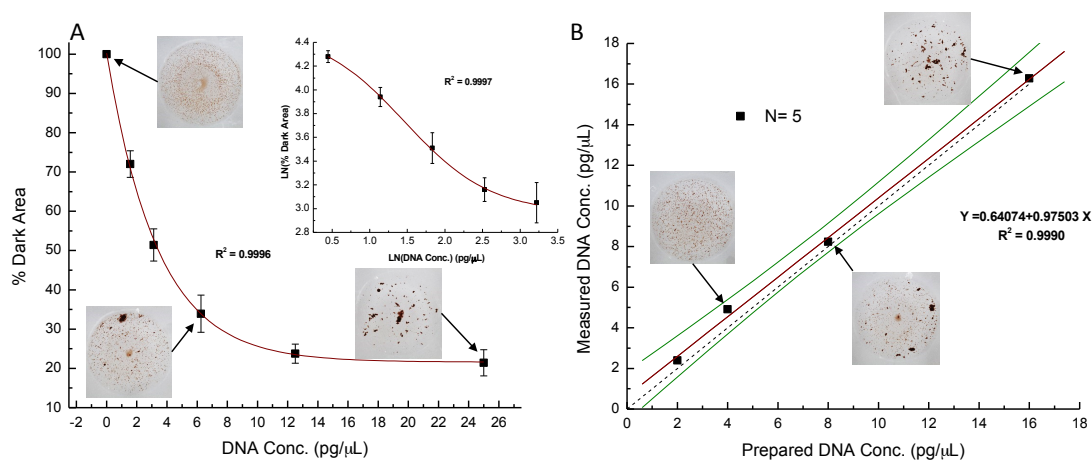


Figure 2-7. λ -Phage DNA standard curves. A) A standard curve was generated for serially diluted λ -phage DNA concentrations ranging from 0-25 pg/ μ L. The inset picture shows the data plotted as natural log functions. B) To illustrate the capability for quantification, the correlation between prepared concentrations and measured values of a second set of DNA samples is shown. The dotted line represents a 1:1 correlation, where the red line is a line of best fit surrounded on either side by green lines representing 95% confidence bands.

clear that the quantitation results from the DFA assay compare favorably with the known values for the prepared samples.

2.2.3.5 Human genomic DNA samples

Analogous experiments were performed using pre-purified human genomic DNA (hgDNA). Standard curves were generated under the same conditions used for the λ -phage DNA experiments, this time with DNA concentrations ranging from 0 pg/ μ L to 12.5 pg/ μ L. The curve trends mirror those with λ -phage DNA, as does the maximum % Dark Area which plateaued around 20% (**Fig. 2-8A**). The LOD for hgDNA is 0.250 pg/ μ L, a dramatic improvement over 10 pg/ μ L reported with the previous system (1). As previously stated, an increase in sensitivity with this system is due to an enhanced interaction of the DNA sample with the particles. In addition, the increase in sensitivity over λ -phage DNA is likely related to DNA length. We have previously shown that the extent of aggregation at a given DNA concentration is dependent on DNA length (1). That report showed in samples that differed in length by 43 Kbp, there was an order of magnitude difference in DNA concentration required for the same degree of aggregation. The manufacturer of the hgDNA standard (Promega™) simply states that 90% of the hgDNA is greater than 50 Kbp in length, and that the source of DNA is from multiple volunteers (manufacturer product information). In comparison, the λ -phage genome remains largely intact at 48.5 Kb. Therefore, due to the increase in average length for hgDNA compared to λ -phage, an increase in sensitivity is expected.

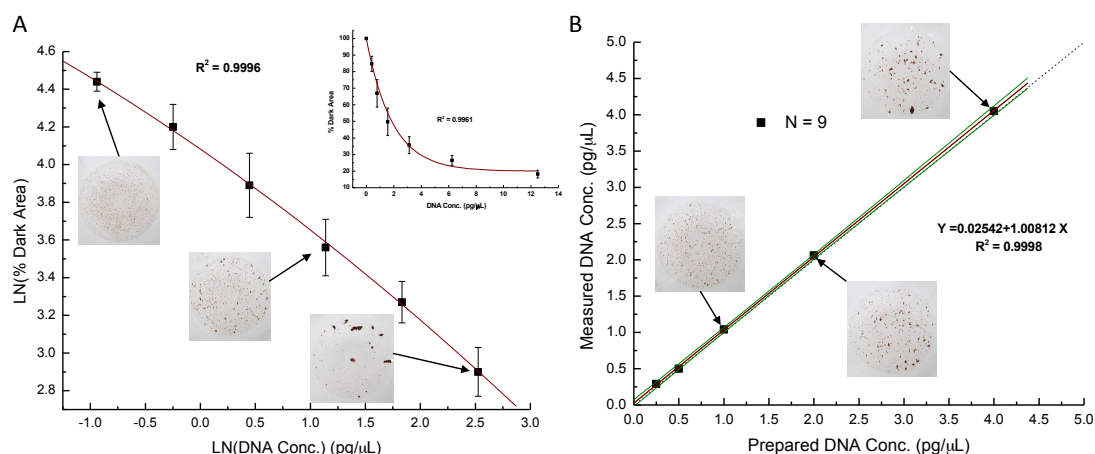


Figure 2-8. Human genomic DNA standard curves. A) A standard curve was generated from serially diluted human genomic DNA, beginning at 12.5 pg/μL. The inset picture shows the data plotted as natural log functions. B) To illustrate the capability for quantification, the correlation between prepared concentrations and measured values of a second set of DNA samples is shown. The dotted line represents a 1:1 correlation, where the red line is a line of best fit surrounded on either side by green lines representing 95% confidence bands.

Similarly to the λ -phage studies, a second set of hgDNA concentrations ranging from 0.25 pg/μL to 4 pg/μL were interrogated simultaneously with a hgDNA standard curve to determine the accuracy of DNA quantitation. **Figure 2-8B** shows the relationship between prepared concentrations and the measured values from the standard curve, where the dotted line denotes a 1:1 correlation. A fit of the data (each point $n=9$) shows an R^2 value of 0.9999 and a y-intercept of 1.008, demonstrating a strong correlation to expected values and the ability for the system to accurately determine random DNA concentrations from a standard curve generated on the same device.

2.2.3.6 Comparing DFA to spectrophotometric methods

After successfully achieving a 12-plex CDA assay with improved sensitivity, the same standard DNA samples (λ -phage and hgDNA) utilized in the earlier experiments were

quantified with a commercial fluorospectrometer (NanoDrop™ 3300) to provide a direct comparison with a validated system. Samples were quantitated via the PicoGreen® assay protocol provided by Thermo Scientific. **Figure 2-9** shows a correlation plot demonstrating the accuracy of the fluorospectrometer to quantify samples from a standard curve. In addition, the data from the λ -phage and hgDNA samples were added to the plots for a direct comparison. DFA is shown to comparably quantify DNA with accuracy at a lower LOD compared to the fluorescent method. The fluorospectrometer

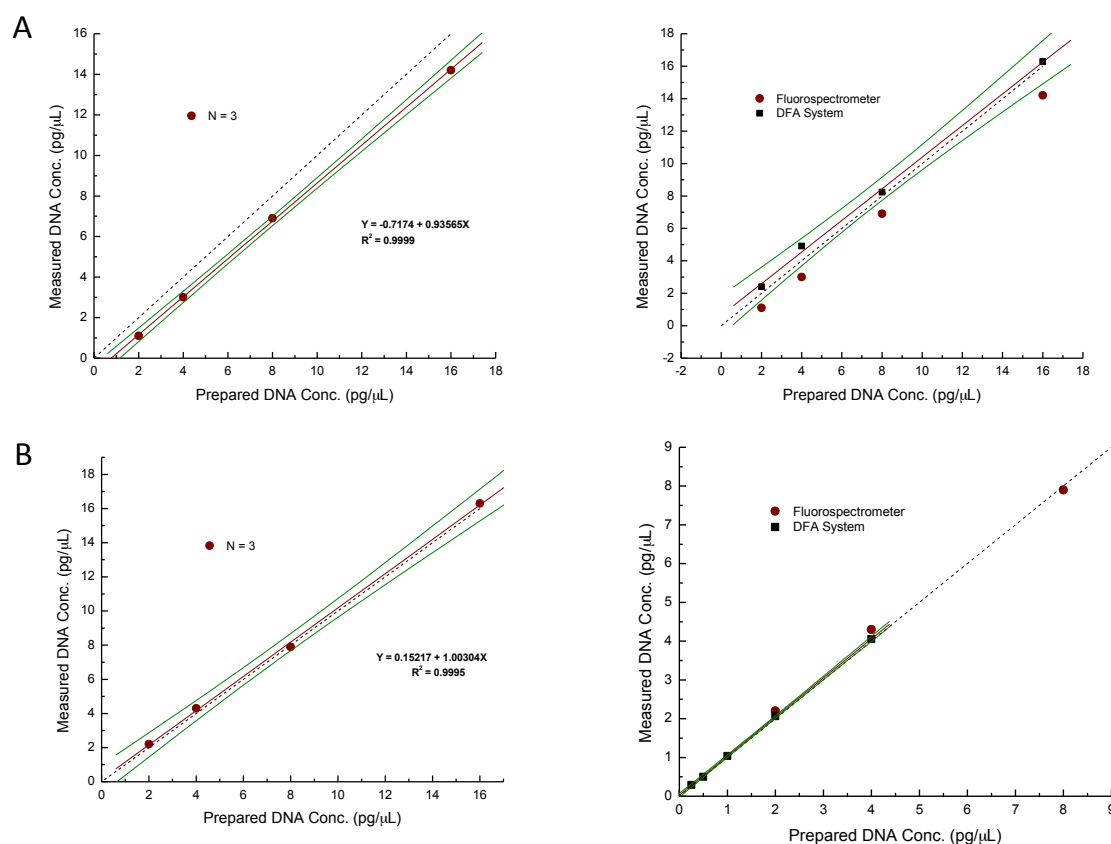


Figure 2-9. Comparison of DFA to a fluorospectrometer. A) Plots demonstrating the correlation of prepared concentrations and measured values of λ -phage DNA when using a fluorospectrometer and the DFA system. The dotted line represents a 1:1 correlation, while the red line is a line of best fit surrounded on either side by green lines representing 95% confidence bands. B) Correlation plots of measured and prepared concentrations of hgDNA when quantitating with both a fluorospectrometer and the DFA system.

LOD is 1 pg/ μ L for double-stranded (ds) DNA while the LODs for the DFA method are \sim 1.5 pg/ μ L and 0.250 fg/ μ L for λ -phage DNA and pre-purified human DNA, respectively. Another advantage to the DFA system over the fluorescent method involves assay time and instrumentation. DFA requires no fluor labeling, incubation times, individual sample measurements which allows a decrease in overall assay time from approximately 2-10 seconds per analysis plus five minutes for fluor incubation, to 140 seconds to simultaneously analyze 12 samples. Further, DFA has the benefit of a reduction in cost. A fluorospectrometer such as the NanoDrop™ 3300 retails for \sim \$12,000 plus fluorescent reagents, while the camera, agitator, and magnet, of the DFA system costs a total of \sim \$1300 with no cost for fluorescent reagents. Finally, while the fluorospectrometer provides a significantly larger dynamic range (1 pg/ μ L – 1000 pg/ μ L for dsDNA), the DFA system still provides a dynamic range that spans over two orders of magnitude. The advantages of DFA over fluorospectrophotometry are highlighted in **Table 2-1**. Overall, the DFA system provides a comparable, rapid alternative DNA quantification method to a fluorospectrometer.

Method	Cost Per Analysis	Time per Analysis	Instrument Cost	Fluors Needed?	Need to calibrate each time?	Automatable?	Limit of Detection
Fluoro-spectrometry	\sim \$2.00	\sim 10 sec	\$12,000	Yes	Yes	No	1 pg/ μ L
DFA	$<$ \$0.25	140 sec per device (12 wells)	\$1300	No	No	Yes	0.250 pg/ μ L

Table 2-1. Comparison of DFA to a fluorospectrometer.

2.2.4 Conclusions

This work describes the comprehensive and methodical optimization of the DFA system for enhanced DNA quantification based on the aggregation assay introduced in an earlier report (1). The DFA approach allows for a 140 second, 12-plex assay in a simple circular microwell array, providing a ~4-fold reduction in assay time compared to a conventional fluorospectrometer, while reducing cost by almost 10-fold. Further, for double-stranded hgDNA, the DFA system offers a ~4-fold increase in sensitivity with an LOD of 0.250 pg/ μ L over the 1 pg/ μ L of the fluorospectrometer. Ultimately, the DFA system provides a simple, rapid, and inexpensive strategy for DNA quantification that should be competitive with existing commercial DNA quantification methods.

2.3 Part Two: Development of an Integrated Microdevice for DNA Amplification and Sequence-Specific Detection

2.3.1 Introduction

The sensitive and specific identification of nucleic acid targets is central to the fields of clinical diagnostics, food safety, forensics and environmental microbiology. Nucleic acid testing (NAT) typically incorporates amplification and detection technologies, many of which require complex operational steps and expensive instrumentation (24,25). Such resource-intensive processes limit the use of NAT assays to reasonably skilled personnel in centralized laboratories and presents challenges for its use at the point-of-care (POC).

However, important applications, such as pathogen detection in remote environments and time-critical diagnostics, require assays that can be performed in POC settings (26,27). The profound impact promised by microfluidics has garnered extensive efforts toward the development of truly portable POC NAT technologies (24,28,29), and many of these involve the incorporation of amplification and detection strategies onto a microfluidic platform (30). Microfluidic assays offer the advantages of rapid analysis, low power consumption, and functional integration of multiple analytical processes (31). By exploiting the strengths of microfluidics, microdevice-based NAT technologies have the potential to be low cost, portable, and easy to use, which are qualities that are critical for implementation at the POC.

Some form of amplification is almost always required in NAT to provide specificity, increase the signal, and assure detection of a target. A number of amplification techniques have evolved, including strand-displacement amplification (32), nucleic acid sequence based amplification (33), and rolling-circle amplification (34), but polymerase chain reaction (PCR) remains the most popular due to its simplicity and amplification power (35). PCR on a microfluidic device was first demonstrated in 1993, and has since been replicated and improved in a number of formats (36,37). The Landers group has successfully demonstrated non-contact infrared (IR)-mediated PCR (IR-PCR) for chip-based amplification and shown the capabilities of this platform to be multiplexed, as well as integrated with upstream and downstream analytical processes (38-40).

The post-amplification analysis of DNA takes on multiple forms for end-point or real-time detection, and these range from hybridization microarrays to capillary electrophoresis and capillary gel electrophoresis, among others (24,35,41-46). Despite the successful implementation of these detection methods on microdevices, many are unsuitable for implementation on POC platforms as a result of the expensive and complex instrumentation required. An attractive detection approach would involve minimal peripheral instrumentation and provide a simple output for interpretation. As such, visual detection methods are an attractive tool for POC applications (27).

The Landers group previously reported a novel particle-driven technique for the visual detection of DNA targets on a microfluidic platform, termed hybridization-induced aggregation (HIA) (1,47). Core to the power of HIA is the ability to differentiate target-specific amplicons from non-specific nucleic acid sequences, which, coupled with the specificity of PCR amplification, brings a second level of specificity to the assay. HIA utilizes a pair of oligonucleotide probes that are complementary to the target DNA sequence. The probes are immobilized on the surface of 1 μm paramagnetic particles (via biotin-streptavidin conjugation), and their interaction with target DNA is enhanced by a RMF. The hybridization of the target sequence to the particle-bound probes induces aggregation of the particles in a manner that rapidly provides visual confirmation of the presence of target DNA in the sample (**Fig. 2-10**). Like the CDA assay, the degree of particle aggregation can be determined through digital image analysis, using a simple algorithm to measure Dark Area. The inherent simplicity and specificity of HIA make it an ideal approach for end-point detection on a NAT device.

A significant challenge facing the integration of amplification and detection processes are related to microfluidic control and device operation (28). Necessary fluid handling and actuation almost always requires the use of complex and bulky peripherals that are not amenable to POC testing. Human operated fluid pumps, such as finger pumps (48-50), have emerged as attractive techniques for fluid actuation in microfluidic systems that can be considered portable. In the current work, we exploit a small machine screw to facilitate fluid movement in our microdevice, which is hand-operated and does not require additional equipment or resources. The torque-actuated pressure (TAP) provided by the screw provides deflection of an elastomeric material into a fluid compartment, which displaces the fluid and drives it into a microchannel. In a similar approach, Weibel et al. previously demonstrated the use of screws embedded in a PDMS microdevice (“TWIST valves”) for fluid pumping (51). The TWIST valves create compartments in which fluids are held under pressure. Upon opening the TWIST valves, the pressure,

stored in the elastic deformation of the walls and ceiling of the PDMS, pushes the fluid out of the compartments and into microfluidic channels.

It is imperative to control the actuation and timing of fluid flow in integrated microfluidic devices. This has traditionally been achieved with pneumatic valves (52) that require external hardware (e.g., vacuum pumps or electronic junctions) (53), escalating the cost and footprint of the micro-platform. Geometric passive valves are attractive because they exploit the microchannel architecture itself to create surface tension at the meniscus that halts fluid flow via capillary action. Such passive valves have been challenging to create in PMMA, an increasingly common material in microdevice fabrication due to low cost and rapid fabrication with CO₂ laser ablation. The difficulty in creating passive valves in PMMA is due to roughness of the surface and lack of precision associated with laser ablation-based microfabrication. Recently, Mohammed et al. described “rastering” the PMMA surface (many low power laser passes over the surface) to create a 600 μm deep geometric burst valve in PMMA (54). PMMA capillary burst valves have also been shown in a centrifugally-driven microfluidic device with channel depths of 500 μm using compute numerical control micromilling (55). Both processes create wide, deep channels that are more likely to collapse during bonding, while also increasing reagent waste/loss. As a result, a “vector cut” (a single high-powered pass of the laser over the PMMA surface) is preferable, as it is capable of generating shallow, narrow channels. In this report, we demonstrate a novel passive geometric burst valve created in PMMA with a vector cut, circumventing the issues seen with previous efforts.

Achieving fluidic control with a novel laser-ablated capillary burst valve and manual torque-actuated pressure system allowed for the integration of multi-sample IR-PCR with HIA-based detection on a simplistic PMMA microdevice (**Fig. 2-11**). We demonstrate the utility of this device for the rapid detection of the zoonotic pathogen *Salmonella enterica* (56), an organism of substantial public health concern.

2.3.2 Materials and Methods

2.3.2.1 Microdevice design

Four ellipsoid PCR chambers (5 mm long, 1.25 mm wide, 0.5 mm deep) are symmetrically oriented within the 7 mm (diameter) focal spot of the halogen lamp for IR-PCR to allow even heating across all chambers. Three of the PCR chambers are each connected to a separate TAP inlet (2.66 mm diameter, 1 mm deep) and HIA

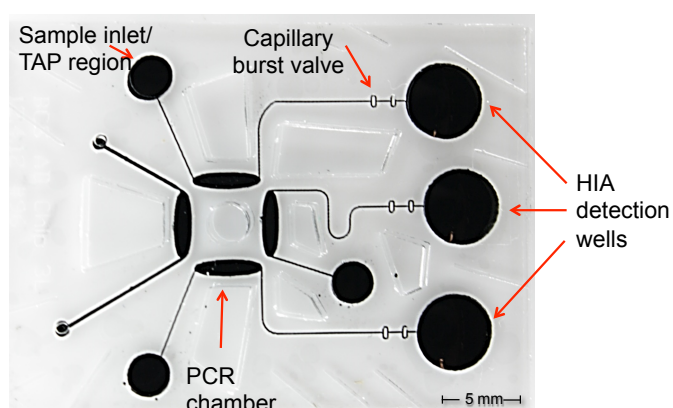


Figure 2-11. Image of the PMMA integrated microdevice. The device is filled with black dye for feature visualization. Highlighted are the four main domains of the device: PCR, valving (burst valve), sample inlet (which is depressed when fluid is mobilized with TAP following PCR) and HIA detection region. Additional features surrounding the primary architecture of the microdevice are “air pockets,” created to reduce the thermal mass of the device and to aid in bonding during device fabrication.

detection chamber (5 mm diameter, 1 mm deep). Along each of the channels connecting the PCR and HIA chambers (14 mm long, 150 μ m wide, 170 μ m deep), there are two adjacent oval-shaped capillary burst

valves (170 μm deep). Though only one valve is functionally necessary, an additional valve is added to account for any fabrication failure in the first valve. The channels are designed such that the HIA chambers are vertically aligned. Additional features (or “air pockets”) surrounding the primary architecture of the microdevice were created to reduce the thermal mass of the device and to aid in bonding during device fabrication.

2.3.2.2 Fabrication of the microdevice, manifold, and rotating magnetic field construct

The microdevice architecture was designed using AutoCAD software. A VersaLASER system 3.50 from Universal Laser Systems (Scottsdale, AZ) was used to ablate the architecture into PMMA (0.5mm thick) purchased from Astra Products (Baldwin, NY) for each of the three layers of the microdevice. The layers were then thermally bonded using established methods, to create a microdevice with a total thickness of 1.5 mm (23). After loading the PCR reagents into the device, the device was sealed with MicroAmp® qPCR adhesive film from Applied Biosystems (Grand Island, NY). A manifold was constructed using 2 layers of PMMA (each with a thickness of 0.635 cm), which encased the microdevice while keeping the PCR and HIA chambers uncovered (see Figure 6). A septum (PTFE face/silicone body) from Sigma Aldrich (St. Louis, MO) was placed above each of the three sample inlets, between the microdevice and the top layer of the manifold. 6-32” mechanical screws were incorporated into the top layer of the manifold, with one above each of the three sample inlets. Three additional mechanical screws were used to “close” the manifold and pressurize the microdevice.

The rotating magnetic field construct was fabricated using 1.0 mm PMMA. Three 2 mm³ neodymium magnets were incorporated onto the construct using a layer of adhesive film. A small motor was connected to the construct to induce automated movement of the magnets in a circular path beneath each HIA chamber.

Channel depths were calculated using Zeiss Axio A1 microscope fitted with a 5X objective.

2.3.2.3 Reagents

Dynabeads® MyOne™ Streptavidin C1 paramagnetic beads were purchased from Invitrogen (Carlsbad, CA). Salmonella enteric, serovar typhimurium LT2 DNA (700720D-5) was purchased from ATCC (Manassas, VA). Biotinylated oligonucleotides were purchased from Eurofins MWG Operon (Huntsville, AL). Potassium chloride and ethanol were purchased from Fisher Scientific (Fair Lawn, NJ). 2-Amino-2-(hydroxymethyl)-1,3-propanediol (Trizma base, 99.9%) was purchased from Sigma (St. Louis, MO). All solutions were prepared in Nanopure water (Barnstead/Thermolyne, Dubuque, IA). SpeedSTAR™ polymerase, magnesium chloride and 10X PCR buffer, is available from Clontech Lab. (Mountain view, CA).

2.3.2.4 Conjugating oligonucleotide probes to particles

Particles were prepared according to the manufacturer's protocol to produce stock particle concentration: 2 mg/mL. Final suspension buffer: 500 µL of 200 mM KCl, 10 mM Trizma base, pH 7.5.

2.3.2.5 PCR

PCR was performed using the following cycling protocol: initial hold at 95 °C for 2 min followed by 32 cycles of 95 °C for 5 sec, 60 °C for 15 sec, and 72 °C for 20 sec, and then a final hold at 72 °C for 2 min. Final concentrations of reagents were, MgCl₂ 3 mM, dNTP's 0.4 μM, 1X PCR buffer, polymerase 2.5 units, primers 2 μM. Non-integrated assays were then removed from the microdevice and the product was separated and detected using an Agilent 2100 Bioanalyzer (Agilent Technologies, Inc., Santa Clara, CA).

2.3.2.6 Oligonucleotide sequences

Forward PCR primer: 5'-AATTATCGCCACGTTCTGGGCAA-3'

Forward HIA probe: 5'-[BioTEG] AATTATCGCCACGTTCTGGGCAA-3'

Reverse PCR primer: 5'-TCGCACCGTCAAAGGAACC-3'

Reverse HIA probe: 5'-GGTTCCTTTGACGGTGCGA[BioTEG-Q]-3'

2.3.2.7 Image analysis

For dye studies and HIA detection, images of the HIA chambers were collected using a T1i DSLR camera with MP-E 65 mm f/2.8 1–5× macro lens purchased from Canon U.S.A., Inc. (Lake Success, NY). Image processing was performed using Mathematica™ software.

2.3.3 Results and Discussion

2.3.3.1 Multiplexed IR-PCR

If HIA is to be an effective technique for sequence-specific DNA detection, it will either have to detect high copy number targets or rely on some form of DNA/RNA amplification to generate enough target for optically-detectable DNA-bead aggregation. It is in this respect that multiplexed PCR is important for specificity, and it is critical to include controls that minimize false negatives due to failure in amplification or sample preparation. With HIA, this facilitates simple interpretation of the results and immediate classification of the sample, via a visual side-by-side comparison with positive and negative controls.

To achieve multiplexed amplification in a microfluidic format that begins to address the potential for fully integrated analysis, four elliptical-shaped chambers, each having a volume of 2 μ L, were symmetrically orientated within the 7 mm (diameter) focal spot of the halogen bulb (defined by the distance of chip positioned above the bulb); three are for PCR samples/controls, with the fourth used as a reference for temperature control (**Fig. 2-12A**). To evaluate temperature homogeneity across all PCR chambers, all chamber temperatures were measured simultaneously using independent thermocouples. The chamber-to-chamber variation in temperature was determined to be $\pm 2^{\circ}\text{C}$. To test the effect of this variation on PCR performance, PCR specific for a 278 bp fragment of the *S. enterica* genome was carried out, and the PCR product generated in each chamber was analyzed by microchip electrophoresis using the Agilent Bioanalyzer (**Fig 2-12B**). Using the semi-quantitative capability of the Agilent Bioanalyzer, it was determined that

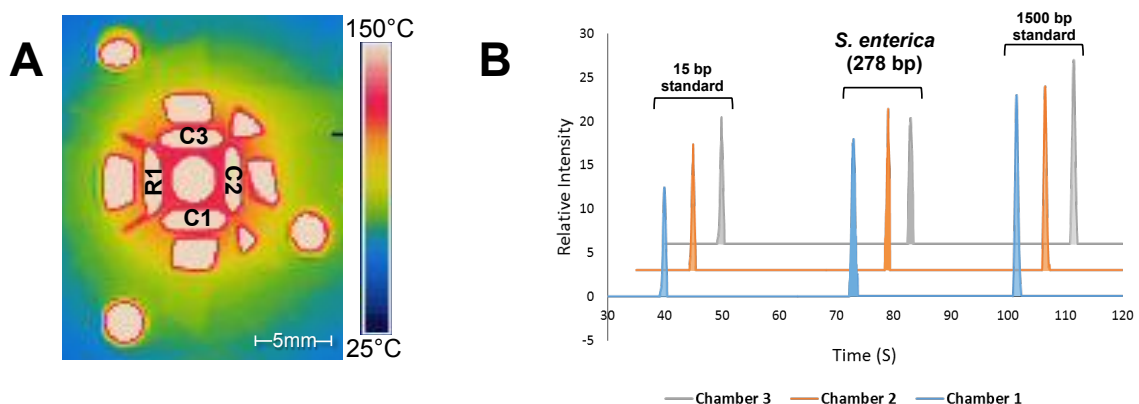


Figure 2-12. Multiplex PCR with a halogen bulb. A) IR camera image of the top layer of the microdevice during thermocycling. PCR chambers are in a symmetrical arrangement around the focal spot of the halogen bulb. The 7 cm diameter represents the hottest section, providing fast heating rates. Each PCR chamber is sized to scale. B) Electropherograms of multiplex IR-PCR amplification of a 278 bp region of *Salmonella enterica*. Lightly shaded peaks are the 15 and 1500 bp markers respectively. Each chamber position corresponds to those in (A).

~3 ng (± 0.3 ng) of the 278 bp fragment was produced in each of the microchip PCR reactions using 1 ng of pre-purified template DNA. With this defining comparable PCR results across all PCR chambers, it was concluded that the slight variation in temperature did not have a significant impact on PCR performance; therefore, three samples could be processed simultaneously on the device without a position-dependent bias.

2.3.3.2 Torque actuated pressure (TAP) system for reagent delivery

Following the completion of amplification, a reproducible volume of the PCR product must be transferred to the HIA chambers for sequence-specific detection. With the aim of avoiding the use of any form of external hardware for fluid flow control (to maintain low cost, portability and ease of use), we created a torque actuated pressure (TAP) system for fluid actuation. Using the turning of a 6-32" mechanical screw to force the elastomeric

materials used to seal the device (septa and bio-film; described in following section) into the sample inlet, the PCR product is forced through the channel into the HIA detection chamber (**Fig. 2-13A**). For this, we fabricated a circular 1 mm deep cavity with a 1.33 mm radius, yielding a total inlet volume of 5.6 μL prior to any deformation of the elastomeric materials by the TAP. Dye studies were performed to verify the intra- and inter-device reproducibility of the TAP delivery system in precise mobilization and delivery of a desired volume of fluid. Blue dye (representing PCR reagents) was used to fill the inlet, PCR chamber and the channel to the valve, while yellow dye (representing HIA reagents) was used to fill the HIA detection chambers. As blue and yellow dyes mix as a result of the TAP activation, the hue resulting from the color change increases

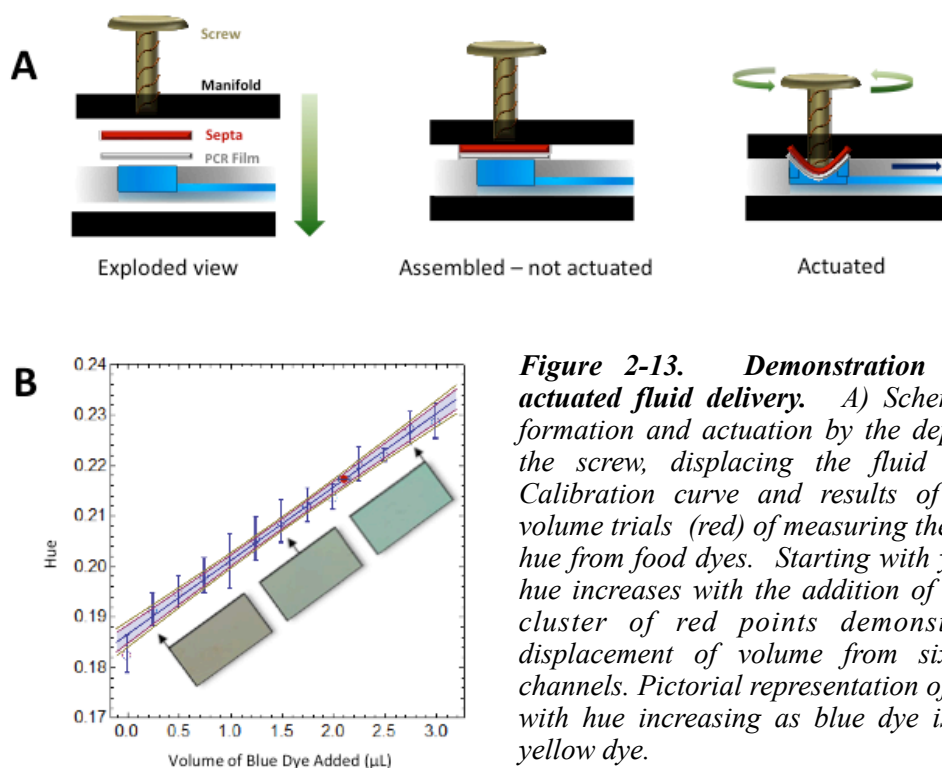


Figure 2-13. Demonstration of torque actuated fluid delivery. A) Scheme of TAP formation and actuation by the depression of the screw, displacing the fluid below. B) Calibration curve and results of dispensed volume trials (red) of measuring the change in hue from food dyes. Starting with yellow dye, hue increases with the addition of blue. The cluster of red points demonstrates the displacement of volume from six separate channels. Pictorial representation of HIA wells with hue increasing as blue dye is added to yellow dye.

proportionally with the volume of blue dye added. A calibration curve was created by adding 3 μL of blue dye in 0.25 μL increments to the yellow dye, followed by image capture and processing. The results from six separate trials showed that the TAP system was capable of reproducibly mobilizing 2 μL of fluid into the HIA reservoir with a variability of only 3.31% (**Fig. 2-13B**). This volume was attained through complete deformation of the elastomeric material by the TAP, which avoids any variability due to user-to-user differences in the degree to which the screw is turned. Accounting for unreacted master-mix in the channel upstream of the capillary valves, 1 μL of PCR product was transferred into the HIA reservoir, which is the volume of PCR product previously determined to be optimal for the HIA assay (1).

The TAP reagent delivery system allows us to avoid limitations associated with the Wiebel et, al. TWIST valve on a PDMS device (51). First, reagent evaporation through permeation is observed in PDMS, which would prevent successful PCR; we avoid this by adopting a PMMA substrate. Additionally, the hysteresis of the PDMS prevents much of the available liquid in a compartment from being released with the TWIST valve; this is not an issue with our PMMA device. Finally, the fabrication process to incorporate the single-use screws into the PDMS device for the TWIST valve is labor-intensive, whereas the multi-use TAP method utilizes simple one-time tapping of the PMMA manifold (which encases the microdevice) as the only extra ‘fabrication’ step required to incorporate the screws into the microfluidic system. This strategy of using a PMMA manifold to house the screws was also employed by Holcomb et al. to facilitate

torque-actuated valving (58); however, until now, this technique has not been demonstrated for fluid actuation and delivery.

2.3.3.3 Sealing and pressurization of the microdevice

The laser-ablated surface of the PMMA microdevice is rough, and thus prone to bubble formation (59). Therefore, sealing and pressurization of the device was required to prevent bubble expansion, which would drive the PCR reagents out of the chamber during thermal cycling. In previous work, sealing and pressurization was achieved using biocompatible film and a PMMA manifold; however, this was applied to seal inlets with a radius of 0.5 mm and proved insufficient for our TAP

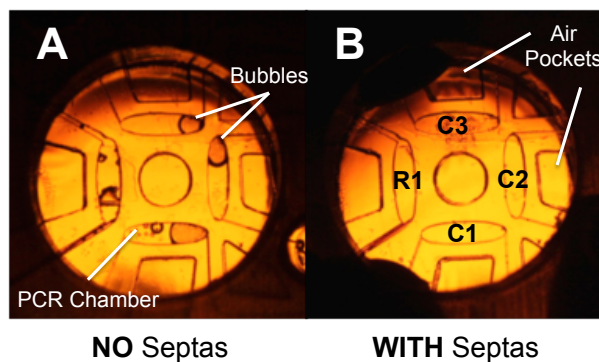


Figure 2-14. Top-view photographs of the PCR chambers at 95 °C. A) Bubbles are seen in the PCR chambers when no septa is applied. B) No bubbles are visible to the naked eye with the addition of a septa for additional pressurization. HIA chambers are positioned to the right of the chambers.

inlets with nearly 3X the surface area (1.33 mm radius) (**Fig. 2-14A**) (59). Therefore, an additional sealing component was required to prevent bubble expansion. Additional pressure was applied with a septum (conventionally used to seal sample vials in capillary electrophoresis) placed above the inlets. The combination of bio-film, septa, and a PMMA manifold successfully minimized bubble expansion in the PCR chambers at 95 °C, allowing PCR to be performed successfully (**Fig. 2-14B**). The silicone composition of the septa prevented any sample loss through the bio-film, and was easily deformed

with the application of the screw for fluid actuation. Importantly, due to the exceptional thermal stability of silicone, the elasticity of the septa is maintained even when exposed to the high temperatures required for PCR (60).

2.3.3.4 Capillary burst valves

In initial microdevice designs, the slight pressure that needed to be applied above the TAP inlets to assure sealing caused the premature movement of fluid through the PCR chamber, the microchannel, and into the HIA reservoirs. This can typically be avoided by applying even pressure across the device at all times; however, concurrently pressurizing the HIA reservoirs and PCR chambers would be challenging without the use of sophisticated pneumatic hardware. An alternative counter-pressurization scheme was used to immobilize the PCR reagents in the channel, based on a geometric capillary burst valve. The basis of this valve design stems from a previously reported “fishbone valve” (61) involving the widening of a microchannel at a 90° angle to the direction of the flow; this creates the necessary surface tension to halt fluid flow. Such valves have been created in PMMA by laser-ablation using a rastering technique (54). However, for effective valving, these require channels with a minimum dimension at the valve junction of 240 μm (w) x 600 μm (d), thus resulting in large dead-volumes (i.e., unreacted PCR reaction mix) that may be problematic for the downstream chemistry. Furthermore, our experience indicates that laser ablation systems can lack the necessary precision to connect vector and raster ablated channels in the same plane (i.e., micron-scale resolution). For these reasons, we adapted the fishbone valve approach, using vector

etching to create an opening perpendicular to the channel, reducing dead-volume and fabrication errors. Two burst valves in sequence were used, the second as a ‘back-up’ valve should the first valve be breached (**Fig. 2-15**). Notably, we never experience failure of the second valve with this device, while the failure rate of the first valve is ~5%. To minimize bubble formation caused by sharp corners in the microfluidic geometry, the valve was created with an oval shape and a depth of 170 μm – this was the minimal channel depth that could be reproducibly laser-ablated without channel collapse during thermal bonding. The valve was determined to burst at 0.4 PSI (2758 Pa), which is exceeded by the TAP to facilitate fluid movement to the detection chamber following PCR.

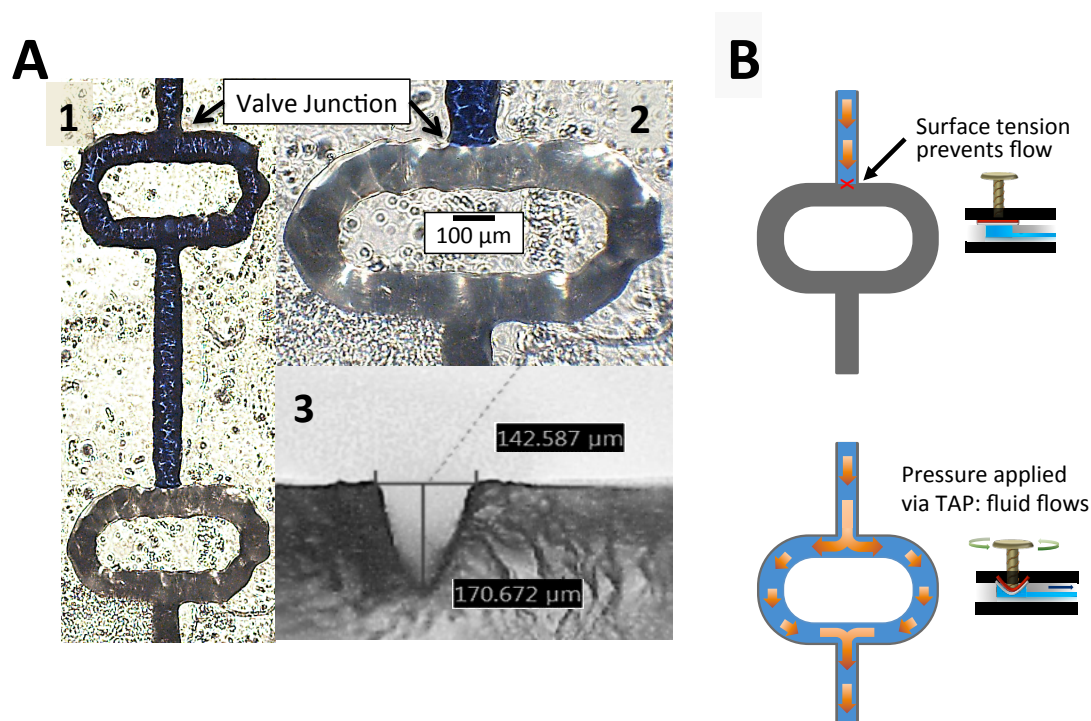


Figure 2-15. Capillary burst valve characterization. A) Microscope images of the capillary valve and channel shape and depth in PMMA. A1) Image demonstrating that if the first valve is broken, the second valve will hold. A2) Close-up of the valve preventing fluid flow through surface tension. A3) Cross-sectional view of the channel architecture in the device. All channels are ~150 μm wide and ~170 μm deep. B) Schematic demonstrating the principles of fluidic control using the capillary valve and TAP system.

2.3.3.5 HIA detection

Once PCR amplification is completed, 1 μL volume of PCR product is mobilized to the HIA chamber for exposure to the oligonucleotide probe-adducted paramagnetic particles. Note that the HIA chambers were positioned 10 mm from the edge of the IR focal spot to minimize the effect of heating during PCR. As reported previously (1,47,62,63), hybridization of the particle-bound probes to the amplified DNA in the presence of a rotating magnetic field (RMF) leads to particle aggregation. The single large bar magnet used previously was replaced with individual 2 mm³ neodymium magnets positioned under each HIA detection chamber (**Fig. 2-16**). The magnets were encased in a machined PMMA holder connected to a small motor to induce automated movement of the magnets

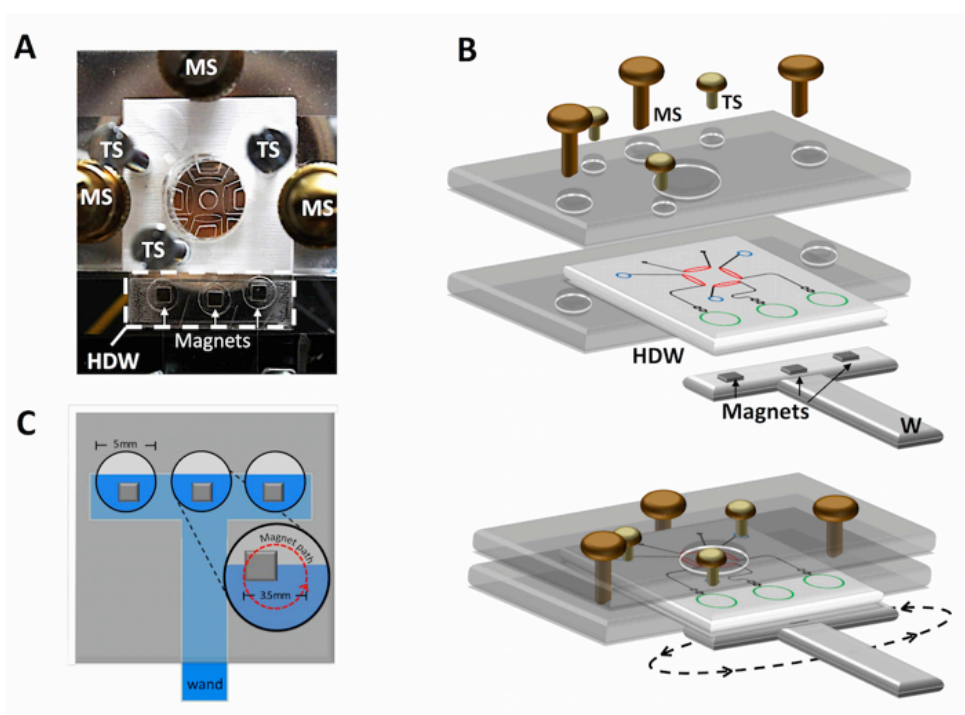


Figure 2-16. Placement of discrete individual magnetic field for HIA detection. A) Top-view photograph of the HIA chambers with individual magnets below. B) Scheme of microdevice held in manifold following pressurization with placement of the magnets held in a PMMA cross-T. C) Scheme of 2 mm² magnets rotating within a 3.5 mm diameter. MS, manifold screw; TS, TAP screw; HDW, HIA detection well; W, rotating magnetic wand.

in a circular path beneath each HIA chamber. To avoid magnetic field cross-talk (magnet from one chamber affecting another chamber), the radius of rotation for each magnet required confinement to 3.5 mm underneath the 2.5 mm (radius) HIA well (**Fig. 2-16C**). By applying a magnetic field in this manner, the particle aggregation in the presence of target sequence (or dispersion in the absence of target) was complete in 30 seconds, allowing for rapid, specific DNA detection.

*2.3.3.6 Integrated amplification and detection of *Salmonella enterica**

To demonstrate functionality in an integrated format, however rudimentary, PCR amplification followed by direct bead aggregation detection was evaluated with the detection of *Salmonella enterica* in a sample. Using the same PCR protocol and reagents/primers used to generate the data in **Figure 2-12B** (and described in *Materials and Methods*), 32 cycles of IR-PCR was performed in only 34 minutes (57, 64). In these analyses, the four chambers were utilized for thermocycling of positive control, negative control, test sample, and the reference chamber for temperature control (C3, C2, C1, and R1, respectively in **Fig. 2-12A**). In both the positive control and test sample chambers, 1 ng of pre-purified bacterial DNA was thermocycled. Following PCR, the HIA detection chambers were manually filled with HIA buffer and the oligonucleotide-bound particles. (Note that HIA reagents were not pre-loaded due to evaporation effects during PCR). TAP was initiated, moving any generated PCR products through the burst valves into the HIA chambers, where rotation of the mounted magnets at 150 rpm for 30 seconds enhanced the target-particle interaction. While aggregation was obvious to the naked

eye, a custom algorithm was used to objectively evaluate the degree of aggregation (**Fig. 2-17**). With HIA, the greater the extent of aggregation, the larger the number of target molecules per unit volume in the sample. The software filters out the background, so only the aggregated particles are counted as pixels (**Fig 2-17B**). This showed that the test sample had a 99 % Aggregation value that was comparable to the *Salmonella* positive control, while negative control resulted in a minimal HIA response (p value=0.002), confirming the presence of *Salmonella enterica* DNA in the sample (**Fig. 2-17C**). These experiments represent the first instance of integrating PCR with HIA detection on a single microdevice.

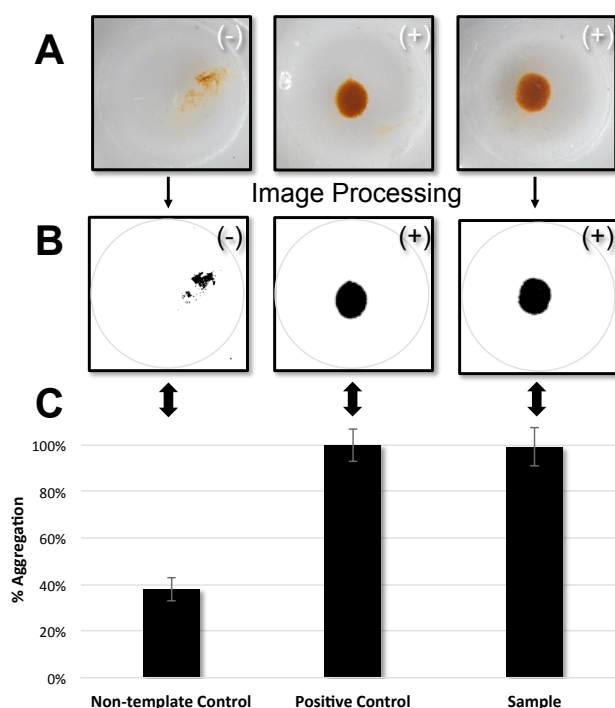


Figure 2-17. Integrated analysis for the detection of *Salmonella enterica*. A) Images of HIA well showing the extent of aggregation after exposure to a RMF for 30 seconds. B) Images showing algorithmic conversion into the pixelized image that provides semi-quantitative information. C) Bar graph generated from algorithm analysis of the aggregation in (B). For $n=3$, % CV for Non-template Control, Positive Control and Sample were 5, 9 and 8% respectively.

2.3.4 Conclusions

This work describes key advances for the future integration of chemical processes on a single microdevice suitable for POC NAT. Presented here is the development of a novel PMMA microdevice that integrates two simple, inexpensive and novel analytical processes, IR-PCR and HIA detection. The multiplex format of the device allows for the inclusion of on-chip assay standards, enhancing the reliability of detection. Additionally, the capability for a visual read-out permits immediate interpretation of the results by the user and eliminates the need for additional instrumentation, which keeps costs low and portability high. Highly simplistic fluidic control was established, without the use of additional fabrication steps or peripheral instrumentation – this is key cost-efficiency in commercialization for rural or global health. The functionality of the device was shown with the successful detection of *Salmonella enterica* DNA in under 35 minutes. These results are a significant step to creating a functional, portable, easy-to-use POC microdevice for bacterial organisms or other relevant DNA targets.

2.4 Concluding Remarks

The work presented in this chapter represents significant progress in the expansion of previous discovery of novel technologies for DNA detection/quantification based on DNA aggregation. Two critical features of attractive analytical technologies, especially for POC applications, are made possible in this work: multiplex capabilities (*part one*)

and integration of multiple analytical processes (*part two*). Importantly, the DFA system developed in *part one* serves as the primary instrumentation used in the work that follows.

2.5 References

1. D.C. Leslie, J. Li, B.C. Strachan, M.R. Begley, D. Finkler, L.A.L. Bazydlo, N.S. Barker, D.M. Haverstick, M. Utz, J.P. Landers, *Journal of the American Chemical Society* 134 (2012) 5689.
2. N.P. Singh, M.T. McCoy, R.R. Tice, E.L. Schneider, *Experimental Cell Research* 175 (1988) 184.
3. B. Budowle, F.S. Baechtel, C.T. Comey, A.M. Giusti, L. Klevan, *Electrophoresis* 16 (1995) 1559.
4. M. Piatak, K.C. Luk, J.D. Lifson, *Biotechniques* 14 (1993) 70.
5. K.N. Ballantyne, R.A.H. van Oorschot, R.J. Mitchell, *Forensic Science International* 166 (2007) 35.
6. C.T. Wittwer, M.G. Herrmann, A.A. Moss, R.P. Rasmussen, *Biotechniques* 22 (1997) 130.
7. S.M. Shim, J.H. Kim, S.E. Jung, D.J. Kim, J.H. Oh, B.G. Han, J.P. Jeon, *Biopreservation and Biobanking* 8 (2010) 187.

8. H.Y. Lee, M.J. Park, N.Y. Kim, J.E. Sim, W.I. Yang, K.-J. Shin, *Forensic Science International: Genetics* 4 (2010) 275.
9. K. Sturk-Andreaggi, T.M. Diegoli, R. Just, J. Irwin, *Forensic Science International: Genetics Supplement Series* 3 (2011) e504.
10. T. Demeke, G.R. Jenkins, *Analytical and Bioanalytical Chemistry* 396 (2010) 1977.
11. S. Amory, R. Huel, A. Bilić, O. Loreille, T.J. Parsons, *Forensic Science International: Genetics* 6 (2012) 398.
12. S. Witt, J. Neumann, H. Zierdt, G. Gébel, C. Röscheisen, *Forensic Science International: Genetics* 6 (2012) 539.
13. D. White, Butler, B., Creswell, D., Smith, C., *Promega Notes* (1998) 12.
14. C.J. Frégeau, C.M. Lett, R.M. Fourney, *Forensic Science International: Genetics* 4 (2010) 292.
15. C.R. Reedy, J.M. Bienvenue, L. Coletta, B.C. Strachan, N. Bhatni, S. Greenspoon, J.P. Landers, *Forensic Science International-Genetics* 4 (2010) 206.
16. J.M. Bienvenue, L.A. Legendre, J.P. Ferrance, J.P. Landers, *Forensic Science International-Genetics* 4 (2010) 178.
17. N. Pamme, *Lab on a Chip* 6 (2006) 24.
18. S.H. Lee, D. van Noort, J.Y. Lee, B.-T. Zhang, T.H. Park, *Lab on a Chip* 9 (2009) 479.
19. Y. Moser, T. Lehnert, M.A. Gijs, *Lab Chip* 9 (2009) 3261.

21. K.A. Melzak, C.S. Sherwood, R.F.B. Turner, C.A. Haynes, *Journal of Colloid and Interface Science* 181 (1996) 635.
22. A. Sassolas, B.D. Leca-Bouvier, L.J. Blum, *Chemical Reviews* 108 (2008) 109.
23. Y. Sun, Y.C. Kwok, N.T. Nguyen, *Journal of Micromechanics and Microengineering* 16 (2006) 1681.
24. A. Niemz, T. M. Ferguson and D. S. Boyle, *Trends in Biotechnology*, 2011, 29, 240-250.
25. C. A. Holland and F. L. Kiechle, *Current Opinion in Microbiology*, 2005, 8, 504-509.
26. C. Duarte, E. Salm, B. Dorvel, B. Reddy, Jr. and R. Bashir, *Biomed Microdevices*, 2013, DOI: 10.1007/s10544-013-9769-5, 1-10.
27. P. Yager, G. J. Domingo and J. Gerdes, *Annual Review of Biomedical Engineering*, 2008, 10, 107-144.
28. T. M.-H. Lee and I. M. Hsing, *Analytica Chimica Acta*, 2006, 556, 26-37.
29. P. Craw and W. Balachandran, *Lab on a Chip*, 2012, 12, 2469-2486.
30. L. Chen, A. Manz and P. J. R. Day, *Lab on a Chip*, 2007, 7, 1413-1423.
31. C. A. Baker, C. T. Duong, A. Grimley and M. G. Roper, *Bioanalysis*, 2009, 1, 967-975.
32. G. T. Walker, M. S. Fraiser, J. L. Schram, M. C. Little, J. G. Nadeau and D. P. Malinowski, *Nucleic acids research*, 1992, 20, 1691-1696.

33. J. Compton, *Nature*, 1991, 350, 91-92.
34. A. Fire and S. Q. Xu, *Proceedings of the National Academy of Sciences*, 1995, 92, 4641-4645.
35. C. Zhang and D. Xing, *Nucleic acids research*, 2007, 35, 4223-4237.
36. Y. Zhang and P. Ozdemir, *Analytica Chimica Acta*, 2009, 638, 115-125.
37. S. Park, Y. Zhang, S. Lin, T.-H. Wang and S. Yang, *Biotechnology Advances*, 2011, 29, 830-839.
38. C. J. Easley, J. M. Karlinsey and J. P. Landers, *Lab on a Chip*, 2006, 6, 601-610.
39. M. G. Roper, C. J. Easley, L. A. Legendre, J. A. C. Humphrey and J. P. Landers, *Analytical Chemistry*, 2007, 79, 1294-1300.
40. D. Le Roux, B. E. Root, J. A. Hickey, O. N. Scott, A. Tsuei, J. Li, D. J. Saul, L. Chassagne, J. P. Landers and P. de Mazancourt, *Lab Chip*, 2014, 14, 4415-4425.
41. M. A. Burns, B. N. Johnson, S. N. Brahmasandra, K. Handique, J. R. Webster, M. Krishnan, T. S. Sammarco, P. M. Man, D. Jones, D. Heldsinger, C. H. Mastrangelo and D. T. Burke, *Science*, 1998, 282, 484-487.
42. E. T. Lagally, C. A. Emrich and R. A. Mathies, *Lab on a Chip*, 2001, 1, 102-107.
43. D. Trau, T. M. Lee, A. I. Lao, R. Lenigk, I. M. Hsing, N. Y. Ip, M. C. Carles and N. J. Sucher, *Anal Chem*, 2002, 74, 3168-3173.
44. R. C. Anderson, X. Su, G. J. Bogdan and J. Fenton, *Nucleic acids research*, 2000, 28, e60.
45. M. A. Northrup, B. Benett, D. Hadley, P. Landre, S. Lehew, J. Richards and P. Stratton, *Anal Chem*, 1998, 70, 918-922.

46. J. G. Lee, K. H. Cheong, N. Huh, S. Kim, J. W. Choi and C. Ko, *Lab Chip*, 2006, 6, 886-895.
47. B. C. Strachan, H. S. Sloane, J. C. Lee, D. C. Leslie and J. P. Landers, *Analyst*, 2015, 140, 2008-2015.
48. K. Xu, M. R. Begley and J. P. Landers, *Lab on a Chip*, 2015, 15, 867-876.
49. K. Iwai, K. C. Shih, X. Lin, T. A. Brubaker, R. D. Sochol and L. Lin, *Lab on a Chip*, 2014, 14, 3790-3799.
50. W. Li, T. Chen, Z. Chen, P. Fei, Z. Yu, Y. Pang and Y. Huang, *Lab on a Chip*, 2012, 12, 1587-1590.
51. D. B. Weibel, M. Kruithof, S. Potenta, S. K. Sia, A. Lee and G. M. Whitesides, *Analytical Chemistry*, 2005, 77, 4726-4733.
52. M. A. Unger, H.-P. Chou, T. Thorsen, A. Scherer and S. R. Quake, *Science*, 2000, 288, 113-116.
53. J. Melin and S. R. Quake, *Annu Rev Biophys Biomol Struct*, 2007, 36, 213-231.
54. M. I. Mohammed, E. Abraham and M. P. Y. Desmulliez, *Journal of Micromechanics and Microengineering*, 2013, 23, 035034.
55. A. L. Brogger, D. Kwasny, F. G. Bosco, A. Silahtaroglu, Z. Tumer, A. Boisen and W. E. Svendsen, *Lab on a Chip*, 2012, 12, 4628-4634.
56. A. S. Patterson, D. M. Heithoff, B. S. Ferguson, H. T. Soh, M. J. Mahan and K. W. Plaxco, *Appl Environ Microbiol*, 2013, 79, 2302-2311.

57. J. A. Lounsbury, A. Karlsson, D. C. Miranian, S. M. Cronk, D. A. Nelson, J. Li, D. M. Haverstick, P. Kinnon, D. J. Saul and J. P. Landers, *Lab on a Chip*, 2013, 13, 1384-1393.
58. R. E. Holcomb, L. J. Mason, K. F. Reardon, D. M. Cropek and C. S. Henry, *Anal Bioanal Chem*, 2011, 400, 245-253.
59. J. A. Lounsbury, B. L. Poe, M. Do and J. P. Landers, *Journal of Micromechanics and Microengineering*, 2012, 22, 085006.
60. C. L. Joost, O. Wouter, H. V. Peter and B. Piet, *Journal of Micromechanics and Microengineering*, 1996, 6, 52.
61. C. Lu, Y. Xie, Y. Yang, M. M. C. Cheng, C.-G. Koh, Y. Bai, L. J. Lee and Y.-J. Juang, *Analytical Chemistry*, 2006, 79, 994-1001.
62. D. A. Nelson, B.C. Strachan, Briony, H.S. Sloane, J. Li, J.P. Landers, *Analytica Chimica Acta*, 2014, Accepted, Jan 2014.
63. H. S. Sloane, K. A. Kelly and J. P. Landers, *Anal Chem*, 2015, DOI: 10.1021/acs.analchem.5b01876.
64. J. A. Lounsbury, N. Coult, D. C. Miranian, S. M. Cronk, D. M. Haverstick, P. Kinnon, D. J. Saul and J. P. Landers, *Forensic Science International: Genetics*, 2012, 6, 607-615.

3 Development of a Novel Analytical Strategy for Rapid *KRAS* Mutation Detection using Hybridization-Induced Aggregation

3.1 Overview

KRAS mutations have emerged as powerful predictors of response to targeted therapies in the treatment of lung and colorectal cancers; thus, prospective *KRAS* genotyping is essential for appropriate treatment stratification. Conventional mutation testing technologies are not ideal for routine clinical screening, as they often involve complex, time-consuming processes and/or costly instrumentation. In response, a unique analytical strategy for revealing *KRAS* mutations was developed, based on the allele-specific hybridization-induced aggregation (HIA) of oligonucleotide probe-conjugated microbeads. HIA utilizes a pair of sequence-specific oligonucleotide probes bound to magnetic microbeads. Hybridization to a target DNA strand tethers the beads together, inducing bead aggregation. By simply using the extent of bead aggregation as a measure of the hybridization efficiency, additional labels and sophisticated analytical equipment are avoided. Through strategic manipulation of the assay design and experimental parameters, HIA is used to facilitate, for the first time, the detection of single base mutations in a gene segment, and specifically, the detection of activating *KRAS* mutations in human cancers. The bead-bound oligonucleotide probes were designed with perfect complementarity to the wild-type *KRAS* gene segment; therefore, the presence of any of

the common *KRAS* mutations (located in codons 12 and 13) in a target reduces the stability of the hybridization complex, resulting in decreased bead aggregation. This unique approach allows for the detection of any of the common *KRAS* mutations in a single-step, 2-minute assay, using only one set of oligonucleotide probes. The assay is performed at room temperature and uses simple, inexpensive instrumentation with a reusable plastic microwell chip that permits multiplexed analysis.

Following development and optimization of the HIA method for Mutation Detection (HIA_{MD}), the clinical utility of this approach was demonstrated. In the analysis of 20 lung and colon tumor pathology specimens, a 100% correlation between the *KRAS* mutation statuses determined by HIA_{MD} and sequencing was observed. In addition, *KRAS* mutations were detectable in a background of 75% wild-type DNA – a finding in line with that reported for sequencing. With this, it is shown that HIA_{MD} allows rapid and cost-effective *KRAS* mutation detection without compromising analytical performance. These results indicate the validity of HIA_{MD} as a mutation testing technology suitable for practical clinical testing.

3.2 Introduction

Advances in understanding the genetic basis of cancer have heralded a new era of clinical oncology, and with it, the prospect of a patient-centered model of cancer care. Specifically, the identification and functional analysis of tumor-specific genetic

alterations has opened exciting opportunities to exploit genetic mutations as predictors of therapeutic response and guide, in unprecedented ways, a more effective patient treatment regime (1). A compelling example of this has been the emergence of *KRAS* mutations as powerful predictive biomarkers of treatment sensitivity in patients with colorectal cancer (CRC) and non-small cell lung cancer (NSCLC) (2).

Approximately 30-40% of CRC and 20% of NSCLC tumors are known to harbor *KRAS* point mutations, occurring almost always in codons 12 or 13 (3). These mutations render the KRAS protein constitutively GTP-bound and active, and consequently, lead to stimulus-independent, persistent activation of downstream effectors to promote cell proliferation, survival, and metastasis (4). This provides a mechanism to bypass the anti-tumor effect of therapeutic strategies directed to the epidermal growth factor receptor (EGFR), an upstream receptor tyrosine kinase in the KRAS pathway (**Fig. 3-1**) (5). Indeed, numerous clinical studies have demonstrated that response to anti-EGFR therapies (including the monoclonal antibody therapies *cetuximab* and *panitumumab* as well as the tyrosine kinase inhibitors *gefitinib* and *erlotinib*) is limited to patients harboring tumors with wild-type *KRAS* (2, 3, 6-13). Given the overwhelming evidence, it is clear that the assessment of *KRAS* mutation status is an essential strategy in increasing the efficiency of treatment allocation for CRC and NSCLC patients, to improve outcomes and reduce costs (14). Additionally, *KRAS* genotyping for population stratification will likely be key in accelerating the development of novel inhibitors of this key oncogenic pathway (15,16).

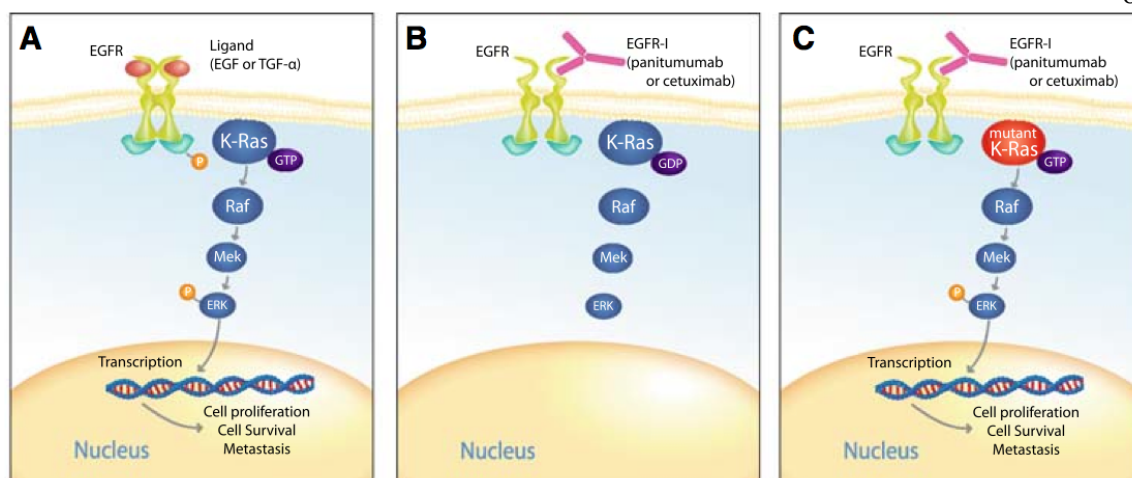


Figure 3-1. The KRAS gene product functions as a GTP/GTP-regulated binary on-off switch. In normal quiescent cells, KRAS is GDP-bound and inactive. Stimulation of epidermal growth factor receptor (EGFR) causes transient formation of the active, GTP-bound form of KRAS, which facilitates cellular proliferation through the activation of downstream effectors (A). By inhibiting EGFR, KRAS is inactivated by the hydrolysis of bound GTP to GDP, therefore inhibiting downstream signaling (B). Mutant KRAS genes result in amino acid substitutions that impair intrinsic and GAP-mediated GTP hydrolysis, rendering the protein constitutively GTP-bound and active. Thus, the inhibition of EGFR has no inhibitory effect on downstream signaling and cell proliferation (C). Figure taken from (5).

It has recently been advocated that *KRAS* testing be incorporated into routine practice for all CRC patients at the time of initial diagnosis (i.e., reflex testing), as the current process of retrospective *KRAS* testing is cumbersome, time-consuming, and error-prone (17). Although reflex testing appears an ideal scenario, its implementation raises questions about practicality. While a number of technologies have been used for *KRAS* mutation analysis, including Sanger sequencing, pyrosequencing, and high-resolution melting (HRM) analysis, it is unclear whether any current methodology could be applied in a low-maintenance (i.e., operation by unskilled personnel and easy to interpret) and economically sound manner. Sanger sequencing is considered to be the gold standard, yet it has the highest turn around time and the most hands-on time of these methods (18). HRM analysis can be run considerably faster than other methods; however, it requires

costly instrumentation (19) and is often associated with unreliable results (20,21). Pyrosequencing methods may have relatively lower costs per assay, but the instrumentation is the most costly to purchase and maintain (19,22). Other technologies designed to reveal SNPs are based on the principle of allele-specific hybridization, which relies on the ability of oligonucleotide probes to bind selectively to target DNA sequences. The implementation of this methodology on a “DNA chip” has gained popularity, due to the considerable advantages offered by a microfluidic platform, including low reagent consumption, minimal input requirements of precious patient samples, and high throughput capabilities (23). Characteristically, DNA chips (including microarray platforms) involve oligonucleotide probes immobilized on the chip surface, which introduce fundamental limitations to these methods. First, a long analysis time (usually many hours) is required, since the hybridization reaction depends solely on the diffusion of target sequences to surface-bound probes (24). Additionally, typical DNA chips require complicated and expensive fabrication processes to immobilize oligonucleotide probes on a surface (25-27). The most notable limitations, however, are associated with the detection method employed, as mentioned in reference to other mutation detection methods. The highly sensitive nature of hybridization assays with single base discriminatory capabilities requires a comparably sensitive detection method to reveal the small changes in analytical signal produced by a single nucleotide mismatch. This often translates to expensive reagents (e.g., fluorescent, chemiluminescent, or radioactive labels) and sophisticated analytical instrumentation (26,28,29), which substantially limit the practicality of the method for a routine clinical setting.

The limitations associated with these methods provide a substantial barrier to their implementation in the routine clinical setting, where speed, simplicity, and cost-effectiveness are not only preferable, but essential. In an effort to fulfill the unmet clinical demand for a methodology amenable to the requirements of routine testing, a novel approach for the detection of point mutations is introduced. This work addresses the analytical and technical challenges of developing a methodology that is sensitive enough to reveal a single nucleotide mismatch in a gene segment, while maintaining simplicity in both the analytical process and instrumentation required.

The method developed here builds on a hybridization-based technique for sequence-specific DNA detection previously developed in the Landers lab, called hybridization-induced aggregation (HIA) (30). HIA takes a dual hybridization approach, involving a pair of magnetic bead-bound oligonucleotide probes. The hybridization of the complementary target sequence to the probe sequences tethers the beads together and induces bead aggregation. The in-house engineered HIA instrumentation set-up was assembled using a unique combination of a commercial vortexer (for gentle agitation) and a rotating magnet (derived from a conventional laboratory stir plate). The use of a dual-force approach (31) (described in **Chapter 2**) facilitates highly efficient interaction of target DNA with probe sequences, thus enhancing hybridization kinetics in a multiwell chip, so that the hybridization assay is complete in minutes. The assay presented in this work is reduced from 12 minutes (32) to only 2 minutes. The speed of the HIA assay provides a unique discriminator over other technology platforms and presents the possibility for use in diagnostic testing and routine mutation screening.

The HIA assay is performed using a simple, plastic microwell chip. The chip is custom made to fit the vortexer and features a circular array of 12 microwells, designed such that the rotating magnetic field strength is consistent across all wells. The chip can be rapidly fabricated at a cost of pennies per chip, and can be subsequently used in repeated experiments, indefinitely. This makes the technique less expensive, less time-consuming, and more versatile than microarrays and other oligonucleotide-immobilized chip platforms, since the analysis of a different gene segment does require a separate chip to be fabricated. Only one, universal chip is needed for any HIA assay, regardless of the target or mutation in question.

The use of microbeads for direct visual detection of hybridization (through aggregation) avoids the need for fluorescent labels and complex analytical equipment. Capture of a digital image of the reaction well following exposure of the sample DNA to the microbead-bound probes allows for quantitative information to be extracted, where the extent of aggregation is measured by image “saturation” and a simple algorithm. [Note: here, “saturation” is synonymous to “dark area” used to describe image analysis in **Chapter 2.**] As shown in **Figure 3-2**, in the absence of target DNA, the beads remain dispersed in the microwell, which generates a high image saturation value. When the beads are aggregated, the “saturated area” in the microwell is reduced, corresponding to a lower image saturation value. Therefore, the extent of aggregation is inversely related to saturation.

In the work presented here, HIA technology is exploited to allow, for the first time, the detection of a single base change in a gene segment, and specifically, the

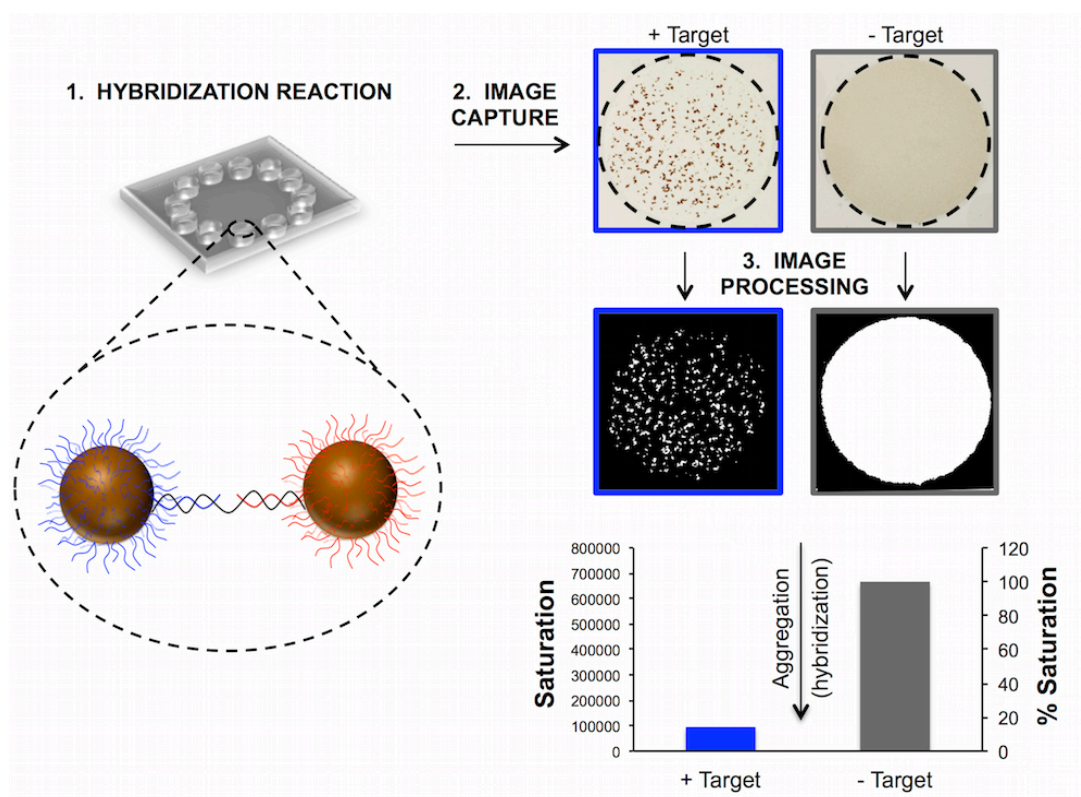


Figure 3-2. HIA assay principles. A pair of magnetic bead bound probes interact with target DNA in a microwell. The hybridization of the target sequence (black) to the probe sequences (red and blue) tethers the beads together and induces bead aggregation. An image of each microwell is then taken, and through image processing, the extent of aggregation is measured by image saturation. The extent of aggregation is inversely related to saturation.

detection of *KRAS* mutations in human cancers. In principle, a HIA-based method for mutation detection (HIA_{MD}) relies on differences in the thermal stabilities of perfectly matched and mismatched target-probe pairs to achieve allelic discrimination. Despite extensive knowledge about nucleic acid hybridization, meticulous empirical evaluation and assay-specific heuristics are required to establish the conditions that will ultimately permit two sequences differing by a single base to be distinguished (33). Key parameters affect the thermodynamics of duplex formation and, therefore, these were acutely considered in the development and optimization of this assay. These included probe

design, buffer composition (as a function of ionic strength and formamide concentration), and target parameters.

Upon development and optimization of the assay, it was applied for the detection of *KRAS* mutations in cancer cell lines. With the understanding that the analysis of patient tumor samples requires mutation detection in a background of wild-type DNA, the ability of HIA_{MD} to detect *KRAS* mutations in low abundance was investigated. Finally, this method was applied for *KRAS* mutation analysis of 20 colorectal and lung patient tumors, and these results were compared to those obtained from sequencing.

3.3 Methods and Materials

3.3.1 Oligonucleotides.

Synthetic target sequences, biotinylated probe sequences, and PCR primers were synthesized by Eurofins MWG Operon (Huntsville, AL). All oligonucleotide sequences are listed in **Table 3-1**.

3.3.2 Cell lines and cDNA synthesis

Cell lines (listed in **Table 3-2**) were purchased from the American Type Culture Collection. cDNA was synthesized from cultured cells using the FastLane Cell cDNA Kit (Qiagen, Venlo, Limburg), according to the manufacturer's instructions.

Oligonucleotide	Sequence*
PCR primers	
HIA _{MD} vs. 1 fwd	TGAATATAAACTTGTGGTAGTTGGAG
HIA _{MD} vs. 1 rev	TATCGTCAAGGCACTCTTGC
HIA _{MD} vs. 2 fwd	GACTGAATATAAACTTGTGGTAGTTGGA
HIA _{MD} vs. 2 rev	CATATTCGTCCACAAAATGATTCTG
Sequencing fwd	GAGAATTCATGACTGAATATAAACTTGT
Sequencing rev	TCGAATTCCTCTATTGTTGGATCATATTCG
Targets	
50-base, A	GCATCGGGGGAATTCTACGCCTCGAGTGCAGCCCAGGA ACTACTAGCGAA
50-base, B	GCATCGGGGGAATTCTACGaCTCGAGTGCAGCCCAGGA ACTACTAGCGAA
50-base, C	GCATCGGGGGAATTCTACGCCTCGAtTGCAGCCCAGGA ACTACTAGCGAA
50-base, D	GCATCGGGGGAATTCTACGaCTCGAGTaCAGCCCAGGAA CTACTAGCGAA
50-base E	GCATCGGGGGAATTCTACtaCTCGAGTGCAGCCCAGGAA CTACTAGCGAA
58-base, <i>KRAS</i> wt	TGAATATAAACTTGTGGTAGTTGGAGCTGGTGGCGTAG GCAAGAGTGCCTTGACGATA
58-base, <i>KRAS</i> mut	TGAATATAAACTTGTGGTAGTTGGAGCTGATGGCGTAGG CAAGAGTGCCTTGACGATA
95-base, <i>KRAS</i> wt	GACTGAATATAAACTTGTGGTAGTTGGAGCTGGTGGCGT AGGCAAGAGTGCCTTGACGATACAGCTAATTCAGAATC ATTTTGTGGACGAATATG
95-base, <i>KRAS</i> mut	GACTGAATATAAACTTGTGGTAGTTGGAGCTtGTGGCGT AGGCAAGAGTGCCTTGACGATACAGCTAATTCAGAATC ATTTTGTGGACGAATATG
Probes	
50-base target, 5'	[Biotin_TEG]TTTTTTTATGTGGTCTATGTCGTCGTTTCGCTA GTAGTTCCTGGGCTGCAC
50-base target, 3'	TCGAGGCGTAGAATTCCCCCGATGCGCGCTGTTCTTACT CATTTTT[Biotin_TEG-Q]
58-base target, 5'	CCACCAGCTCCAACCTACCAC [Biotin_TEG~Q]

Table 3-1. Oligonucleotide sequences. *All sequences are listed 5' to 3'.

Oligonucleotide	Sequence*
58-base target, 3'	[Biotin_TEG] TATCGTCAAGGCACTC
95-base target, DP-1	CTACGCCACCAGCTCTTTTTT[Biotin_TEG~Q]
95-base target, DP-2	CTACGCCtCCAGCTCTTTTTT[Biotin_TEG~Q]
95-base target, SP	[Biotin_TEG]TTTTTTCTGAATTAGCTGTATCGTCAAGGCA CTC

*Table 3-1 cont'd. Oligonucleotide sequences. *All sequences are listed 5' to 3'.*

Cell line	Cancer classification	KRAS mutation status
CaCo2	Colorectal carcinoma	Wild-type
H1975	Lung adenocarcinoma	Wild-type
H522	Non-small cell lung adenocarcinoma	Wild-type
BxPC-3	Pancreatic adenocarcinoma	Wild-type
A549	Lung carcinoma	c.34G>A p.G12S
MIA PaCa-2	Pancreatic carcinoma	c.34G>T p.G12C
SW-620	Colorectal carcinoma	c.35G>T p.G12S
H2122	Non-small cell lung adenocarcinoma	c.34G>T p.G12C

Table 3-2. Cell lines.

3.3.3 Tumor samples

20 frozen surgical resections (10 lung and 10 colon) were obtained from pathology through the Biorepository and Tissue Research Facility at The University of Virginia. The samples were coded and collected under IRB protocol. Sample characteristics are found in **Table 3-3**. The samples were divided into 2 groups of 10 (each including 5 lung and 5 colon) for RNA isolation. While genomic DNA could have also been used as the input nucleic acid, it has been suggested that RNA may actually be preferred over genomic DNA for mutation analysis from frozen tissue samples (34). The first group of samples (patient IDs: 1,3,5,10,12,13,18,19, and 20) was prepared using the *mirVana*TM miRNA Isolation Kit (Life Technologies, Carlsbad, CA) for total RNA isolation, and the second group (patient IDs: 2,6,7,8,9,11,14,15,16, and 17) was prepared using the RNeasy Mini Kit (Qiagen, Venlo, Limburg). The concentration and purity of the RNA products were estimated using a NanoDrop 2000 spectrophotometer (Thermo Scientific, Wilmington, DE). RNA was then converted to cDNA using the QuantiTect Reverse Transcription Kit (Qiagen, Venlo, Limburg). Approximately 1 µg of RNA was used in each 20 µL reverse transcription reaction.

3.3.4 Sequencing

PCR reactions were composed of 1X MyTaq Reaction Buffer (Bioline Reagents Ltd, London, UK), 0.4 µM primers, 0.05 U/µL MyTaq HS DNA Polymerase (Bioline Reagents Ltd, London, UK), and 10%/v template cDNA. A GeneAmp PCR System 2700 thermal cycler (Applied Biosystems, Foster City, CA) was used with the following

thermocycling conditions: 2 minutes at 95°C, followed by 45 cycles of 15 seconds at 95°C, 30 seconds at 57° C, and 30 seconds at 72°C, then finally, 2 minutes at 72° C. PCR products were analyzed using Agilent 2100 DNA 1000 Series II kits and instrumentation (Agilent Technologies, Santa Clara, CA) to confirm amplification and estimate amplicon concentration. The products were then purified using the QIAquick PCR Purification Kit (Qiagen, Venlo, Limburg). Sequencing was performed by Eurofins Genomic (Huntsville, AL) using the reverse sequencing PCR primer.

3.3.5 PCR

3.3.5.1 Initial PCR with version 1 primers

PCR was performed using AmpliTaq Gold® DNA Polymerase reagents (Applied Biosystems, Foster City, CA). 25 µL reactions were composed of 1.2X PCR Buffer II, 5mM MgCl₂, 0.2 µM dNTPs, 0.8 µM primers, and 0.1 U/µL AmpliTaq Gold polymerase. The positive DNA control (**Fig. 3-7A**) contained 1 ng/µL hgDNA. The synthetic template control (**Fig. 3-9A**) contained 4x10⁵ copies/µL of synthetic target (58 bp). PCR was performed on a GeneAmp PCR System 2700 thermal cycler (Applied Biosystems, Foster City, CA), under the following thermocycling conditions: 11 minutes at 95°C, followed by 40 cycles of 30 seconds at 95°C, 30 seconds at 45° C, and 30 seconds at 72°C, then finally, 10 minutes at 72° C. The PCR products were analyzed using Agilent 2100 DNA 1000 Series II kits and instrumentation (Agilent Technologies, Santa Clara, CA) to confirm amplification.

3.3.5.2 Real-time PCR and quantitative PCR

Real-time PCR was performed using a CFX Connect Real-Time PCR Detection System (Bio-Rad, Hercules, CA). Reactions were composed of 12.5 µL SYBR Green Real-Time PCR Master Mix (Applied Biosystems, Foster City, CA), 1 µL primers (20 µM), 1.5 µL H₂O, and 10 µL template (cDNA prepared from cell lysates). Reactions were performed under the following thermal cycling conditions: 2 minutes at 95°C, followed by 50 cycles of 10 seconds at 95°C and 30 seconds at 55° C (for vs. 1 primers) or 58° C (for vs. 2 primers). Immediately after the real-time PCR run, melting curves were generated. For qPCR, a standard curve was generated using varying concentrations (10¹², 10¹⁰, 10⁸, 10⁶, 10⁴, and 10² copies/µL) of synthetic template (wild-type) as the templates for real-time PCR reactions. qPCR analysis was performed using a threshold of 20 rfu.

3.3.5.3 Optimized PCR for the generation of HIA-MD targets

PCR was performed using MyTaq™ HS DNA reagents (Bioline Reagents Ltd, London, UK) and primer sequences described previously by Lang et al (35). 5 µL of cDNA was added to 10 µL of 5X MyTaq Reaction buffer, 1 µL of version 2 forward and reverse primers (20 µM each), 0.5 µL MyTaq HS DNA Polymerase, and 33.5 µL autoclaved H₂O, for a total reaction of 50 µL. PCR was performed on a GeneAmp PCR System 2700 thermal cycler (Applied Biosystems, Foster City, CA), under the following thermocycling conditions: 3 minutes at 95°C, followed by 50 cycles of 15 seconds at 95°C, 15 seconds at 58° C, and 5 seconds at 72°C, then finally, 2 minutes at 72° C. The PCR products were analyzed using Agilent 2100 DNA 1000 Series II kits and instrumentation (Agilent Technologies, Santa Clara, CA) to confirm amplification. All PCR products were

determined to be at a concentration of approximately 1×10^{11} copies/ $\mu\text{L} \pm 1$. Prior to HIA analysis, the PCR product was denatured at 95°C for 2 minutes and immediately placed on ice, in order to obtain single stranded product.

3.3.6 Microdevice fabrication

Each chip (4 cm x 4 cm x 1.5 mm) was made from two layers of a plastic substrate [Poly(methyl methacrylate), or PMMA] and features a 12-well circular array of 5-mm-diameter circular wells. The PMMA (Astra Products, Baldwin, NY) was cut using a VersaLASER system 3.50 (Universal Laser Systems, Scottsdale, AZ). The microwell features (designed in AutoCAD) were cut out of the top layer (1.0mm thick), which was then thermally bonded using established methods (36) to the bottom layer (0.5mm thick).

3.3.7 HIA instrumentation

The instrumentation used for HIA assays was developed in-house, and described in detail in **Chapter 2**. Briefly, the set-up consists of a vortexer (MS3 basic vortexer, IKA, Wilmington, NC) to hold the chip and provide gentle agitation, and a rotating magnet positioned above the chip to provide additional mixing of the probe-bound magnetic beads.

3.3.8 Bead preparation

Each set of probe-bound beads was prepared by immobilizing biotinylated probe oligonucleotides to Dynabeads MyOne Streptavidin C1 superparamagnetic beads

(Invitrogen, Oslo, Norway) under saturating conditions, according to the manufacturer's instructions. Following conjugation, the beads were brought up in 1X binding and washing buffer (5 mM Tris-HCl (pH 7.5), 0.5 mM EDTA, 1 M NaCl) in a volume equivalent to the initial volume of stock beads, to maintain the concentration of $7-10 \times 10^9$ beads per mL.

3.3.9 Hybridization buffers

The initial buffer (buffer 1) used was composed of 200mM KCl and 10mM Tris, at pH 7.5. Buffers 2, 3, and 4 were prepared by spiking formamide (Sigma, St. Louis, MO) into buffer 1 at 25% /v (buffer 2), 50% /v (buffer 3), and 75% /v (buffer 4). SSC buffers (3X, 1X, 0.5X, and 0.1X) were prepared from a 20X stock, composed of 3M NaCl and 0.3M sodium citrate, at pH 7.0.

3.3.10 HIA_{MD} assays

All assays were performed at room temperature. Each reaction took place in a 5mm (diameter) circular well, at a total volume of 20 μ L, composed of target sample (either PCR product, synthetic target sequences, or PCR buffer ["blank"]), hybridization buffer, and probe-bound beads, at the volumes specified. After loading the reagents, the chip was placed on the HIA set-up, using a rotating magnet speed of 2,000 rpm and a vortexing speed of 130 rpm, for a total of 2 minutes (unless otherwise stated). After the hybridization assay, a digital photo of each well on the chip was taken using a T1i DSLR camera with MP-E 65 mm f/2.8 1–5 \times macro lens (Canon U.S.A., Inc., Lake Success,

NY) and analyzed using a Kapur algorithm in the program Mathematica®, to derive a quantitative value (saturation) corresponding to the extent of aggregation in each well.

3.3.10.1 Initial feasibility assays

Reactions were composed of 17 μL of buffer 1, 1 μL of each 3'- and 5'- probe-bound beads, and 1 μL 1 μL synthetic target (10^{12} copies/ μL).

3.3.10.2 HIA_{MD} studies performed under pre-optimized conditions

Each reaction was composed of 18 μL buffer 1, 1 μL probe-bound beads (1:1 ratio of SP and DP-1 or DP-2), and 1 μL synthetic target (10^{12} copies/ μL).

3.3.10.3 Effect of ionic strength

Each reaction was composed of 18 μL SSC buffer (at the specified concentration), 1 μL probe-bound beads (1:1 ratio of SP and DP-1), and 1 μL synthetic target (10^{12} copies/ μL).

3.3.10.4 Optimization of buffer composition

Each reaction was composed of 18 μL hybridization buffer (as specified), 1 μL probe-bound beads (1:1 ratio of SP and DP-1 or DP-2), and 1 μL synthetic target (10^{12} copies/ μL).

3.3.10.5 Effect of target concentration

Each reaction was composed of 18 μL buffer 3, 1 μL probe-bound beads (1:1 ratio of SP and DP-2), and 1 μL synthetic target (at the concentration specified).

3.3.10.6 Reaction composition modifications

Each reaction was composed of 9 μL hybridization buffer (as specified), 1 μL probe-bound beads (1:1 ratio of SP and DP-2), and 10 μL synthetic target (10^{11} copies/ μL).

3.3.10.7 Final optimized HIA_{MD} reaction

Each reaction was composed of 10 μ L target sample (either PCR product or synthetic target sequence at a concentration of 10^{11} copies/ μ L, corresponding to ~ 50 ng of input DNA), 9 μ L buffer 4, and 1 μ L probe-bound beads (1:1 ratio of SP and DP-2).

3.4 Results and Discussion

3.4.1 Establishing initial feasibility

Previously, the feasibility of applying the HIA method for single base mismatch detection was demonstrated in short, 26-base synthetic oligonucleotides (32). While this was a promising piece of preliminary data, it was not sufficient to establish whether HIA would be viable for point mutation detection in biological samples, using PCR-generated target sequences. Of note, PCR is used to generate the target sequence in the majority mutation analysis techniques (37), and it is advantageous for a number of reasons. First, amplification of target DNA facilitates more sensitive detection (data to follow), since a higher concentration of the target strand enhances the hybridization efficiency. Second, PCR cuts down genomic DNA or mRNA to generate a shorter DNA segment around the mutation locus. Keeping the target short is important for minimizing possible secondary structure, which can lead to inhibited probe-target hybridization and diminished sensitivity of the assay (38), as well as minimizing possible regions where the probes can

bind non-specifically. Due to the restraints of primer design, the PCR-generated target sequence must be at least 50 base pairs (bp), considering that optimal PCR primers are 18-24 bases in length (39), and that the primer regions must exclude the mutation locus so that it is conserved during amplification. This means that the target generated would, at minimum, be roughly twice the length of the target sequence used in previous studies. Given the significance of target length to discrimination capabilities, it was important to first establish the feasibility of revealing a single base mismatch in a 50-base synthetic target using a HIA approach.

First, a HIA assay was established to detect a 50-base target perfectly complimentary to the probe sequences. The aggregation was analyzed in terms of % saturation, calculated from the ratio of the image saturation value given by the target to that of a blank (no DNA) sample. Therefore, a blank sample corresponds to 100% saturation while lower % saturation values indicate a greater extent of aggregation, and thus, more efficient hybridization (refer to **Fig. 3-2**). As shown in **Figure 3-3**, the target was detectable down to 10^8 copies per μL .

To determine the optimal location of the mismatch for maximum destabilization of the hybridization complex, 50-base target sequences that differed only in the location of the mismatch(s)

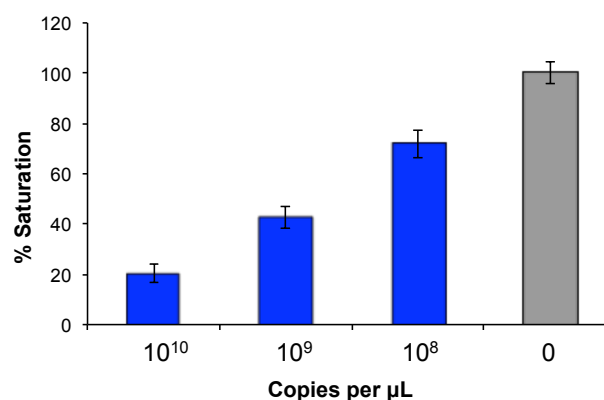


Figure 3-3. Detection of a 50-base target sequence with HIA. A synthetic 50-base oligonucleotide was tested to confirm the capability of the HIA system to detect a target sequence roughly the length of a PCR product. 25 minute assays.

relative to the probes were tested. In the event that a single mismatch might not provide enough destabilization of the hybridization complex to be detected by HIA, targets with two mismatches were also considered. As shown in **Figure 3-4**, it was determined that a target with one mismatch could be differentiated from a completely complementary sequence (via % saturation). Selectivity was characterized quantitatively through a discrimination ratio, or the ratio of the aggregation (in terms of saturation) induced by the mutant target to that by the wild-type target. A discrimination ratio greater than 1 indicates decreased aggregation (higher saturation) induced by the mutant target as compared to the wild-type, with higher discrimination ratios indicative of a greater selectivity. Maximum discrimination and, therefore, the highest selectivity for revealing point mutations, occurred when the mismatch was positioned 5 bases from the end of the probe (**Fig. 3-4**). These results are consistent with the theory that centrally-placed

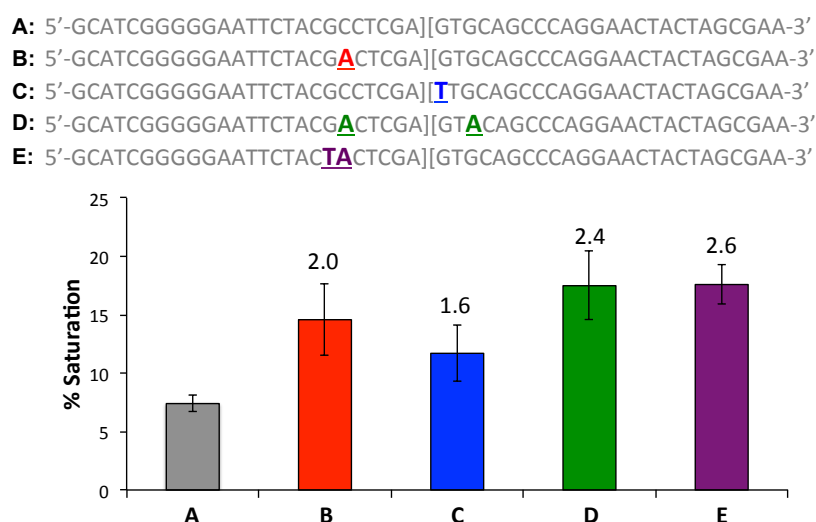


Figure 3-4. Detection of mismatch(s) in a 50-base target sequence. 50-base target sequences with one or two base mismatches were tested in 5-minute HIA assays to determine the location of a mismatch that provided maximum destabilization of the hybridization complex (i.e., highest resulting discrimination ratio). Discrimination ratios are reported above each data point.

mismatches have a higher destabilizing effect on the duplex, and are therefore easier to be discriminated (40). The mismatch could not be internalized within the probe-target complex more than 5 bases from the target center, considering that the location of the mismatch must not overlap with the primer region during amplification.

A synthetic single-stranded DNA sequence mimicking a 58-bp *KRAS* PCR product (see section 3.4.2) was used to test the feasibility of the HIA method as a *KRAS*-specific genotyping technique. Synthetic targets with and without a point mutation were used. Optimal probes were designed based on the information obtained from the previous study, with the location of a commonly occurring mutation (c.35G>A) positioned internally, 5 bases from the end of the probe binding region. Optimization of the hybridization reaction time was performed to establish maximum selectivity of the assay, such that the system was capable of differentiating a sample containing only mutant target sequences (i.e., target sequences containing a mismatch) from a sample containing a 50/50 mixture of mutant and wild-type (i.e., perfectly-matched) target sequences. The discrimination ratios of both “homozygous” mutant (100% mutant) and “heterozygous” mutant (50% mutant; 50% wild-type) sample compositions, based on % saturation, were plotted as a function of assay time (Fig. 3-5).

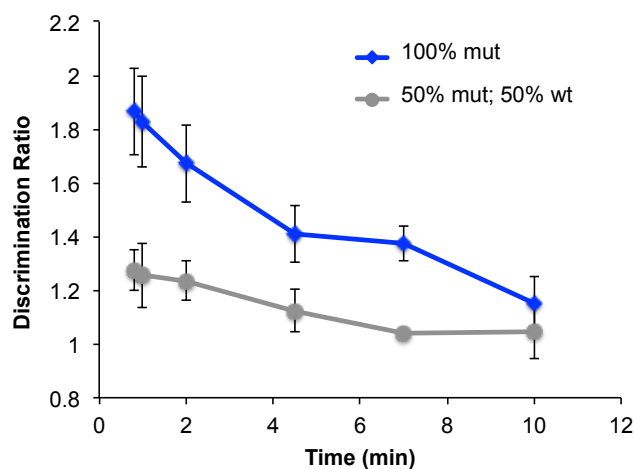


Figure 3-5. Optimization of the hybridization reaction time. Discrimination ratios for homozygous mutant (100% mutant) and heterozygous mutant (50% mutant; 50% wild-type) samples were plotted as a function of reaction time. Discrimination is shown to decrease with time.

Discrimination ratios were greatest at shorter assay durations, and decreased with the time of the assay. Based on these results, future HIA_{MD} assays were kept below two minutes.

As proof of initial feasibility, in a one-minute assay, the HIA system demonstrated the capability of reproducibly distinguishing synthetic samples modeling heterozygous, homozygous mutant, and wild-type genotypes (**Fig. 3-6**). Although the discrimination between wild-type and mutant samples was subtle, the correct trend (decreased aggregation for mismatched targets) was observed.

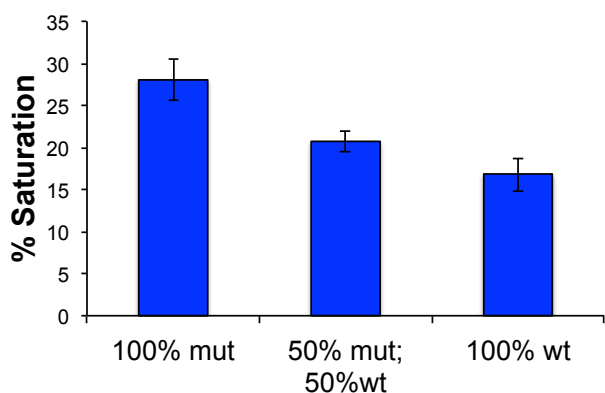


Figure 3-6. Demonstrating initial feasibility of the HIA_{MD} method. Synthetic oligonucleotide targets mimicking the *KRAS* RT-PCR product (58 bp) were used to model homozygous mutant (100% mutant), heterozygous (50% mutant; 50% wild-type), and wild-type (100% wild-type) samples. The expected trend is observed, where aggregation is decreased in mismatched (“mutant”) targets.

3.4.2 Generating the target sequence from biological samples

PCR primers were designed to generate a *KRAS* target sequence from biological samples. The principle design requirement was that the binding locations of the primers on the target strand would frame the mutation locus without overlapping it, such that the identity of the bases at the mutation locus (codons 12 and 13) would be conserved during amplification. With that requirement met, PCR primers were chosen that produced the

shortest possible product. The 58-bp amplicon segment generated using these primers (**Table 3-1**, version 1 primers) was used to model the synthetic target strand first used in initial feasibility studies (**Fig. 3-5** and **Fig. 3-6**).

Using these primers, a PCR reaction was established to generate a target sequence from a human genomic DNA (hgDNA) sample. The amplified sample, as well as a non-template (i.e., negative) control, was detected using commercial microchip electrophoresis (Agilent Bioanalyzer). The results show a short amplicon, sized as ~69 bp by the Bioanalyzer, in both the hgDNA sample and the negative control (**Fig. 3-7A** and **Fig. 3-7B**, respectively). Typically, these results would be indicative of DNA contamination in the negative control; however, a series of troubleshooting studies led to the conclusion that the amplicon observed in the negative control was likely a primer complex. Melting curve analysis (**Fig. 3-8**) serves as a strong piece of supporting evidence, as it clearly distinguishes the amplification product of the hgDNA sample from the negative control based on the melting temperatures (T_m).

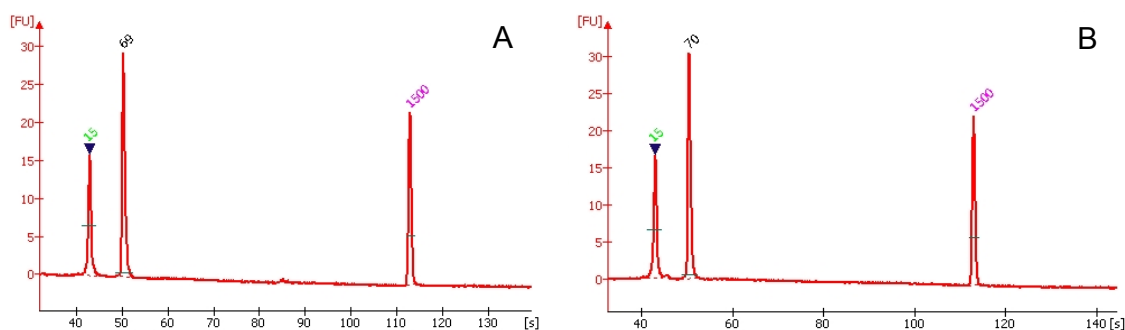


Figure 3-7. PCR with version 1 primers to generate a 58 bp KRAS target for HIA_{MD} analysis. Amplification products from hgDNA (A) and a non-template control (B) were detected with the Agilent Bioanalyzer and sized as 69 bp and 70 bp, respectively. 15 bp and 1500 bp markers are included in each sample for proper sizing of the product. The amplicon size is labeled above the respective peak.

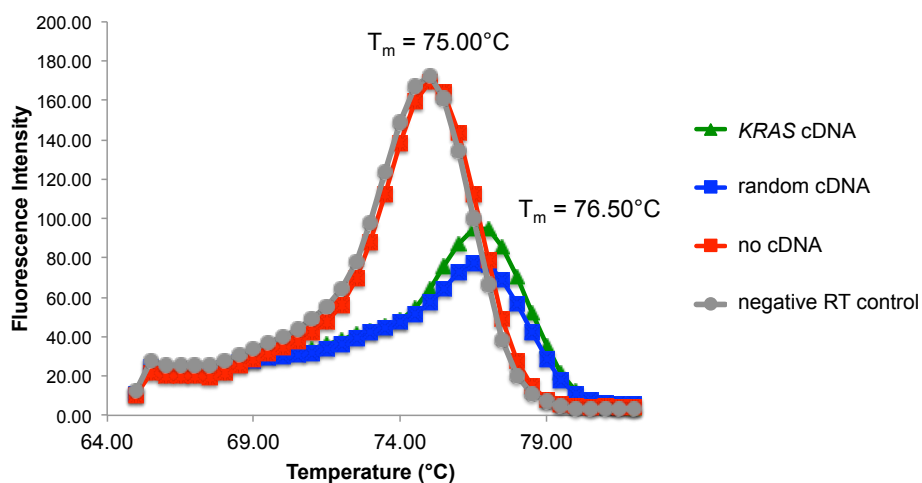


Figure 3-8. Melting curve analysis of PCR product with version 1 primers. Following real-time PCR, melting curves were generated. The positive samples (amplified from KRAS-specific cDNA and random cDNA) show melting temperatures at 76.50°C, while the negative controls (no cDNA and negative reverse transcription control) show melting temperatures at 75.50°C.

Although slightly outside of the range of $\pm 10\%$ CV sizing accuracy associated with the Bioanalyzer (as reported by the manufacturer), the 69 bp amplicon detected by the Bioanalyzer was likely the intended 58 bp PCR product. To confirm the identity of the amplicon, sequencing would be ideal. However, sequencing methods typically require that the product is greater than 100 bp in length. Instead, the 58 bp HIA target (plus strand of the PCR product) was synthesized as a single-stranded oligonucleotide and used as the template DNA for PCR. The product was detected using the Bioanalyzer, along with the synthetic target (not amplified) at 10^{12} copies per μL . As expected, the results (**Fig. 3-9**) showed ~69 bp peaks for both samples, serving as strong evidence supporting the fidelity of the PCR amplicon in the positive control (**Fig. 3-7A**).

Quantitative PCR (qPCR) was performed to quantify the concentration of first-strand cDNA obtained after reverse transcription from the RNA lysate of human-derived

cell lines. The qPCR results (**Fig. 3-10**) revealed that the concentration of first-strand cDNA obtained from the RNA lysate was less than 10^6 copies per μL . This is below the concentration of target shown to be detectable in initial HIA assays (**Fig. 3-3**); thus, this result confirmed the necessity of PCR prior to HIA analysis.

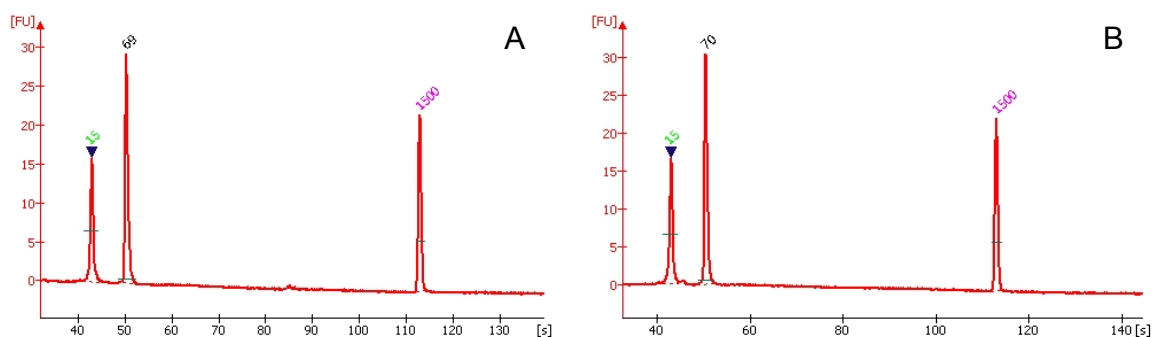


Figure 3-9. Investigating the sequence fidelity of PCR product generated with version 1 primers. A) A synthetic KRAS template was used as the input for a PCR reaction. The product was analyzed on the Bioanalyzer and shows a ~69 bp amplicon. B) The synthetic template at 10^{12} copies/ μL (not amplified) was run on the Bioanalyzer and appears as a ~67 bp product. 15 bp and 1500 bp markers are included in each sample for proper sizing of the product. The amplicon size is labeled above the respective peak.

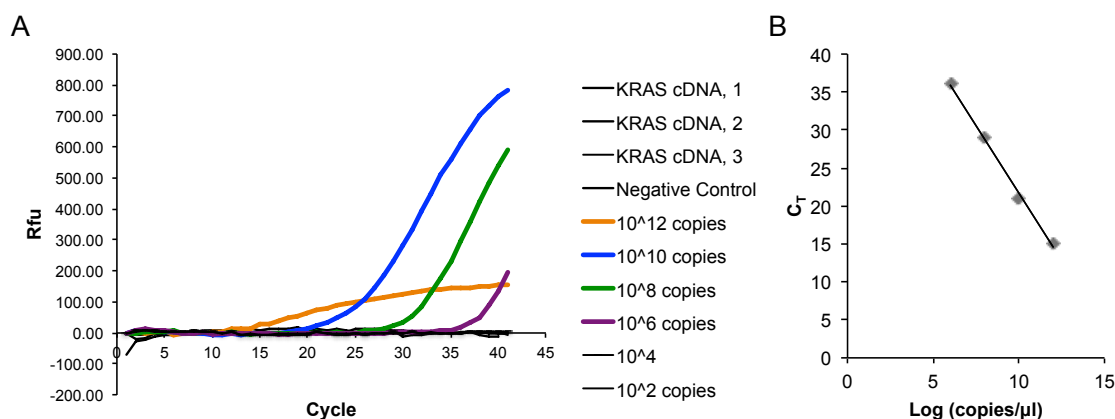


Figure 3-10. Quantitative PCR to determine concentration of first-strand KRAS cDNA. A) Real-time PCR curve showing amplification of KRAS cDNA (in triplicate), as well as synthetic single-stranded template at 10^{12} copies/ μL , 10^{10} copies/ μL , 10^8 copies/ μL , 10^6 copies/ μL , 10^4 copies/ μL , 10^2 copies/ μL , and a non-template control (negative control). B) Standard curve generated from qPCR. Synthetic template less than 10^6 copies/ μL was not detectable. KRAS cDNA was not detectable; thus, the concentration must be less than 10^6 copies/ μL .

It was determined by real-time PCR that, by reducing the number of amplification cycles to ~30 cycles, formation of the primer complex in the non-template control could be avoided (**Fig. 3-11**); however, this was not ideal, as it reduced the yield of the PCR product in the positive samples significantly. Ultimately, it was determined that these primers were not a good choice, and added length in the product would have to be compromised for more reliable primers. Primer sequences taken from the literature (35) (**Table 3-1**, version 2 primers) were used to produce a 95 bp amplicon. Analysis of the product with the Bioanalyzer (**Fig. 3-12**) as well as real-time PCR analysis (**Fig. 3-13**) confirmed successful amplification from the RNA lysates of six human-derived cancer cell lines.

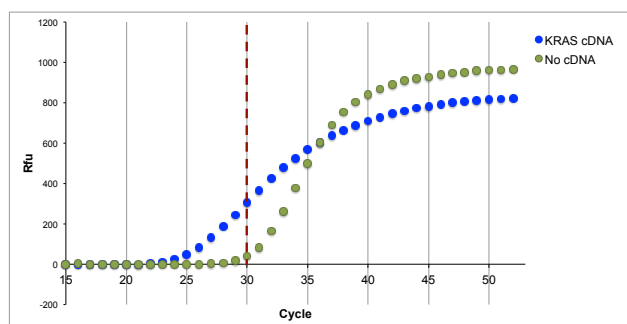


Figure 3-11. Real-time PCR with version 1 primers. Curves show that amplification in the negative control begins around cycle 30. However, the yield of product in the positive sample is low at cycle 30.

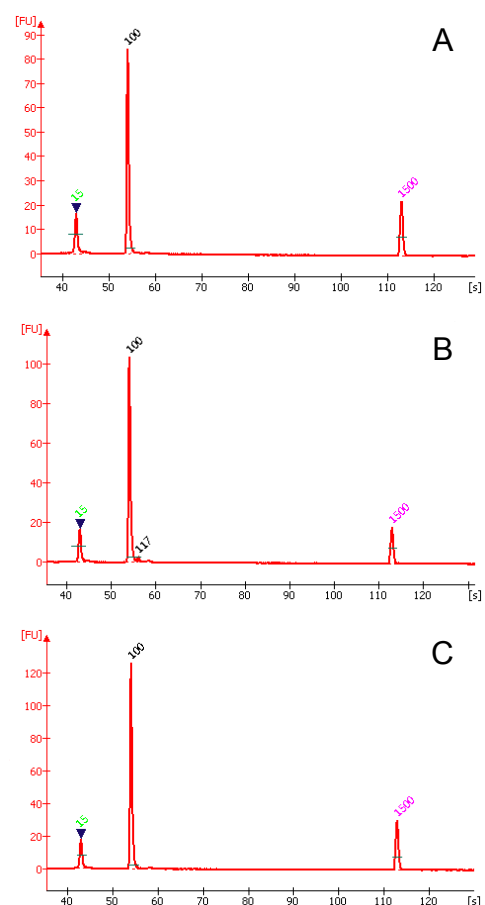


Figure 3-12. PCR with version 2 primers to generate a 95 bp KRAS target. Amplification products from cell lines were analyzed using the Agilent Bioanalyzer. (A) SW-620, (B) H522, and (C) H1975. All 3 samples show amplification of a ~100 bp product. 15 bp and 1500 bp markers are included in each sample for proper sizing of the product. The amplicon size is labeled above the respective peak.

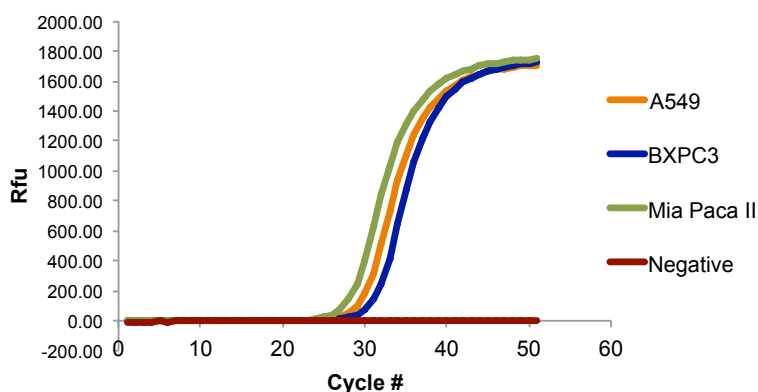


Figure 3-13. Real-time PCR with version 2 primers. *cDNA prepared from 3 cancer cell lines shows expected amplification behavior, while no amplification is observed in the non-template control.*

3.4.3 Probe design

Probe sequences were strategically designed for the new *KRAS* target. As shown in **Figure 3-14**, the HIA_{MD} assay involves a pair of probes, including a “stabilizing probe” and a discriminating probe.” The basis for mutation detection is provided by the discriminating probe (DP), which is designed such that its binding region on the target sequence includes the *KRAS* mutation region (codons 12 and 13). The DP is complementary to wild-type *KRAS*, such that the presence of a mutation in the target sequence results in a hybridization complex that is thermodynamically less favorable when compared to a wild-type (perfectly matched) target sequence. This can then be exploited for detection via a decrease in the extent of bead aggregation induced by hybridization. The HIA_{MD} approach is unique in that a positive analytical signal (aggregation) indicates the absence of a mutation, as opposed to characteristic assays that look for the presence of a mutation using probes that are complementary to the mutant

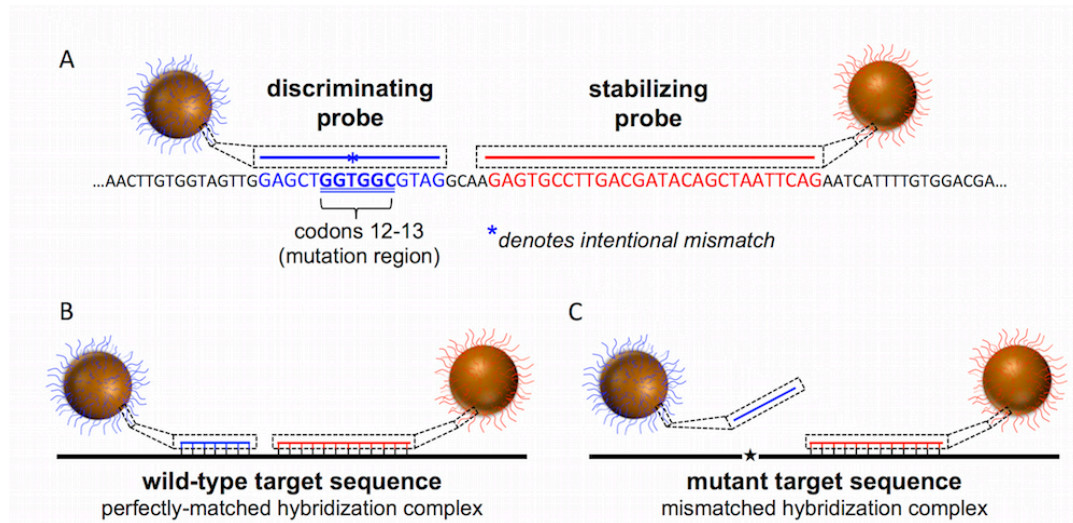


Figure 3-14. Probe Design. The stabilizing probe (red) is designed to hybridize to the target sequence regardless of its *KRAS* mutation status. The discriminating probe (blue) is designed such that it preferentially binds to the wild-type target (B). Hybridization of the discriminating probe to a mutant target is less thermodynamically favorable (C).

sequence. The advantage of this method is that any of the common *KRAS* mutations can, theoretically, be detected in a single assay using a single set of probes. This contrasts other hybridization-based mutation detection assays, as well as allele-specific PCR methods, which require separate probes and/or primers, and often separate assays with varying operating conditions to be performed for every mutation investigated (35, 41, 42). Notably, clinical decisions are simply made on the basis of whether or not a *KRAS* mutation is present, and therefore, knowledge of the particular *KRAS* mutation is not clinically necessary or even currently relevant (18).

In order to maximize the destabilizing effect (in terms of thermodynamic cost) resulting from a single base mismatch in the hybridization complex, the DP was kept short, at 15 bases, which includes codons 12 and 13, as well as 4- and 5- base regions on either side. The mutation region was positioned near the center of the DP binding region,

since it has been shown that a centrally located mismatch produces a hybridization complex with highest degree of instability (43). A second version of the DP was also designed, which incorporated an intentional mismatch at the position corresponding to *KRAS* c.36T, with the purpose of providing increased destabilization in a hybridization complex formed with a mutant target sequence. The c.36T position was chosen to bear the intentional mismatch on the basis that there are no reported missense mutations at that position, (44) and therefore, there is currently no clinical necessity of detecting a mutation there. We refer to this probe as DP-2, while the discriminating probe without an intentional mismatch is referred to as DP-1.

The stabilizing probe (SP) was designed to form a strong hybridization complex with the target sequence (evaluated in terms of T_m) relative to that of the discriminating probe, such that its hybridization to the target sequence is favorable, even under the stringent conditions ultimately required to achieve discrimination. The binding regions of the two probes on the target sequence were separated by a small “spacer” region of 4 bases, which was found to increase the sensitivity of the assay, probably as a result of more favorable binding sterics.

Initial studies were performed with synthetic target sequences mimicking the *KRAS* gene segment, identical in sequence to the PCR-generated segment from which targets from biological samples were prepared. In these studies, both DP-1 and DP-2 were tested in parallel. In these initial studies, aggregation in the presence of both the wild-type and mutant (c.34G>T) sequences was observed, with only slight discrimination between % saturation values (**Fig. 3-15**). A discrimination ratio of only 1.29 was

observed, with a marginal improvement (discrimination ratio of 1.41) when DP-2 was used. To improve the selectivity of the assay, and therefore allow for a more robust discrimination, optimization of the hybridization conditions was required.

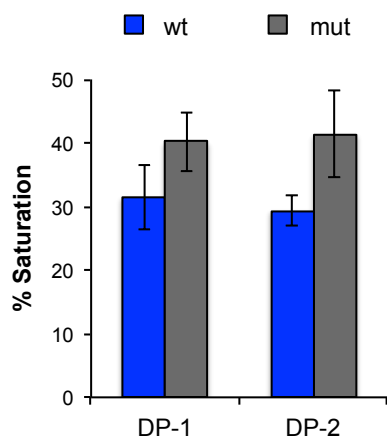


Figure 3-15. HIA_{MD} studies performed under pre-optimized conditions. Assays were performed using both discriminating probes, without and with an intentional mismatch (DP-1 and DP-2, respectively). Each assay was performed on a chip with synthetic wild-type (wt), synthetic mutant (mut), and blank (no DNA) samples, each in triplicate. Results are reported as % saturation, calculated from the ratio of the saturation value given by the target, to the average saturation value of a blank sample (set as 100% saturation). Lower % saturation values correspond to a greater degree of bead aggregation.

3.4.4 Augmenting the instrumentation to provide temperature control

High temperature is commonly used to achieve hybridization selectivity. To allow temperature-controlled HIA_{MD} reactions, it was required that instrumentation be augmented with a thermostatic device. Initially, a Peltier device was positioned below the device to heat the microwells. In initial characterization of the Peltier, a gradient effect was observed, producing inhomogeneous temperature across the microdevice (**Fig. 3-16**). This effect, in addition to the slow heating rate of the Peltier, was not well suited for this application.

In a second attempt to provide temperature control, the instrumentation was augmented with a PID-controlled resistive heater, fabricated using nichrome wire and

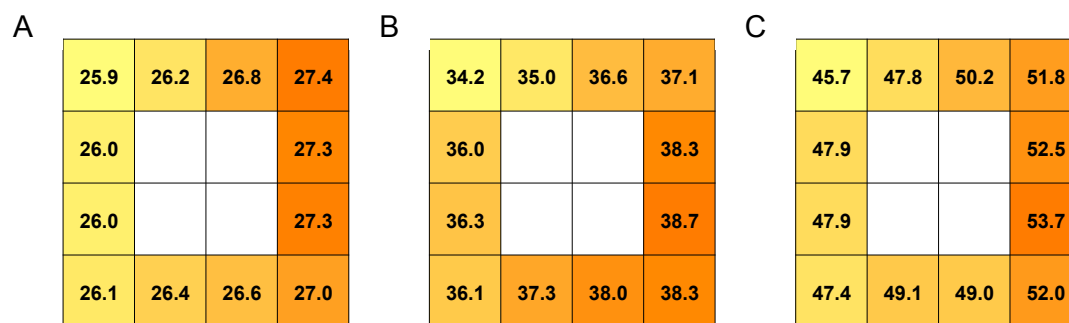


Figure 3-16. Characterization of temperature homogeneity using a Peltier device. A PMMA microdevice was fabricated with a 4 x 4 grid of microwells (5mm diameter). The outer microwells were filled with buffer and heated by placing the device above a Peltier device. 3 studies were performed, each with a different target temperature [A) ~27°C; B) ~35°C; C) ~50°C]. The temperature of the buffer in each well was measured in duplicate using a thermocouple placed in the well. Each temperature (in °C) displayed in the figure above represents the average of duplicate measurements. The spread of temperature across the chip increases with increasing target temperature. [A) Δ temperature = 1.5°C; B) Δ temperature = 4.1°C; C) Δ temperature = 8.0°C]

polyimide tape. An aluminum block was placed on top of the resistive heater and sealed to the heater using thermal paste for efficient heat transfer. The heater demonstrated a fast heating rate and homogenous heating distribution. However, the ability to maintain a steady temperature during HIA_{MD} assays was particularly challenging due to the cooling effect of the rotating magnet above the microwell device. A strategy was devised where an “overshooting temperature” was reached prior to the start of the reaction, such that the temperature would be cooled to the target temperature due to the effects of the RMF (see **Fig. 3-17A**). By systematically adjusting the parameters of a custom Labview program connected to the heater (see **Table 3-4**), a constant temperature (± 1 degree variation) could be achieved during the HIA assay (see **Fig. 3-17B and C**). While this heating system was effective, the PIDs and other program parameters needed to be re-optimized for every target temperature. The tedious nature of this process was contradictory to the

fundamental aim of maximizing the simplicity of our instrumentation and the assay itself.

Thus, the ongoing use of this or other strategies to control hybridization temperature was deliberately avoided. As an added benefit, developing this assay to perform at a single temperature (room temperature) maintained the potential of using this method to analyze multiple targets simultaneously, on a single chip. This is difficult to accomplish with other platforms where target-specific temperature control is required for analysis.

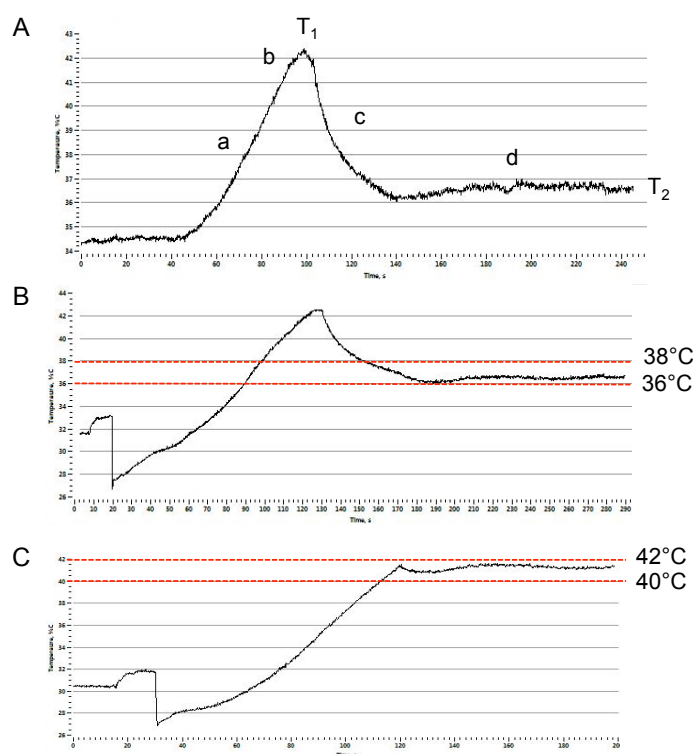


Figure 3-17. Optimization of temperature-controlled HIA reactions using a PID-controlled resistive heater. A) Exemplary temperature profile. A microwell filled with buffer is heated to an “overshooting temperature, T_1 ” (a). When temperature equals T_1 minus 1, probe-bound beads and target DNA are added to the microwell. At T_1 , the assay begins and the microwell device is placed under the RMF. Upon exposure to the RMF, the reaction is cooled (c) to reach a steady target temperature (d), T_2 . B) and C) The strategy illustrated in (A) is executed, providing steady (± 1 degree variation) temperature-controlled HIA reactions.

Program parameter	Description
T_1	Overshooting temperature
t_1	Holding time at T_1
T_2	Assay temperature (target temperature)
t_2	Holding time at T_2
P_1	Proportional value (T_1)
D_1	Derivative value (T_1)
I_1	Integral value (T_1)
P_2	Proportional value (T_2)
D_2	Derivative value (T_2)
I_2	Integral value (T_2)
1_start	Degrees away from T_1 that t_1 starts
1_PID	Degrees away from T_1 that the PIDs kick in
2_start	Degrees away from T_2 that t_2 starts
2_PID	Degrees away from T_2 that the PIDs kick in

Table 3-3. Optimization parameters for Labview program.

3.4.5 Buffer composition

Without temperature elevation, hybridization stringency was achieved with the buffer composition by reducing the ionic strength and adding formamide. First, the effect of varying the ionic strength of the hybridization buffer was explored. As shown in **Figure 3-18A**, decreasing the ionic strength resulted in consistent decreases in the extent of aggregation induced by both the wild-type and mutant samples, as indicated by

increasing image saturation values. Therefore, the discrimination ratio varied only slightly (**Fig. 3-18B**).

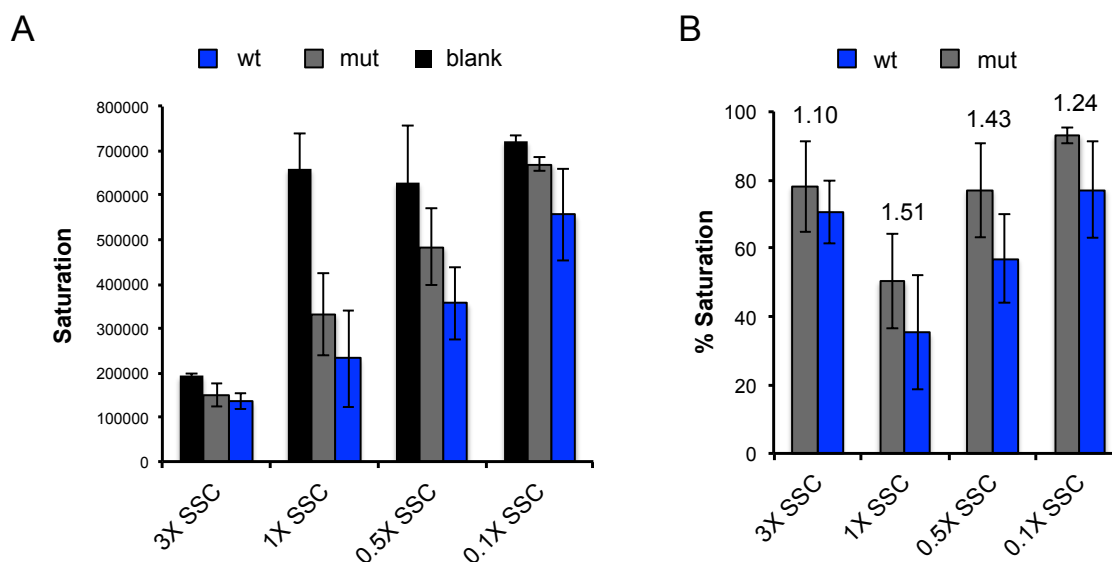


Figure 3-18. Effect of ionic strength. Hybridization buffers of decreasing ionic strength (3X SSC – 0.1X SSC) were tested in HIA-MD assays. Each assay was performed on a chip with synthetic wild-type (wt), synthetic mutant (mut), and blank (no DNA) samples, each in triplicate. The results are given in terms of raw saturation values (A) and % saturation (B). Discrimination ratios are reported above each data set in (B). Lower saturation corresponds to a greater extent of aggregation.

To provide further stringency, the use of formamide (a common chemical denaturant) was explored. A series of buffers were prepared (**Table 3-5**), where formamide was spiked in to the initial hybridization buffer (“buffer 1”, 200 mM KCl) at 25% /v (“buffer 2”), 50% /v (“buffer 3”), and 75% /v (“buffer 4”), corresponding to 22.5%, 45%, and 67.5% overall formamide content in the reaction, respectively. By preparing the buffers in this manner, a reduction in salt content was accompanied by the increase in formamide content. Therefore, the increase in stringency from buffers 1-4 can be attributed to the combination of increased levels of formamide as well as a reduction

Table 3-4. Buffer composition.

	% Formamide	[Salt] (mM KCl)
Buffer 1*	0	200
Buffer 2	25	150
Buffer 3	50	100
Buffer 4	75	50

*Buffer 1 was established as the optimal hybridization buffer in previous work.

in the stabilizing effect of increased ionic strength.

Each buffer was tested in a series of HIA_{MD} reactions, first using DP-1 (**Fig. 3-19**). The increase in stringency provided by buffer 2 and buffer 3 was inconsequential, as signified

by % saturation values that were relatively unchanged from initial assays using buffer 1 (non-stringent conditions). When buffer 4 was used, however, neither the wild-type nor the mutant targets were able to induce aggregation, as indicated by % saturation values

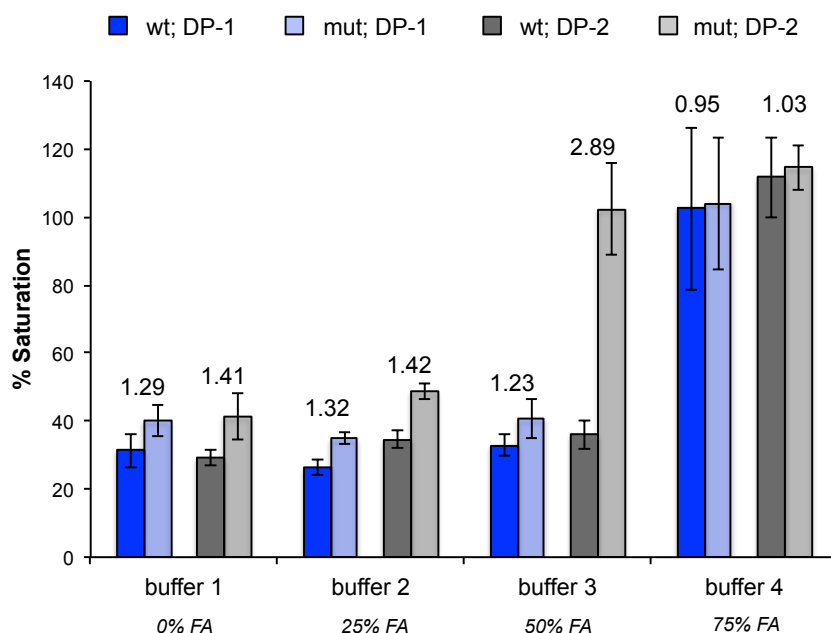


Figure 3-19. Optimization of buffer composition. Buffers 1-4 were tested in assays using both discriminating probes, without and with an intentional mismatch (DP-1 and DP-2, respectively). Each assay was performed on 3 chips, each with reactions containing wild-type (wt), mutant (mut), and blank (no DNA) samples. Each 20 μ L reaction contained 1 μ L of target (10^{12} copies/ μ L) or PCR buffer (blank). Discrimination values are reported above each data set. Lower % saturation values correspond to a greater degree of bead aggregation.

near 100%. As previously described (and illustrated in **Fig. 3-2**), 100% saturation corresponds to a completely blank (no aggregation) sample.

Buffers 1-4 were tested again using DP-2, where additional stringency was provided by the intentional mismatch in the discriminating probe sequence. The effects of buffers 2 and 4 were similar to those observed using DP-1, where buffer 2 had an insignificant effect, and buffer 4 prevented any detectable aggregation. However, when buffer 3 was used, a substantial increase in the discrimination power was observed. Under these conditions, the wild-type target produced significant aggregation while the mutant target remained completely dispersed; by definition, this indicates that hybridization is selective. Since the % saturation values from the wild-type sequence were roughly the same as those observed under non-stringent conditions (buffer 1), with the mutant sequence displaying ~100% saturation (indicative of no aggregation), further optimization of the buffer conditions was deemed unnecessary.

Notably, the reduction of ionic strength (**Fig. 3-18**) and the use of a discriminating probe with an intentional mismatch (**Fig. 3-15**) alone were insufficient to provide a significant increase in discrimination power. However, these parameters together, in combination with the presence of formamide at an optimal concentration increased the discrimination power of the assay roughly three-fold, and allowed a truly selective response.

3.4.6 Initial attempts with biological samples and subsequent adjustments

DNA targets generated from three cancer cell lines were analyzed with the HIA_{MD} assay under the conditions determined to facilitate high discrimination between synthetic wild-type and mutant target sequences. However, as shown in **Figure 3-20**, the results showed

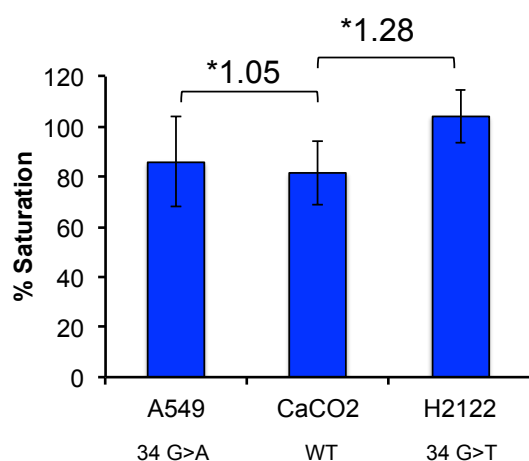


Figure 3-20. Initial attempts with biological samples. PCR products from 3 cancer cell lines, A549 (KRAS c. 34G>A), CaCo2 (KRAS wild-type), and H2122 (KRAS c.34G>T) were tested with HIA_{MD} under the conditions determined to be optimal with synthetic samples. Resulting discrimination ratios between the mutant cell lines and the wild-type cell line were insufficient for mutation discrimination. *denotes discrimination ratio.

insufficient discrimination between the wild-type and mutant cell lines. Since all reaction conditions were the same as the optimized conditions, differences in the samples themselves (synthetic sample versus the PCR-derived target sequences) were considered. The most obvious difference between the samples was the background environment, namely, the buffer. Synthetic targets were suspended in buffer 1, while the PCR products were in the MyTaq PCR buffer (Bioline). To test the effect of the background buffer, synthetic oligonucleotide targets were prepared in 1X MyTaq buffer, while keeping all other parameters constant. As shown in **Figure 3-21A**, a high discrimination ratio as seen in previous studies was maintained. Thus, the buffer composition of the PCR sample was likely not the issue.

Another important difference was the concentration of the synthetic target as compared to the concentration generated from PCR. The concentration of target generated in the PCR reaction was reliably $1 (\pm 1) \times 10^{11}$ copies per μL (as determined by the Agilent Bioanalyzer, **Fig. 3-12**), yet all optimization studies had been performed using synthetic targets at 1×10^{12} copies per μL . Indeed, when the synthetic target sequence was tested at 1×10^{11} copies per μL , the resulting discrimination ratio was considerably lowered (**Fig. 3-21B**).

In a further investigation on the effect of target concentration on aggregation, it was

revealed that 1×10^{12} copies in the microwell

(total volume: $20 \mu\text{L}$) was required, below which insufficient aggregation was induced by the wild-type sequence to provide a statistically significant distinction from aggregation induced by the mutant sequence (**Fig. 3-22**). In order to meet this requirement without having to concentrate the PCR product(s) (increasing time, effort, and adding resources), the reaction was modified so that addition of $10 \mu\text{L}$ of PCR product would provide 10^{12} copies of the target. This increase in the volume of the target sequence in the overall

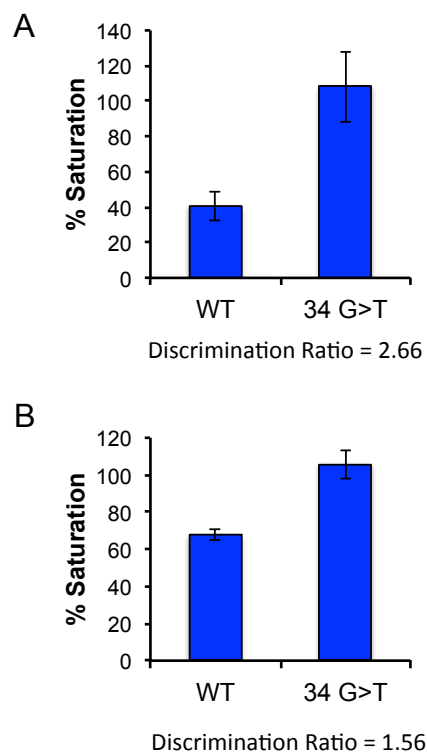


Figure 3-21. Assay troubleshooting. A) Synthetic targets were prepared in 1X MyTaq Buffer and analyzed with HIAMD. The resulting discrimination was high (2.66), in line with previous optimization studies. B) Synthetic targets were prepared at 10^{11} copies per μL and analyzed with HIAMD. The resulting discrimination ratio was lowered to 1.56, indicating the importance of target concentration in obtaining sufficient discrimination.

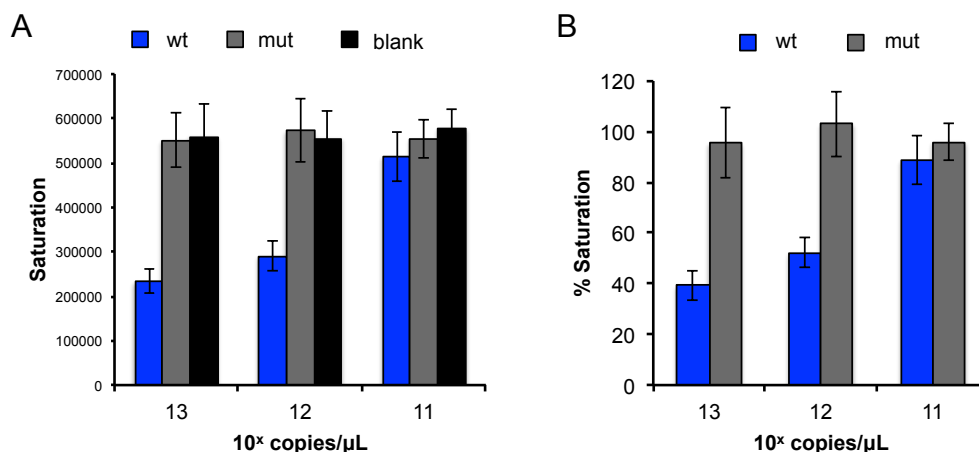


Figure 3-22. Effect of target concentration. *HIA_{MD}* assays were performed with targets present in decreasing quantities. 1 μL of target (wt, mut, or blank) at the displayed concentration was added to each reaction (20 μL total volume). Each assay was performed four times on chips with wild-type (wt), mutant (mut), and blank (no DNA) samples. Lower (%) saturation values correspond to a greater degree of bead aggregation.

reaction (from 5% to 50% by volume) required a proportional decrease in the volume of the hybridization buffer (from 90% to 45% by volume). [Note: the bead-bound probes were maintained at 5% by volume in the assay]. In order to keep the formamide content consistent with the previously optimized reaction (45% formamide in the well), the hybridization buffer would have to be composed of pure formamide, without additional salt or buffering agents. This was detrimental for the discriminatory capability of the assay, as it significantly reduced the extent of bead aggregation induced by the wild-type target (**Fig. 3-23A**). However, it was determined that with the use of buffer 4 in the modified assay, high discrimination between wild-type and mutant sequences could be achieved (**Fig. 3-23B**). Once again, the % saturation values generated by the wild-type sequence were in line with the results from the non-stringent assay, while the mutant

sample gave results near 100% saturation, implying that further optimization of the buffer composition would be unnecessary.

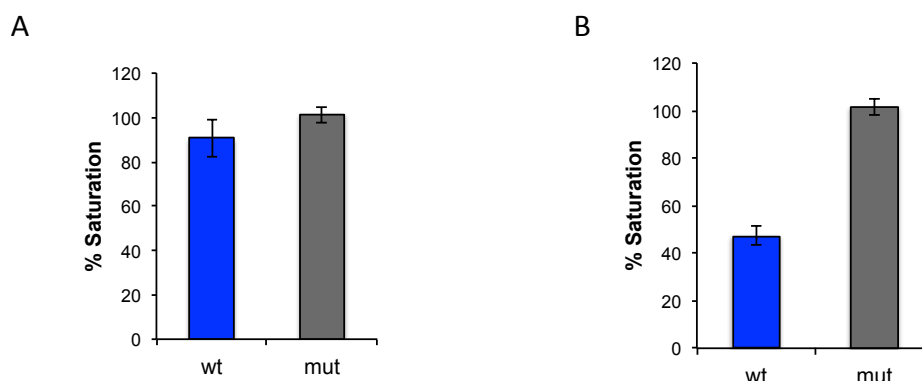


Figure 3-23. Reaction composition modifications. Different hybridization buffers were tested using the modified reaction composition, comprised of 10 μ L target sample, 9 μ L hybridization buffer, and 1 μ L bead-probe solution. A) Pure (100%) formamide was detrimental to the discriminatory capability of the assay (discrimination ratio = 1.11). B) Buffer 4 (75% formamide) allowed high discrimination (discrimination ratio = 2.15) to be achieved. Each assay was performed on a chip with synthetic wild-type (wt), synthetic mutant (mut), and blank (no DNA) samples, each in triplicate. The concentration of target sequence added to each reaction (total volume 20 μ L) was 10^{11} copies/ μ L. Lower % saturation values correspond to a greater degree of bead aggregation.

By modifying the reaction composition, increasing the volume contribution of the target in order to meet the mass requirement, and making appropriate modifications to the buffer composition, the HIA_{MD} assay was able to perform mutation analysis of real biological samples immediately following PCR. These modifications circumvent the need for additional sample preparation, including post-amplification concentration adjustments, and/or buffer exchange. The extreme simplicity of our pre-analytical process is a distinguishing feature of our assay and offers a key advantage over other platforms.

3.4.7 *KRAS* mutation analysis of cancer cell lines

Following the initial development and optimization of the assay, we evaluated the ability of our method to analyze the *KRAS* mutation status in a panel of eight human-derived cancer cell lines (**Table 3-2**). Colorectal and lung cancer cell lines were tested in addition to pancreatic cancer cell lines, since these cancers show the highest incidences of *KRAS* mutation. For each class of cancer (i.e., colorectal, lung, and pancreatic), both wild-type *KRAS* and *KRAS* mutant cell lines were tested.

After PCR, the samples were thermally denatured and snap-cooled, in order to obtain single-stranded targets for use in the HIA assay. Notably, this brief snap cool was the only additional step required following PCR. This is a unique asset of this platform, as other methods generally require a form of sample clean up to remove PCR artifacts prior to analysis. Additionally, it is common for other methods to use a more complex method to obtain single-stranded product for hybridization-based analysis, since the presence of the complementary PCR strand is in competition with the hybridization probe for target binding; this can significantly limit the sensitivity of the assay.

Each assay was performed on a multi-well PMMA chip loaded with the following, each in duplicate: i) PCR product of the cell line in question, ii) a wild-type positive control (1×10^{11} copies per μL), iii) a synthetic mutant control (c.34G>T; 1×10^{11} copies per μL), and iv) a blank (PCR buffer containing no DNA). The saturation values obtained after image analysis for each sample type were averaged. The extent of aggregation from each cell line was normalized (as a percentage) to the aggregation from the synthetic wild-type sequence (which, theoretically would give maximum aggregation

at the given concentration). The aggregation measured in a blank sample (the background) was subtracted from this normalized value to yield the final % aggregation value (see **Eq. 1**). The analysis of each cell line was performed on three separate chips to establish reproducibility. Each assay was complete in less than 10 minutes following PCR, which included ~3 minutes to denature and snap-cool the product, ~1 minute to pipette the samples and reagents (hybridization buffer and probe-bound beads) into the microwells, 2 minutes for the hybridization reaction, and ~3 minutes for image analysis.

$$\% \text{ Aggregation}(x) = \left[\left(\frac{\text{Avg}(\text{SAT}(wt))}{\text{Avg}(\text{SAT}(x))} \right) \times 100 \right] - \left[\left(\frac{\text{Avg}(\text{SAT}(wt))}{\text{Avg}(\text{SAT}(\text{blank}))} \right) \times 100 \right] \quad \text{Equation 1}$$

SAT = image saturation value

wt = synthetic wild-type target

As seen in **Figure 3-24**, the *KRAS* wild-type cell lines (H522, BxPC-3, CaCo2 and H1975) produce significant aggregation, whereas the cell lines with *KRAS* mutations (A549, MIA PaCa-2, SW-620 and H2122) show % aggregation values near zero. Importantly, the assay was able to distinguish mutations in all mutant cell lines, even though they display different base substitutions.

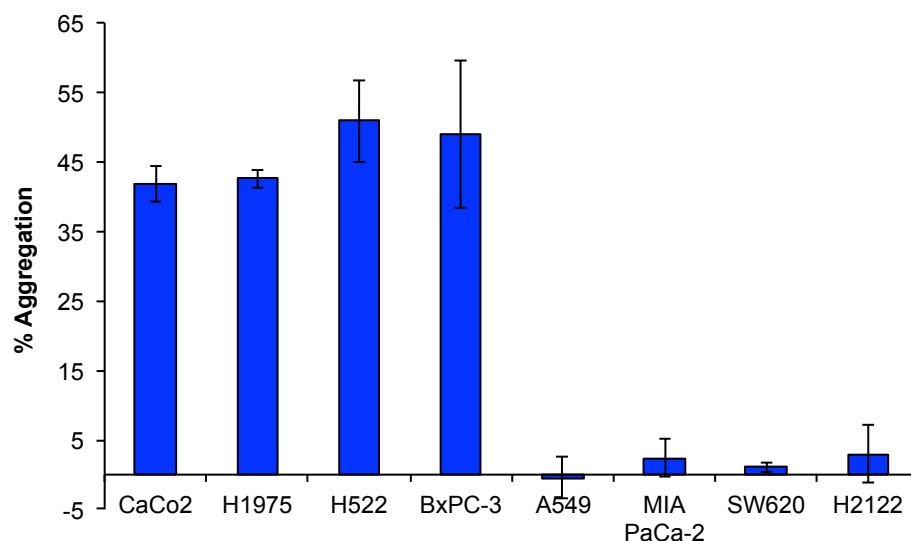


Figure 3-24. *KRAS* mutation analysis of cancer cell lines. Using a PCR-derived target sequence, each cell line was analyzed using the HIA_{MD} assay. The results indicate a significant decrease in the extent of aggregation produced by cell lines bearing a *KRAS* mutation (A549, MIA PaCa-2, SW-620, and H2122) as compared to wild-type cell lines (CaCo2, H1975, H522, and BxPC-3).

3.4.8 Resolution of mutant alleles in the background of wild type DNA

In cancer, the mutated cells are surrounded by stroma, which includes cancer-associated fibroblasts, endothelium, and immune cells – all of which harbor wild type *KRAS* alleles. Therefore, we investigated the ability of HIA_{MD} to detect a *KRAS* mutation in a background of wild-type DNA. Synthetic mutant targets were diluted with synthetic wild-type targets to model mixed samples of the following compositions: 75% mutant, 50% mutant, and 25% mutant. These samples were assayed on the same multi-well chip along with 100% mutant, 0% mutant, and blank (no DNA) samples. As shown in **Figure 3-25**, all samples with mutant content were distinguishable from the wild-type sample, including the sample with only 25% mutant DNA. This detection limit is comparable to

that of sequencing, which is reported to be in the range of 15 to 30% (18, 20, 45). In terms of tumor purity, if we consider a heterozygous genotype of the cancer (allele frequency of 0.5), the tumor purity would need to be at least 50% in order to have at least 25% mutant content.

A threshold value of 36%

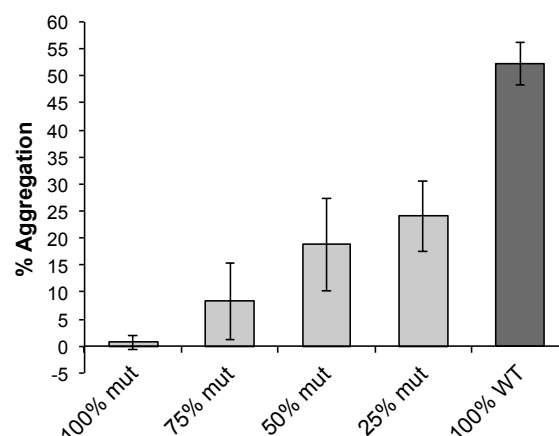


Figure 3-25. Resolution of mutant DNA in a background of wild type DNA. *HIA_{MD}* was applied for the analysis of synthetic samples with mixed genotypes. All samples with mutant content (down to 25% mutant) were significantly distinguishable from a wild-type sample.

aggregation was calculated based on the results of the 100% wild-type sample, using the average aggregation value minus 3 times the standard deviation. Thus, any value below 36% aggregation would be associated with a mutant genotype.

3.4.9 *KRAS* mutation analysis of patient samples

Frozen tissue samples from 20 patients, including 10 lung and 10 colorectal surgical resections, were obtained from pathology at The University of Virginia (see **Table 3-3** for sample characteristics). All tissue samples showed pathologic abnormality, with diagnoses of adenocarcinoma (n=17) or squamous cell carcinoma (n=3). The samples were collected and processed using standard pathology workflow. *KRAS* mutation analysis was performed for each sample in parallel via sequencing and HIA_{MD}.

Sequencing results indicated that 7 (3 colorectal and 4 lung) of the 20 samples (35%) harbored a *KRAS* mutation. Of the mutant samples, 5 were 34G>T and 2 were 35G>A, representing 71.4% and 28.6%, respectively. Notably, all samples that appeared to have a *KRAS* mutation also contained wild-type DNA based on the sequencing electropherograms (see **Fig. 3-26**). This is expected for patient tumor samples, and therefore, we highlight that our sample set, while limited in size, serves as a realistic collection of typical clinical samples.

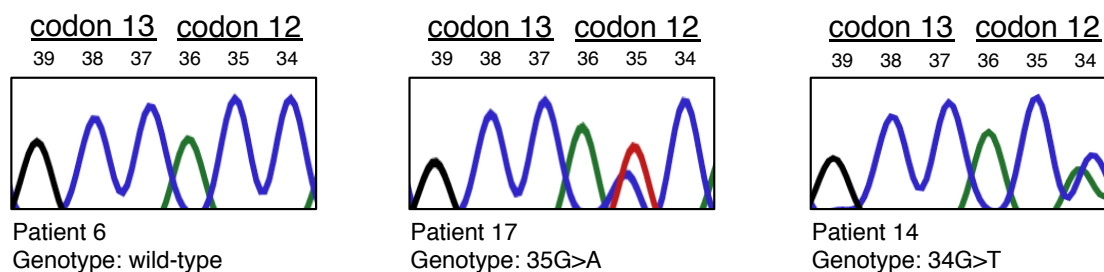


Figure 3-26. Representative sequencing results of 3 patient samples. (Note: the reverse strand was sequenced). Samples with mutant genotypes (e.g., patients 17 and 14) also display wild-type *KRAS* content.

HIA_{MD} assays were performed as described for mutation analysis in cell lines, in which each sample was assayed on 3 chips. % Aggregation values for all tumor DNA samples were calculated and plotted as shown in **Figure 3-27**. The x-axis was set to cross at the set threshold value (36% aggregation) for ease of data interpretation. Samples with a wild-type *KRAS* genotype have values greater than 36% aggregation and therefore lie above the x-axis, whereas samples harboring a *KRAS* mutation result in values lower than 36% aggregation and therefore fall below the x-axis. For all 20

samples, the results of HIA_{MD} analysis were in agreement with sequencing; thus, we report the sensitivity and specificity of our method for the assayed 20 samples to be 100%. Notably, the performance of the HIA_{MD} method was unaffected by the pathologic classification of the tumor (i.e., adenocarcinoma vs. squamous cell carcinoma) or the position and base substitution associated with the mutation (i.e., 34G>T vs. 35G>A).

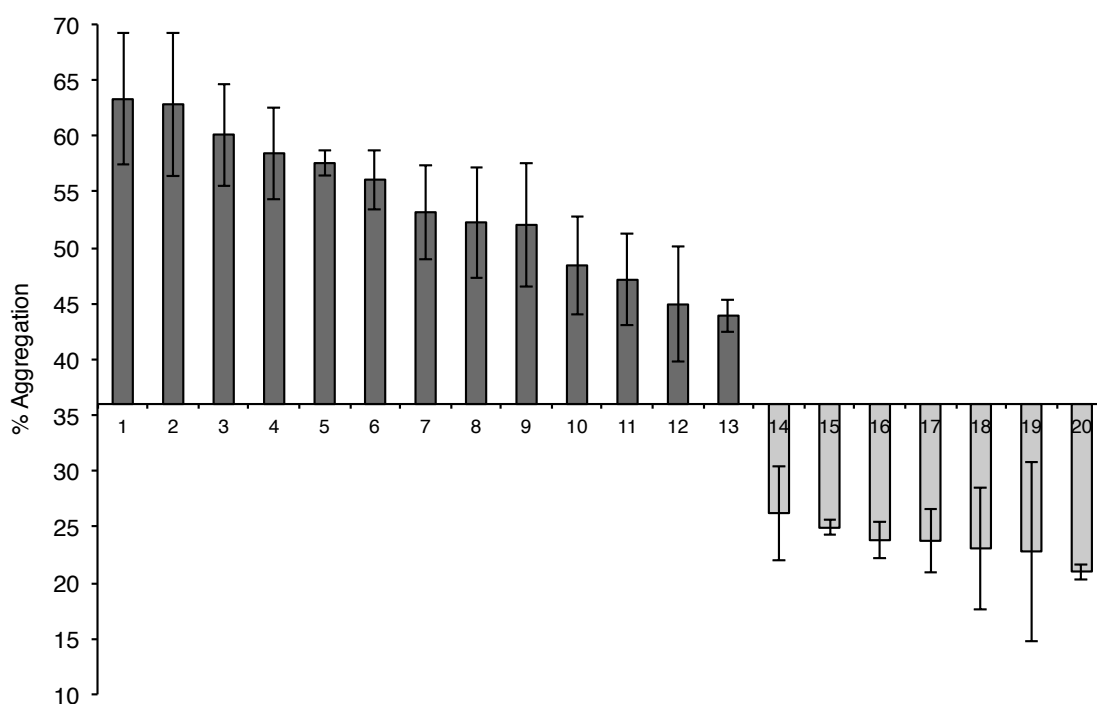


Figure 3-27. HIA_{MD} results from KRAS mutation analysis of patient tissue samples. 36% aggregation was used as the threshold value to distinguish between wild-type (>36%) and mutant (<36%) genotypes. Patient IDs are displayed on the x-axis.

Patient ID	Anatomic Site	Pathologic Diagnosis	Tumor Differentiation	% Tumor by Cellularity	Sequencing Result	HIA_{MD} Result
1	Colon	Adenocarcinoma	Moderate	60	wt	wt
2	Lung	Adenocarcinoma	Well	90	wt	wt
3	Colon	Adenocarcinoma	Well	40	wt	wt
4	Colon	Adenocarcinoma	Poor	80	wt	wt
5	Lung	Squamous Cell Carcinoma	Moderate	70	wt	wt
6	Lung	Adenocarcinoma	Moderate	90	wt	wt
7	Lung	Squamous Cell Carcinoma	Poor	90	wt	wt
8	Colon	Adenocarcinoma	Poor	80	wt	wt
9	Colon	Adenocarcinoma	Poor	80	wt	wt
10	Colon	Adenocarcinoma	Moderate	80	wt	wt
11	Colon	Adenocarcinoma	Moderate	70	wt	wt
12	Lung	Squamous Cell Carcinoma	Moderate	90	wt	wt
13	Lung	Adenocarcinoma	Moderate	90	wt	wt
14	Lung	Adenocarcinoma	Moderate	90	mut (34G>T)	mut
15	Colon	Adenocarcinoma	Moderate	70	mut (34G>T)	mut
16	Lung	Adenocarcinoma	Moderate	95	mut (34G>T)	mut
17	Colon	Adenocarcinoma	Moderate	95	mut (35G>A)	mut
18	Lung	Adenocarcinoma	Poor	85	mut (34G>T)	mut
19	Colon	Adenocarcinoma	Poor	80	mut (35G>A)	mut
20	Lung	Adenocarcinoma	Poor	70	mut (34G>T)	mut

Table 3-3. Patient tumor samples.

3.4.10 Amplicon doublet phenomenon

PCR products to be sequenced were analyzed using the Agilent Bioanalyzer following amplification, in order to quantify the product and guide preparation of the sequencing reaction. In doing so, an interesting trend was observed. 5 of the 20 samples showed doublet peaks in their electropherograms, and all 5 of these samples were identified with a c.34G>T genotype via sequencing (**Fig. 3-28**). Wild-type *KRAS* samples did not display doublet peaks (**Fig. 3-29**), nor did any of the samples possessing a different mutation (i.e., 35G>A) (**Fig. 3-30**). Because all 5 samples with c.34G>T mutations also contained wild-type *KRAS* (see sequencing results), the formation of heteroduplexes (from the annealing of mutant DNA strands to wild-type DNA strands) with altered mobility was likely the cause of the doublet peaks. Indeed, a kink in the helical structure of the heteroduplex DNA could retard its migration through the separation matrix (46). It is interesting, however, that other mixed samples (i.e., containing both mutant and wild-type DNA) with a mutation characterized by a different base substitution at an adjacent nucleotide position did not result in a heteroduplex with altered mobility. This phenomenon could be potentially be exploited as a simply strategy to identify the common *KRAS* c.34G>T mutation.

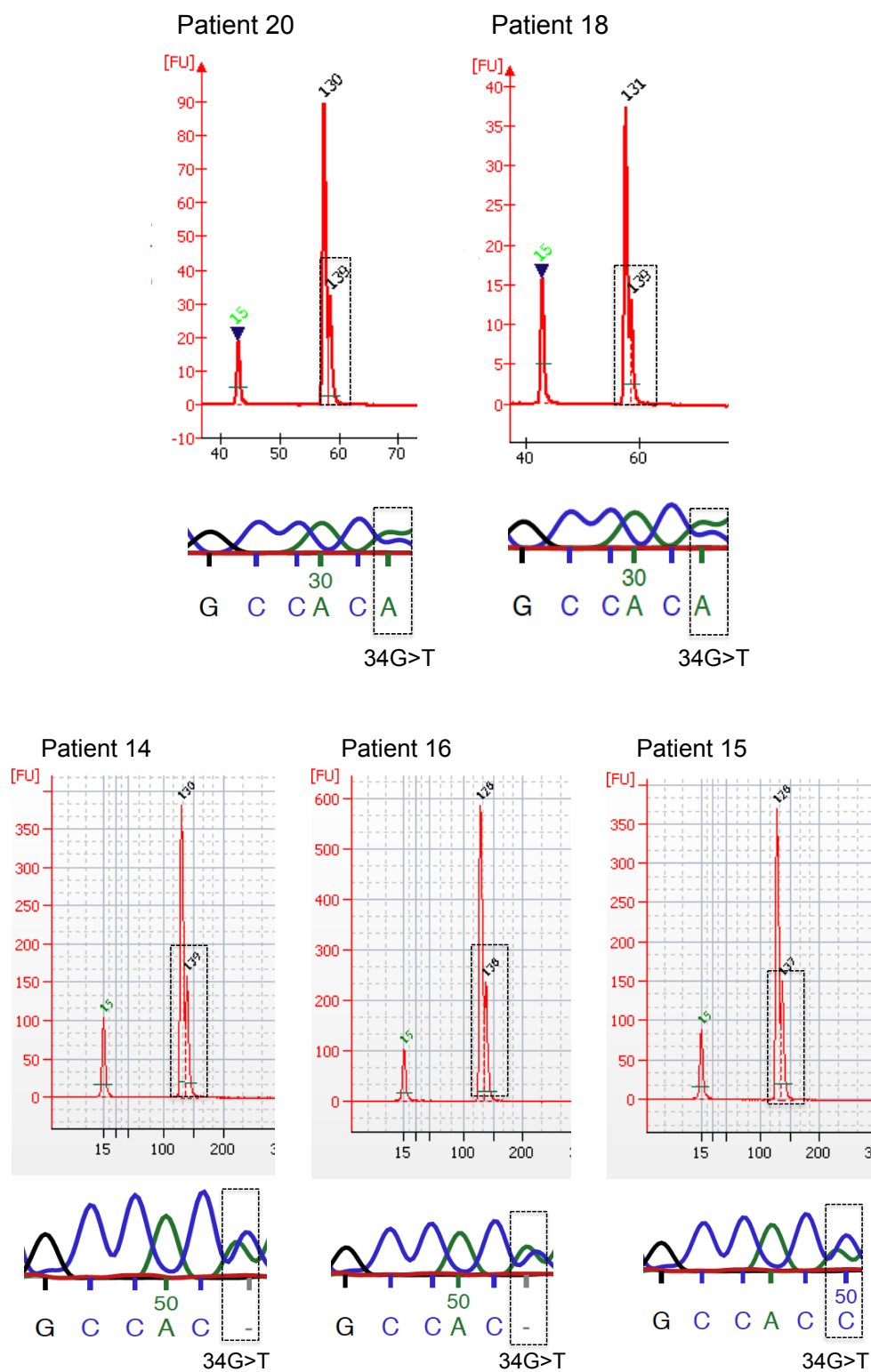


Figure 3-28. Amplicon doublet phenomenon — c.34G>T patient samples. Patient samples with a c.34G>T mutation (detected via sequencing) are characterized by doublet peaks, using the Agilent Bioanalyzer. [Note: the reverse strand was sequenced.]

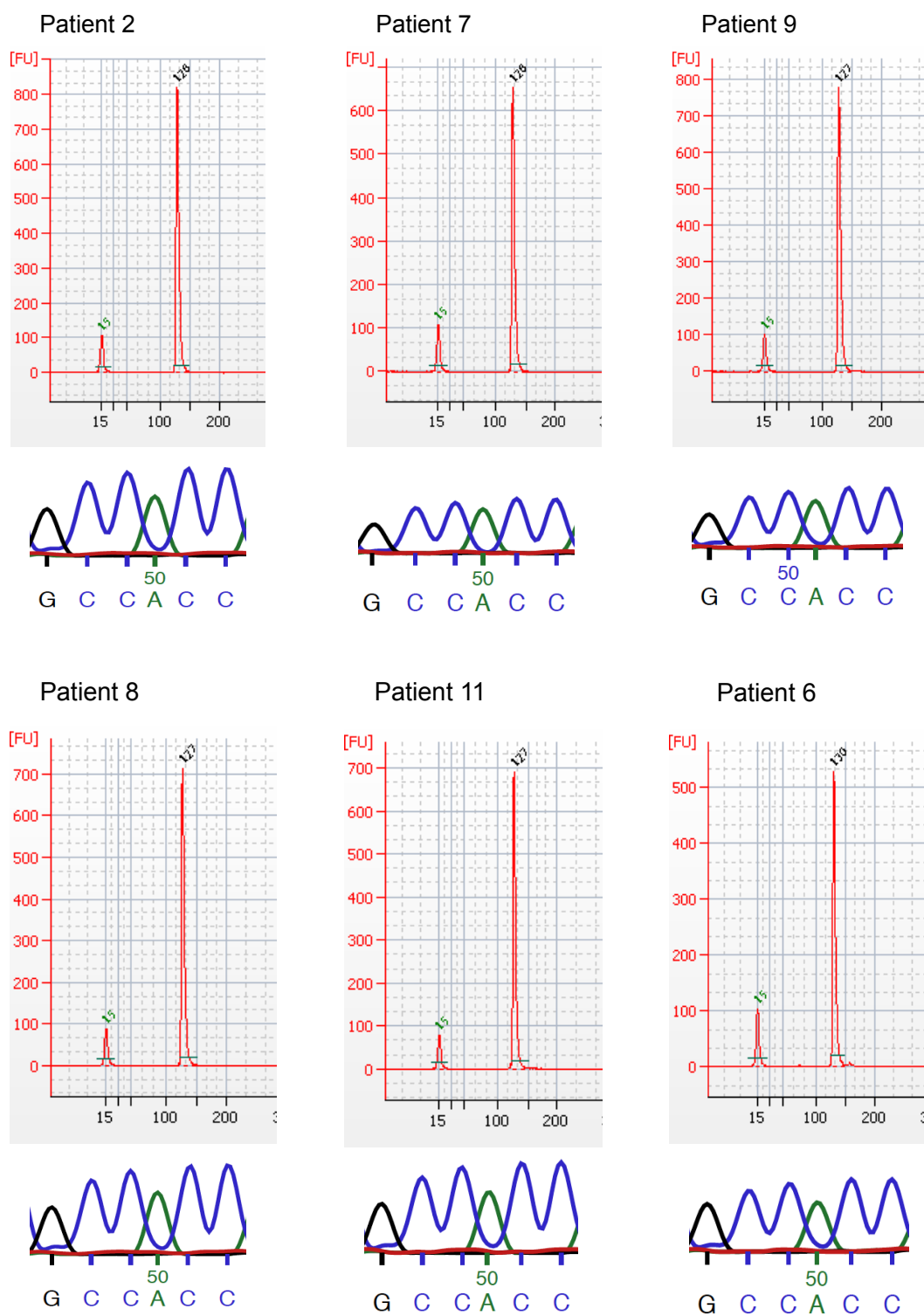


Figure 3-29. Amplicon doublet phenomenon — wild-type patient samples. Patient samples with wild-type KRAS (detected via sequencing) show only a single peak, using the Agilent Bioanalyzer. [Note: the reverse strand was sequenced.]

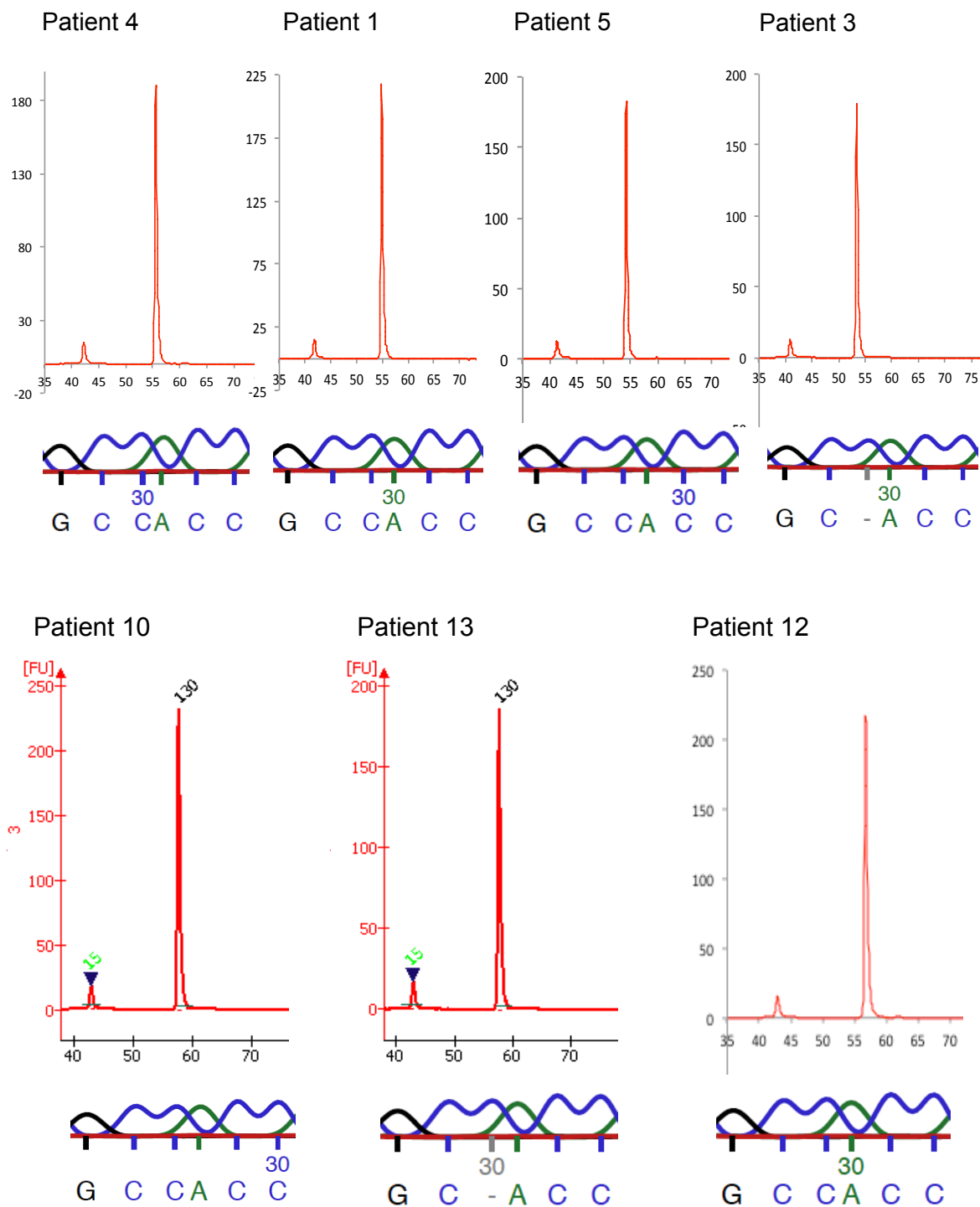


Figure 3-29 cont'd. Amplicon doublet phenomenon — wild-type patient samples. Patient samples with wild-type KRAS (detected via sequencing) show only a single peak, using the Agilent Bioanalyzer. [Note: the reverse strand was sequenced.]

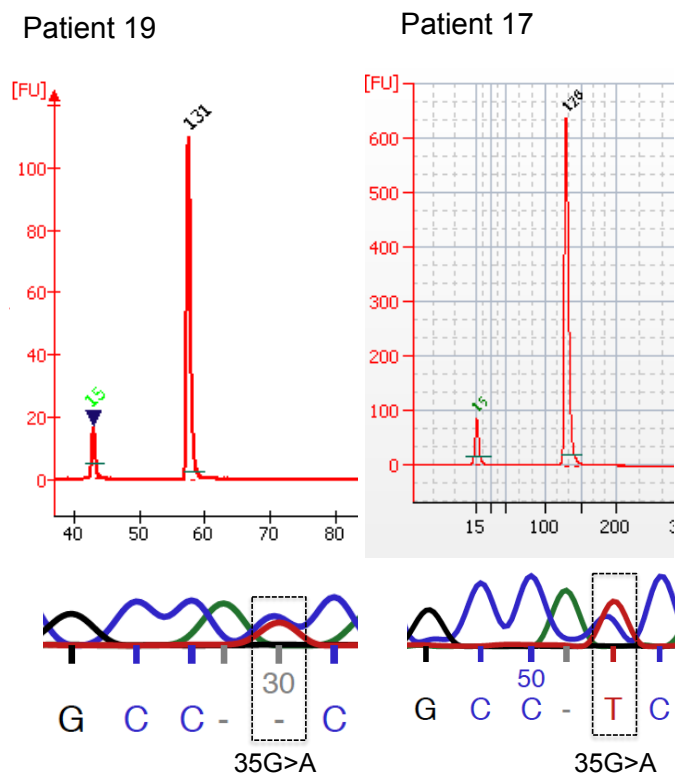


Figure 3-30. Amplicon doublet phenomenon — *c.35G>A* patient samples. Patient samples with a *c.35G>A* mutation (detected via sequencing) display only a single peak, using the Agilent Bioanalyzer. [Note: the reverse strand was sequenced.]

3.5 Concluding Remarks

Targeted therapies are a growing trend in basic and clinical cancer research, and for good reason – the potential for improved treatment outcomes and cost savings is tremendous. The effective implementation of a targeted therapeutic regime requires a practical means for preemptive molecular characterization of the cancer. Here it is shown that HIA_{MD} can be applied for *KRAS* mutation analysis of primary tumors, which is essential for predicting patient sensitivity to EGFR-mediated therapies (47), as well as population

stratification in ongoing therapeutic development (15). Importantly, the analysis is performed in a manner that is both rapid and cost-effective. While a larger study is warranted for validation, this work establishes the potential to apply the HIA_{MD} technology for routine analysis of other, increasingly important genetic markers.

Importantly, we have presented a methodology that is capable of revealing a single base mismatch in a gene segment using only a digital photo of the reaction well for analysis. This is a substantial analytical achievement that presents a vast advantage over other genotyping technologies that typically require highly-sophisticated detection methods, often involving fluorescent labels and complex optics to achieve the sensitivity required to detect a single base change. By design, the HIA_{MD} method allows for the detection of all common *KRAS* mutations in a single, two-minute run using only one set of probes. The robustness of the assay is emphasized by the fact that: 1) the assay can be performed at room temperature, 2) no sample purification following PCR is needed, and 3) no extensive wash steps are needed following the hybridization reaction. These factors allow the analytical process to be kept extremely simple, thereby minimizing the time, effort, and resources required.

The mutation analysis of cell lines described in this work shows proof-of-concept for *KRAS* mutation detection in lung and colorectal cancers with the HIA_{MD} technology. However, the value of *KRAS* mutation analysis requires that the method be validated for use in patient tumor samples. Unlike cell lines, tumor samples are complex, heterogeneous samples, variably contaminated with non-tumor content. Thus, the requirements of a mutation testing method with respect to analytical performance are

considerably more demanding and more difficult to achieve without high technical complexity.

Ultimately, a 100% correlation between results derived from sequencing and HIA_{MD} analysis for *KRAS* mutation screening of 20 lung and colorectal patient tumors is achieved. Furthermore, it is shown that a sample with only 25% *KRAS* mutant content can be detected in a background of wild-type DNA, which is consistent with the detection limit reported using the more costly and cumbersome sequencing method (20, 45). Thus, using HIA_{MD} technology, mutation detection can be performed rapidly and inexpensively without compromising the analytical performance.

Undoubtedly, there are a number of technologies capable of revealing point mutations with higher sensitivities (e.g., next generation sequencing platforms) (48), which may be preferred for the analysis of very low purity samples. However, it must be emphasized that, while impressive, high sensitivity alone does not render a technology appropriate for routine clinical screening. Significant consideration must be made to the cost, complexity, and speed by which the method operates. The inherent features of the HIA_{MD} technology make it a natural fit for use in the routine diagnostic setting. Fundamentally, the method is *simple*. The instrumentation comprises nothing more than a commercial vortexer, a rotating magnet obtained from conventional lab equipment (31), a re-usable plastic microwell chip, a camera, and a laptop. This keeps the method very low in cost (~\$2,500 for all equipment, compared to ~\$100,000 for sequencing instrumentation) (19), and therefore decreases the financial burden for the patient and

healthcare providers. In addition, the simple analytical approach translates to simple technical operation, data analysis, and interpretation, therefore eliminating the need for highly skilled personnel. Furthermore, because the simple optical analysis strategy requires only a camera and a laptop, the potential for using a cell phone for detection is high (49). This transition is an obvious next step and will only increase the suitability of this technology for the point-of-care.

The HIA_{MD} method uses samples processed according to current clinical protocols and is compatible with the clinical laboratory workflow for sample preparation, which includes nucleic acid extraction and PCR amplification. Following amplification, HIA_{MD} analysis for the detection of all common *KRAS* mutations (located in codons 12 and 13) is complete in less than 10 minutes, which includes ~3 minutes for thermal denaturation and snap-cool, ~1 minute to pipette the reagents (sample, buffer, and beads) onto the chip, 2 minutes for the hybridization assay, and ~3 minutes for image analysis. Sequencing analysis, on the other hand, requires further sample preparation, including a tedious PCR cleanup step, and has a turnaround time on the order of days (20, 50). The 12-well microchip can allow 9 patient samples to be analyzed simultaneously, with the inclusion of 3 controls on each chip (wild-type and mutant positive controls, as well as a negative/no DNA control). Additionally, the input of DNA required for the HIA_{MD} assay is 50 ng, as compared to sequencing and other commercial *KRAS* assays, which can require from 100 to 1,600 ng of input DNA (50). Thus, speed, low labor requirements, multiplexing capabilities, and low DNA input are all strategic advantages offered by the HIA_{MD} method and contribute to its suitability for clinical implementation.

With the HIA_{MD} method, confirmation with sequencing may be warranted for samples displaying mutant profiles, as has been suggested for other screening methods (51). However, at a cost of ~\$0.75 per test, HIA_{MD} is an economical choice to first screen for mutations and eliminate the cost and lengthy time-to-result of sequencing for the majority of CRC and lung cancer patients who harbor wild-type *KRAS*. Alternatively, additional reactions using hybridization probes designed for the positive identification of *KRAS* mutations could be incorporated onto the chip to increase the reliability of the results.

This work shows that HIA_{MD} has true potential for integration into our current clinical paradigms, addressing the demand for a practical routine testing methodology. The current direction of clinical oncology research suggests that a technology such as HIA_{MD} will continue to be a highly relevant and valued analytical tool for the facilitation of individualized therapeutic strategies.

3.6 References

1. Duffy MJ, O'Donovan N, Crown J. Use of molecular markers for predicting therapy response in cancer patients. *Cancer Treat Rev.* 2011;37:151-9.
2. Linardou H, Dahabreh IJ, Kanaloupiti D, Siannis F, Bafaloukos D, Kosmidis P, Papadimitriou CA, Murray S. Assessment of somatic k-RAS mutations as a mechanism associated with resistance to EGFR-targeted agents: a systematic review

- and meta-analysis of studies in advanced non-small-cell lung cancer and metastatic colorectal cancer. *Lancet Oncol.* 2008;9:962-72.
3. Raponi M, Winkler H, Dracopoli NC. KRAS mutations predict response to EGFR inhibitors. *Curr Opin Pharmacol.* 2008;8:413-8.
 4. Bos JL. ras oncogenes in human cancer: a review. *Cancer Res.* 1989;49:4682-9.
 5. Siddiqui AD, Piperdi B. KRAS mutation in colon cancer: a marker of resistance to EGFR-I therapy. *Ann Surg Oncol.* 2010;17:1168-76.
 6. Amado RG, Wolf M, Peeters M, Van Cutsem E, Siena S, Freeman DJ, Juan T, Sikorski R, Suggs S, Radinsky R, Patterson SD, Chang DD. Wild-type KRAS is required for panitumumab efficacy in patients with metastatic colorectal cancer. *J Clin Oncol.* 2008;26:1626-34.
 7. Baynes RD, Gansert J. KRAS mutational status as a predictor of epidermal growth factor receptor inhibitor efficacy in colorectal cancer. *Am J Ther.* 2009;16:554-61.
 8. Di Fiore F, Blanchard F, Charbonnier F, Le Pessot F, Lamy A, Galais MP, Bastit L, Killian A, Sesboue R, Tuech JJ, Queuniet AM, Paillot B, Sabourin JC, Michot F, Michel P, Frebourg T. Clinical relevance of KRAS mutation detection in metastatic colorectal cancer treated by Cetuximab plus chemotherapy. *Br J Cancer.* 2007;96:1166-9.
 9. Karapetis CS, Khambata-Ford S, Jonker DJ, O'Callaghan CJ, Tu D, Tebbutt NC, Simes RJ, Chalchal H, Shapiro JD, Robitaille S, Price TJ, Shepherd L, Au HJ, Langer C, Moore MJ, Zalcberg JR. K-ras mutations and benefit from cetuximab in advanced colorectal cancer. *N Engl J Med.* 2008;359:1757-65.

10. Lievre A, Bachet JB, Le Corre D, Boige V, Landi B, Emile JF, Cote JF, Tomasic G, Penna C, Ducreux M, Rougier P, Penault-Llorca F, Laurent-Puig P. KRAS mutation status is predictive of response to cetuximab therapy in colorectal cancer. *Cancer Res.* 2006;66:3992-5.
11. Pao W, Wang TY, Riely GJ, Miller VA, Pan Q, Ladanyi M, Zakowski MF, Heelan RT, Kris MG, Varmus HE. KRAS mutations and primary resistance of lung adenocarcinomas to gefitinib or erlotinib. *PLoS Med.* 2005;2:e17.
12. Murray S, Dahabreh IJ, Linardou H, Manoloukos M, Bafaloukos D, Kosmidis P. Somatic mutations of the tyrosine kinase domain of epidermal growth factor receptor and tyrosine kinase inhibitor response to TKIs in non-small cell lung cancer: an analytical database. *J Thorac Oncol.* 2008;3:832-9.
13. van Zandwijk N, Mathy A, Boerrigter L, Ruijter H, Tielen I, de Jong D, Baas P, Burgers S, Nederlof P. EGFR and KRAS mutations as criteria for treatment with tyrosine kinase inhibitors: retro- and prospective observations in non-small-cell lung cancer. *Ann Oncol.* 2007;18:99-103.
14. Mancl EE, Kolesar JM, Vermeulen LC. Clinical and economic value of screening for Kras mutations as predictors of response to epidermal growth factor receptor inhibitors. *Am J Health Syst Pharm.* 2009;66:2105-12.
15. Vakiani E, Solit DB. KRAS and BRAF: drug targets and predictive biomarkers. *J Pathol.* 2011;223:219-29.
16. Roberts PJ, Stinchcombe TE. KRAS mutation: should we test for it, and does it matter? *Journal of Clinical Oncology.* 2013;31:1112-21.

17. van Krieken JH, Jung A, Kirchner T, Carneiro F, Seruca R, Bosman FT, Quirke P, Flejou JF, Plato Hansen T, de Hertogh G, Jares P, Langner C, Hoefler G, Ligtenberg M, Tiniakos D, Tejpar S, Bevilacqua G, Ensari A. KRAS mutation testing for predicting response to anti-EGFR therapy for colorectal carcinoma: proposal for an European quality assurance program. *Virchows Arch.* 2008;453:417-31.
18. Tsiatis AC, Norris-Kirby A, Rich RG, Hafez MJ, Gocke CD, Eshleman JR, Murphy KM. Comparison of Sanger sequencing, pyrosequencing, and melting curve analysis for the detection of KRAS mutations: diagnostic and clinical implications. *J Mol Diagn.* 2010;12:425-32.
19. Weichert W, Schewe C, Lehmann A, Sers C, Denkert C, Budczies J, Stenzinger A, Joos H, Landt O, Heiser V, Rocken C, Dietel M. KRAS genotyping of paraffin-embedded colorectal cancer tissue in routine diagnostics: comparison of methods and impact of histology. *J Mol Diagn.* 2010;12:35-42.
20. Jancik S, Drabek J, Berkovcova J, Xu YZ, Stankova M, Klein J, Kolek V, Skarda J, Tichy T, Grygarkova I, Radzioch D, Hajdich M. A comparison of Direct sequencing, Pyrosequencing, High resolution melting analysis, TheraScreen DxS, and the K-ras StripAssay for detecting KRAS mutations in non small cell lung carcinomas. *J Exp Clin Cancer Res.* 2012;31:79.
21. Beau-Faller M, Blons H, Domerg C, Gajda D, Richard N, Escande F, Solassol J, Denis MG, Cayre A, Nanni-Metellus I, Olschwang S, Lizard S, Piard F, Pretet JL, de Fraipont F, Bieche I, de Cremoux P, Rouquette I, Bringuier PP, Mosser J, Legrain M, Voegeli AC, Saulnier P, Morin F, Pignon JP, Zalcman G, Cadranel J. A

- multicenter blinded study evaluating EGFR and KRAS mutation testing methods in the clinical non-small cell lung cancer setting--IFCT/ERMETIC2 Project Part 1: Comparison of testing methods in 20 French molecular genetic National Cancer Institute platforms. *J Mol Diagn*. 2014;16:45-55.
22. Ogino S, Kawasaki T, Brahmandam M, Yan L, Cantor M, Namgyal C, Mino-Kenudson M, Lauwers GY, Loda M, Fuchs CS. Sensitive sequencing method for KRAS mutation detection by Pyrosequencing. *J Mol Diagn*. 2005;7:413-21.
 23. Weng X, Jiang H, Li D. Microfluidic DNA hybridization assays. *Microfluidics and nanofluidics*. 2011;11:367-83.
 24. Yim SC, Park HG, Chang HN, Cho DY. Array-based mutation detection of BRCA1 using direct probe/target hybridization. *Anal Biochem*. 2005;337:332-7.
 25. Ramsay G. DNA chips: state-of-the art. *Nature biotechnology*. 1998;16:40-4.
 26. Caillat P, David D, Belleville M, Clerc F, Massit C, Revol-Cavalier F, Peltie P, Livache T, Bidan G, Roget A. Biochips on CMOS: an active matrix address array for DNA analysis. *Sensors and Actuators B: Chemical*. 1999;61:154-62.
 27. Pease AC, Solas D, Sullivan EJ, Cronin MT, Holmes CP, Fodor SP. Light-generated oligonucleotide arrays for rapid DNA sequence analysis. *Proc Natl Acad Sci U S A*. 1994;91:5022-6.
 28. Lopez-Crapez E, Chypre C, Saavedra J, Marchand J, Grenier J. Rapid and large-scale method to detect K-ras gene mutations in tumor samples. *Clin Chem*. 1997;43:936-42.

29. Peytavi R, Raymond FR, Gagne D, Picard FJ, Jia G, Zoval J, Madou M, Boissinot K, Boissinot M, Bissonnette L, Ouellette M, Bergeron MG. Microfluidic device for rapid (<15 min) automated microarray hybridization. *Clin Chem*. 2005;51:1836-44.
30. Leslie DC, Li J, Strachan BC, Begley MR, Finkler D, Bazydlo LAL, Barker NS, Haverstick DM, Utz M, Landers JP. New detection modality for label-free quantification of DNA in biological samples via superparamagnetic bead aggregation. *Journal of the American Chemical Society*. 2012;134:5689-96.
31. Nelson DA, Strachan BC, Sloane HS, Li J, Landers JP. Dual-force aggregation of magnetic particles enhances label-free quantification of DNA at the sub-single cell level. *Analytica chimica acta*. 2014;819:34-41.
32. Strachan BC, Sloane HS, Lee JC, Leslie DC, Landers JP. Investigation of the DNA target design parameters for effective hybridization-induced aggregation of particles for the sequence-specific detection of DNA. *Analyst*. 2015;140:2008-15.
33. Kabilov MR, Pyshnyi DV. Analytical consideration of the selectivity of oligonucleotide hybridization. *Journal of Biophysical Chemistry*. 2011;2:75.
34. Gallegos Ruiz MI, Floor K, Rijmen F, Grünberg K, Rodriguez JA, Giaccone G. EGFR and K-ras mutation analysis in non-small cell lung cancer: comparison of paraffin embedded versus frozen specimens. *Analytical Cellular Pathology*. 2007;29:257-64.
35. Lang AH, Drexel H, Geller-Rhomberg S, Stark N, Winder T, Geiger K, Muendlein A. Optimized allele-specific real-time PCR assays for the detection of common

- mutations in KRAS and BRAF. *The Journal of Molecular Diagnostics*. 2011;13:23-8.
36. Sun Y, Kwok YC, Nguyen N-T. Low-pressure, high-temperature thermal bonding of polymeric microfluidic devices and their applications for electrophoretic separation. *Journal of Micromechanics and Microengineering*. 2006;16:1681.
 37. Kim S, Misra A. SNP genotyping: technologies and biomedical applications. *Annu Rev Biomed Eng*. 2007;9:289-320.
 38. SantaLucia Jr J, Hicks D. The thermodynamics of DNA structural motifs. *Annu Rev Biophys Biomol Struct*. 2004;33:415-40.
 39. Dieffenbach CW, Lowe TM, Dveksler GS. General concepts for PCR primer design. *PCR Methods Appl*. 1993;3:S30-7.
 40. Lucarelli F, Marrazza G, Mascini M. Design of an optimal allele-specific oligonucleotide probe for the efficient discrimination of a thermodynamically stable (G x T) mismatch. *Anal Chim Acta*. 2007;603:82-6.
 41. Maekawa M, Nagaoka T, Taniguchi T, Higashi H, Sugimura H, Sugano K, Yonekawa H, Satoh T, Horii T, Shirai N, Takeshita A, Kanno T. Three-dimensional microarray compared with PCR-single-strand conformation polymorphism analysis/ DNA sequencing for mutation analysis of K-ras codons 12 and 13. *Clin Chem*. 2004;50:1322-7.
 42. Steinbach C, Steinbrucker C, Pollok S, Walther K, Clement JH, Chen Y, Petersen I, Cialla-May D, Weber K, Popp J. KRAS mutation screening by chip-based DNA

- hybridization - a further step towards personalized oncology. *Analyst*. 2015;140:2747-54.
43. Cisse II, Kim H, Ha T. A rule of seven in Watson-Crick base-pairing of mismatched sequences. *Nature structural & molecular biology*. 2012;19:623-7.
 44. Forbes SA, Bindal N, Bamford S, Cole C, Kok CY, Beare D, Jia M, Shepherd R, Leung K, Menzies A. COSMIC: mining complete cancer genomes in the Catalogue of Somatic Mutations in Cancer. *Nucleic acids research*. 2010gkq929.
 45. Ney JT, Froehner S, Roesler A, Buettner R, Merkelbach-Bruse S. High-resolution melting analysis as a sensitive prescreening diagnostic tool to detect KRAS, BRAF, PIK3CA, and AKT1 mutations in formalin-fixed, paraffin-embedded tissues. *Arch Pathol Lab Med*. 2012;136:983-92.
 46. Glavac D, Dean M. Applications of heteroduplex analysis for mutation detection in disease genes. *Human mutation*. 1995;6:281-7.
 47. Allegra CJ, Jessup JM, Somerfield MR, Hamilton SR, Hammond EH, Hayes DF, McAllister PK, Morton RF, Schilsky RL. American Society of Clinical Oncology provisional clinical opinion: testing for KRAS gene mutations in patients with metastatic colorectal carcinoma to predict response to anti-epidermal growth factor receptor monoclonal antibody therapy. *J Clin Oncol*. 2009;27:2091-6.
 48. Tzvetkov M, von Ahsen N. Pharmacogenetic screening for drug therapy: from single gene markers to decision making in the next generation sequencing era. *Pathology*. 2012;44:166-80.

49. DuVall JA, Borba JC, Shafagati N, Luzader D, Shukla... N. Optical Imaging of Paramagnetic Bead-DNA Aggregation Inhibition Allows for Low Copy Number Detection of Infectious Pathogens. *PloS one*. 2015
50. de Castro DG, Angulo B, Gomez B, Mair D, Martinez R, Suarez-Gauthier A, Shieh F, Velez M, Brophy VH, Lawrence HJ. A comparison of three methods for detecting KRAS mutations in formalin-fixed colorectal cancer specimens. *British journal of cancer*. 2012;107:345-51.
51. Nollau P, Wagener C. Methods for detection of point mutations: performance and quality assessment. *Clinical chemistry*. 1997;43:1114-28.

4 Warfarin Genotyping with Hybridization-Induced Aggregation on a Poly(ethylene terephthalate) Microdevice

4.1 Overview

Warfarin, a commonly prescribed oral anticoagulant, is burdened by a narrow therapeutic index and high inter-individual variability in response, making it the second leading cause of drug-related emergency room visits. Since genetic factors contribute significantly to warfarin sensitivity, a genotype-guided dosing strategy may reduce the occurrence of adverse events. While numerous methods have been demonstrated for warfarin genotyping, the specifications of most assays with respect to turnaround time and cost are not ideal for routine testing.

In this work, a multiplex allele-specific PCR reaction was used to generate products corresponding to 3 genetic variants associated with warfarin sensitivity [*CYP2C9* *2, *CYP2C9* *3, and *VKORC1* (1173C>T)] and an internal control product. The products were detected simultaneously on a poly(ethylene terephthalate) (PET) microdevice using Hybridization-induced Aggregation (HIA), a unique bead-based technique for sequence-specific detection. The genotyping results of 23 patient DNA samples using this approach were in 100% concordance with the results of a validated test (WARFGENO test, ARUP laboratories). These results were obtained in approximately 15 minutes following PCR. Additionally, the PCR reaction was

successfully transferred to a PeT chip, which facilitated accurate genotyping results from patient DNA samples in under an hour.

Multiplex allele-specific PCR coupled with HIA detection provides a simple, rapid, and affordable approach to warfarin genotyping. By demonstrating both chemistries on PET microdevices, the potential for integration on a single device for sample-to-answer genotyping is demonstrated.

4.2 Introduction

Pharmacogenetics, or the principle of relating genetic characteristics to therapeutic response, has long been recognized as a promising strategy to optimize patient care. By exploiting pharmacogenetics, treatment decisions can be tailored based on an individual's genotype in order to maximize therapeutic efficacy and minimize adverse effects. An important case study for pharmacogenetics involves warfarin, the most widely-used oral anticoagulant worldwide (1). Warfarin is notoriously challenging to prescribe due to the combination of a narrow therapeutic window and high inter-individual variability in dose requirement. The severity of these challenges is apparent in the alarmingly high rate of adverse effects associated with warfarin. Indeed, warfarin is the second leading cause of drug-related emergency room visits (2) and a prevalent cause of drug-related mortality (3).

In addition to clinical factors (e.g., age, race, and drug interactions), genetic factors have been implicated as important predictors of warfarin sensitivity. In fact, roughly 40% of inter-patient differences in warfarin response is attributed to alterations in two key genes: cytochrome P450 2C9 (*CYP2C9*), which encodes the enzyme that metabolizes S-warfarin, and vitamin K epoxide reductase complex subunit 1 (*VKORC1*), which encodes the molecular target of warfarin (4). Variants of *CYP2C9* (specifically, *2 and *3) and *VKORC1* (-1639G>A or 1173C>T), result in decreased warfarin dose requirements as well as a greater risk of experiencing adverse effects (5,6). Given the consistent relationship between these genetic factors and warfarin response, a patient's *CYP2C9* and *VKORC1* genotype is useful in selecting a starting dose – a point that is affirmed on the FDA label for warfarin (7).

There is a wealth of research indicating that using genotypic information allows a more accurate prediction of warfarin dose (8-10), and furthermore, that it can actually reduce the occurrence of adverse events (11,12). A compelling example is a study by Epstein et al., which showed that patients who were genotyped experienced 43% fewer hospitalizations for bleeding or thromboembolism compared with non-genotyped control groups (13). Despite the strong evidence, genotype-guided warfarin dosing in clinical practice is still limited. One explanation for this is – and a topic of considerable debate – is the lack of large randomized controlled studies that show clinical utility (14-16). Another commonly cited barrier for clinical implementation is the turnaround time and cost of genotyping (1,17). The availability of a technology that can deliver rapid, on demand results is of particular importance for warfarin testing since genotypic

information is most useful prior to initiation of warfarin (10), and a delay in treatment initiation is typically not possible (1). Additionally, cost must be minimized for the widespread implementation of a routine genetic testing regime to be financially feasible, especially since most insurance companies have refused to cover warfarin testing (18). Clearly, improvements in genotyping technology, with an emphasis on speed and affordability, must be prioritized.

There have been a number of assays demonstrated for warfarin genotyping, including allele-specific PCR (19-21), allele-specific isothermal amplification (22), and PCR with microarray hybridization (23), among others. However, the specifications of most assays with respect to time-to-result and cost are not optimal for a routine testing scenario (24). The detection modality associated with these methods is often the limiting factor in achieving ideal specifications. Detection typically involves sensitive labels (e.g., fluorescent) that require technically-sophisticated optics and/or other equipment (19,23), which ultimately contradict the simplicity necessary for a practical clinical testing technology. Further, most methods require multiple processing steps between amplification and result (e.g., sample clean-up or post-hybridization wash steps) (23), which complicates the analytical process and limits the turnaround time.

In this work, we implement a unique detection method on a microscale platform, known as Hybridization-induced Aggregation (HIA) (25), to address the aforementioned drawbacks associated with conventional technologies. HIA relies on a pair of oligonucleotide probes conjugated to magnetic beads to provide sequence-specific nucleic acid detection. When a target sequence is present, the probes will hybridize to it

(one on each end of the target sequence), tethering the beads together and inducing bead aggregation. A digital photo is taken and processed using a simple image analysis algorithm to relate the extent of aggregation to image saturation (see **Fig. 4-1B** and **C**). In the absence of the complimentary target sequence, the beads remain dispersed throughout the chamber, and thus a high saturation value is produced. However, when the beads are aggregated, the saturated area in the chamber is reduced, yielding a lower saturation value. In this way, quantitative target detection is achieved without additional labels or complex detection instrumentation.

Until now, all reports of HIA assays (including the work described thus far in this dissertation) have taken place on poly(methyl methacrylate) (PMMA) microdevices in an open-well format (25-27). Here, the HIA assay is transitioned to a poly(ethylene terephthalate) (PeT) microdevice, which features a closed-chamber format, decreased reaction volumes, and greater multiplexing capabilities. The devices are created as circular disks, making it simple to exploit centrifugal force for fluid manipulation.

To achieve sufficient sensitivity and specificity with this genotyping assay, HIA was combined with a multiplex allele-specific PCR reaction. This PCR reaction was adapted from a tetraprimer amplification refractory mutation system (T-ARMS) previously reported by Poe et al. (28), which relies on primer specificity to anneal to a SNP site at its 3' end. The T-ARMS reaction incorporated four primers per locus, forming one or two (in the case of a heterozygous genotype) allele-specific products and a control product associated with each locus (i.e., *CYP2C9* *2, *CYP2C9* *3, and *VKORC1* (1173C>T)). For simplicity in detection, the T-ARMS reaction was modified here by

eliminating one set of primers per locus, such that only one product, associated with the mutant genotype, was possible for each locus. Thus, any aggregation detected in HIA analysis would be indicative of a mutant allele (see **Fig. 4-1**). Additionally, a primer set for an internal control, corresponding to a short segment of the *KRAS* gene, was incorporated into the reaction. *KRAS*, while not typically employed as an internal control, was ideal for this assay since a HIA-based method for its detection has previously been demonstrated (26). The inclusion of an internal control was important in eliminating the possibility of false negatives due to failed amplification.

The basic principles of this assay are depicted in **Figure 4-1**. First, multiplex allele-specific PCR is performed to amplify mutation-specific products, one corresponding to each of the three allelic variants associated with warfarin sensitivity. Then, using separate HIA reactions with oligonucleotide probes complimentary to each PCR amplicon, the products are detected simultaneously, on one chip, to generate a complete mutation profile in less than 15 minutes following PCR. Initially, PCR was performed in-tube using conventional equipment. It is then shown that the multiplex allele-specific PCR can be performed on a PeT chip prior to HIA detection, for total analysis from patient DNA in under an hour. These results indicate the possibility for integration of these chemistries on a single microdevice to provide sample-to-answer genotyping.



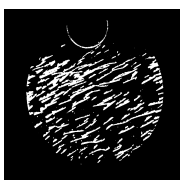
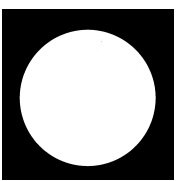
		GENOTYPE	
		mutant	wild-type
A	allele-specific PCR	amplification	NO amplification
B	HIA	aggregation 	NO aggregation 
C	image analysis	LOW saturation 	HIGH saturation 

Figure 4-1. Assay Principles. A) Allele-specific PCR is used to amplify gene segments only when the mutation in question is present. B) HIA reactions are used to detect the mutant-specific PCR products, and images of the HIA chambers are taken as shown here. (Slight evaporation during the assay is observed, as indicated by the meniscus in seen in each photo.) In the absence of the mutant-associated target sequence, the beads remain dispersed throughout the chamber. C) Image analysis quantifies the extent of aggregation in terms of saturation. In the absence of aggregation (wild-type), the beads remain disperse throughout the chamber, yielding a HIGH saturation value. When the beads are aggregated (mutant), the saturated area is reduced, corresponding to a LOW saturation value.

4.3 Materials and Methods

4.3.1 Oligonucleotides

PCR primers and biotinylated probe sequences (for HIA assays) were synthesized by Eurofins MWG Operon (Huntsville, AL). All oligonucleotide sequences are listed in **Table 4-1**.

Oligonucleotide		Sequence
PCR Primers	<i>CYP2C9</i> *2 Fwd	5'-GGATGGGGAAGAGGAcCATTGAGGgCt-3'
	<i>CYP2C9</i> *2 Rev	5'-CCGCTTCACATaAGCTAAcAACCAGaACTCAT-5'
	<i>CYP2C9</i> *3 Fwd	5'-TGTGGTGCAGGAGGTCCAGAGATgCc-3'
	<i>CYP2C9</i> *3 Rev	5'-CCAGACACTAGGACCTcTTACAAACCTTTATtGC-3'
	<i>VKORC1</i> (1173C>T) Fwd	5'-ACTTAAGGTCTAAGATGAAAAGCAGGGCCTAC-3'
	<i>VKORC1</i> (1173C>T) Rev	5'-TCCTCTGTTCCCCCACCTCCCATCCTtGTCCAAtA-3'
	<i>KRAS</i> Fwd	5'- GACTGAATATAAACTTGTGGTAGTTGGA -3'
	<i>KRAS</i> Rev	5'-CATATTCGTCCACAAAATGATTCTG-3'
HIA Probes	<i>CYP2C9</i> *2 5' Probe	5'-[Biotin-TEG]TTTTTTGGATGGGGAAGAGGACCATTGAGGGCT-3'
	<i>CYP2C9</i> *2 3' Probe	5'-ATGAGTTCTGGTTGTAGCTTATGTGAAGCGGTTTTTT[Biotin-TEG-Q]-3'
	<i>CYP2C9</i> *3 5' Probe	5'-[Biotin-TEG]TTTTTTGTGGTGCAGGAGGTCCAGAGATGCC-3'
	<i>CYP2C9</i> *3 3' Probe	5'-GCAATAAAGGTTTGTGAAGGTCCTAGTGTCTGGTTTTTT[Biotin-TEG-Q]-3'
	<i>VKORC1</i> (1173C>T) 5' Probe	5'-[Biotin-TEG]TTTTTTACTTAAGGTCTAAGATGAAAAGCAGGGCCTAC-3'
	<i>VKORC1</i> (1173C>T) 3' Probe	5'-TATTGGACAAGGATGGGAGGTGGGGGAACAGAGGATTTTT[Biotin-TEG-Q]-3'
	<i>KRAS</i> 5' Probe	5'- [Biotin-TEG]TTTTTTCTGAATTAGCTGTATCGTCAAGGCACTC -3'
	<i>KRAS</i> 3' Probe	5'- CTACGCCiCCAGCTCTTTTT[Biotin-TEG-Q] -3'

Table 4-1. Oligonucleotide sequences. Lowercase letters in primer sequences indicate intentional mismatches versus the genomic template. Primer sequences for *2, *3, and 1173C>T products are described by Poe et al (28).

4.3.2 Bead preparation

Biotinylated probe oligonucleotides were conjugated to 1 μm (diameter) streptavidin-coated beads (Dynabeads MyOne Streptavidin C1 superparamagnetic beads; Invitrogen, Oslo, Norway) in accordance with the manufacturer's instructions. Following immobilization and wash steps, the beads were brought up in 1X binding/washing buffer (5 mM Tris-HCl (pH 7.5), 0.5 mM EDTA, 1 M NaCl) in a volume equivalent to the initial volume of stock beads, to maintain a concentration of $\sim 7\text{-}10 \times 10^9$ beads per mL. Each pair of beads used for HIA assays was composed of a 1:1 mixture of forward and reverse probe-bound beads.

4.3.3 Patient samples

De-identified patient samples were acquired from ARUP laboratories (Salt Lake City, UT) in the form of extracted DNA in elution buffer from a MagNA Pure LC DNA Isolation Kit (Roche, Indianapolis, IN). The samples were previously genotyped via the WARFGENO test (ARUP laboratories), which relies on PCR and fluorescence monitoring to test for *CYP2C9* *2, *CYP2C9* *3, and *VKORC1* -1639G>A variants.

4.3.4 PCR (conventional)

25 µL PCR reactions were composed of 1X MyTaq Reaction Buffer and 0.04 U/µL MyTaq HS DNA Polymerase (Bioline Reagents Ltd., London, UK), 0.3 µM *CYP2C9* *2 forward and reverse primers, 0.2 µM *CYP2C9* *3 forward and reverse primers, 0.2 µM *VKORC1* (1173C>T) forward and reverse primers, 0.4 µM *KRAS* primers, and ~25 ng of DNA. A GeneAmp PCR System 2700 thermal cycler (Applied Biosystems, Foster City, CA) was used with the following thermal cycling parameters: 2 min at 95 °C; 10 cycles of 15 s at 95 °C, 30 s at 62 °C, 10 s at 72 °C; 25 cycles of 15 s at 95 °C, 30 s at 60 °C, 10 s at 72 °C; 2 min at 72 °C.

4.3.5 PCR (microchip)

25 µL PCR reactions were composed of 1X MyTaq Reaction Buffer and 0.1 U/µL MyTaq HS DNA Polymerase (Bioline Reagents Ltd., London, UK), 0.4 µg/µL BSA, 0.3 µM *CYP2C9* *2 forward and reverse primers, 0.3 µM *CYP2C9* *3 forward and reverse primers, 0.3 µM *VKORC1* (1173C>T) forward and reverse primers, 0.5 µM *KRAS*

primers, and ~50 ng of DNA. The thermal cycling parameters were as follows: 1 min at 95 °C; 10 cycles of 10 s at 95 °C, 18 s at 60 °C, 15 s at 72 °C; 35 cycles of 10 s at 95 °C, 18 s at 58 °C, 15 s at 72 °C; 2 min at 72 °C. Custom built instrumentation comprising a pair of Peltier thermoelectric cooling modules (Laird Part 430446-503) clamped around the PCR reservoir was used for temperature cycling. Temperatures were measured with a T-type thermocouple and digitized before being sent to a Parallax Propeller microcontroller (Parallax Part 32150). These signals provided feedback so that temperatures inside the PCR chamber could be regulated with a Proportion-Integral control algorithm run on the microcontroller. Peltier throttle control signals were generated by the microcontroller, converted to an analog signal with a digital to analog converter (Analog devices AD557), and amplified by a high current operational amplifier (Texas Instruments Part OPA548), before reaching the Peltier modules. User inputs related to thermocycling temperatures and duration were sent to the microcontroller via a text-based serial terminal interface.

4.3.6 Microchip electrophoresis

During PCR optimization, products were analyzed using Agilent 2100 DNA 1000 series II kits and instrumentation (Agilent Technologies, Santa Clara, CA).

4.3.7 HIA instrumentation

4.3.7.1 DFA system

The dual force aggregation (DFA) instrumentation was developed in-house and is described in detail in **Chapter 2**. Briefly, the set-up consists of a vortexer (MS3 basic vortexer, IKA, Wilmington, NC) to hold the chip and provide gentle agitation, and a rotating magnet positioned above the chip to provide additional mixing of the probe-bound magnetic beads.

4.3.7.2 Spinning platform

Instrumentation used for HIA on PeT devices was designed and built in house. As shown in **Figure 4-5C**, the set-up includes a spinning platform for the chip and a rotating disc with attached magnets, which provides efficient mixing of the magnetic bead-bound probes with the sample during the HIA assay. Motion profiles were created using a bipolar stepper motor (Sanmotion Type SS2422-5041). Rotation speeds were controlled in an open loop fashion by changing the frequency of step pulses sent to the motor. These pulses, produced by a Parallax Propeller microcontroller (Parallax Part 32150), were decoded and amplified by a Texas Instruments DRV8825 IC based microstepping breakout board (Pololu Part 2133) in full step mode, creating a step size of 1.8 degrees. User inputs concerning spin speeds and times were communicated to the microcontroller by a text-based serial terminal interface designed in house.

4.3.8 Microdevice fabrication

4.3.8.1 PMMA device

Each chip (4 cm x 4 cm x 1.5 mm) was made from two layers of PMMA and features a 12-well circular array of 5-mm-diameter circular wells. The PMMA (Astra Products,

Baldwin, NY) was cut using a VersaLASER system 3.50 (Universal Laser Systems, Scottsdale, AZ). The microwell features (designed in AutoCAD) were cut out of the top layer (1.0mm thick), which was then thermally bonded using established methods (36) to the bottom layer (0.5mm thick).

4.3.8.2 PeT devices

Microdevices used for HIA assays and chip PCR were fabricated with a poly(ethylene terephthalate) substrate in the form of overhead transparency sheets (TRANSNS; Filmsource, Maryland Heights, MO). Each device was composed of 5 layers. Layers 2 and 4 of the device were coated with toner (HPC-4127X black; Hewlett-Packard, Palo Alto, CA) by printing two layers of the toner on each side of the transparency at 600dpi, using a HPLaserJet 4000 printer (Hewlett-Packard, Palo Alto, CA). Layers 1 and 5 were treated with plasma oxidation (PE-75; Plasma Etch, Carson City, NV). The features of each layer of the microdevice were designed using CorelDraw software and cut from transparency sheets using a CO₂ laser cutter (VersaLASER VLS3.50; Universal Laser Systems, Scottsdale, AZ). The device was bonded using an office laminator (UltraLam 250B; Akiles, Mira Loma, CA), allowing the printer toner to serve as an adhesive agent. The layers were initially taped together to maintain alignment and subsequently inserted into the laminator several times to ensure sufficient bonding. Images of the HIA and PCR chips are shown in **Figure 4-5** and **Figure 4-11**, respectively.

4.3.9 Hybridization-induced Aggregation assays on a PMMA microdevice

Prior to HIA analysis, PCR products were thermally denatured (3 min at 95 °C) and placed immediately on ice in order to obtain single-stranded products. Each reaction took place in a 5mm (diameter) circular well, at a total volume of 20 μ L, composed of 18 μ L of hybridization buffer [200 mM KCl/10mM Tris (pH 7.5)], 1 μ L of each 3'- and 5'-probe-bound beads, and 1 μ L undiluted PCR product. After loading the reagents, the chip was placed on the DFA set-up, using a rotating magnet speed of 2,000 rpm and a vortexing speed of 130 rpm, for a total of 12 minutes.

4.3.10 Hybridization-induced Aggregation assays on a PeT microdevice

Prior to HIA analysis, PCR products were thermally denatured (3 min at 95 °C) and placed immediately on ice in order to obtain single-stranded products. Beads and sample (denatured PCR products) were diluted as detailed in 4.3.10.1 and 4.3.10.2. All dilutions were prepared in 1X hybridization buffer [200 mM KCl/10mM Tris (pH 7.5)] unless otherwise stated.

For all HIA assays on PeT, 3 μ L of beads (in the appropriate dilution) were pipetted into an inlet on the HIA chip. The chip was spun at 1200 rpm for 12 s to bring the beads into the chamber. 3 μ L of the sample was then pipetted through the same inlet, and the chip was spun at 2000 rpm for 12 s. The magnetic disc was lowered so that the magnets were positioned 0.5 cm above the microdevice. The magnetic disc was then spun as follows: clockwise at 200 rpm for 60 s, then 10 repeats of 30 s intervals clockwise then counterclockwise at 200 rpm.

4.3.10.1 HIA on PeT following conventional PCR

KRAS assay: beads (1:2), sample (1:2); *2 assay: beads (1:4), sample (1:2); *3 assay: beads (1:4), sample (1:2); 1173C>T assay: beads (1:4 in 100 mM KCl/5mM Tris/50% formamide), sample (1:2).

4.3.10.2 HIA on PeT following chip PCR

KRAS assay: beads (1:2), sample (1:1); *2 assay: beads (1:4), sample (1:4); *3 assay: beads (1:4), sample (1:1); 1173C>T assay: beads (1:4), sample (1:3).

4.3.11 Image analysis/data analysis

Following the aggregation assay, a digital photo of each chamber was taken using a T1i DSLR camera with MP-E 65 mm f/2.8 1–5× macro lens (Canon U.S.A., Inc., Lake Success, NY). The photo was cropped using ImageJ to include only the chamber and analyzed using a Kapur algorithm in the program Mathematica to derive a quantitative value (saturation) corresponding to the extent of aggregation.

4.4 Results and Discussion

4.4.1 Multiplex allele-specific PCR

Following optimization of the multiplex allele-specific PCR reaction, it was applied to a set of 6 patient DNA samples representing a diverse combination of genotypes. These samples were previously genotyped using the WARFGENO test (ARUP laboratories),

which relies on PCR and fluorescence monitoring to test for *CYP2C9* *2, *CYP2C9* *3, and *VKORC1* -1639G>A variants. Although this method tests for the *VKORC1* 1173C>T, the -1639G>A and 1173C>T alleles are in near perfect linkage disequilibrium and therefore can be reliably compared (29, 6). Indeed, the consistent relationship between -1639G>A and 1173C>T alleles across populations has prompted the common use of the 1173C>T SNP as a marker for -1639G>A (29).

Post-amplification analysis was performed using microchip electrophoresis (**Fig. 4-2**). For all samples, a 95 base pair (bp) product corresponding to the internal control (*KRAS*) was produced. For every sample containing a *CYP2C9* *2, *CYP2C9* *3, and *VKORC1* (1173C>T) mutation, electropherogram peaks corresponding to 209 bp, 286 bp, or 170 bp amplicons, respectively, are observed. No amplification of mutation-specific products is observed for wild-type genotypes. These results confirm complete allele-specificity of the multiplex PCR reaction.

4.4.2 Mutation detection with HIA

A pair of biotinylated probes conjugated to streptavidin-coated paramagnetic beads were used for the detection of each of the four possible products by PCR, corresponding to *KRAS*, *CYP2C9* *2, *CYP2C9* *3, and *VKORC1* (1173C>T). For each of the three allele-specific products, the sequences of the forward PCR primer and the reverse complement of the reverse PCR primer were used as the hybridization probes for detection. Thus, the detection is sequence-specific and provides an added level of specificity to the

genotyping assay. The design of the hybridization probes for the detection of the control (*KRAS*) amplicon was previously established and described in (26).

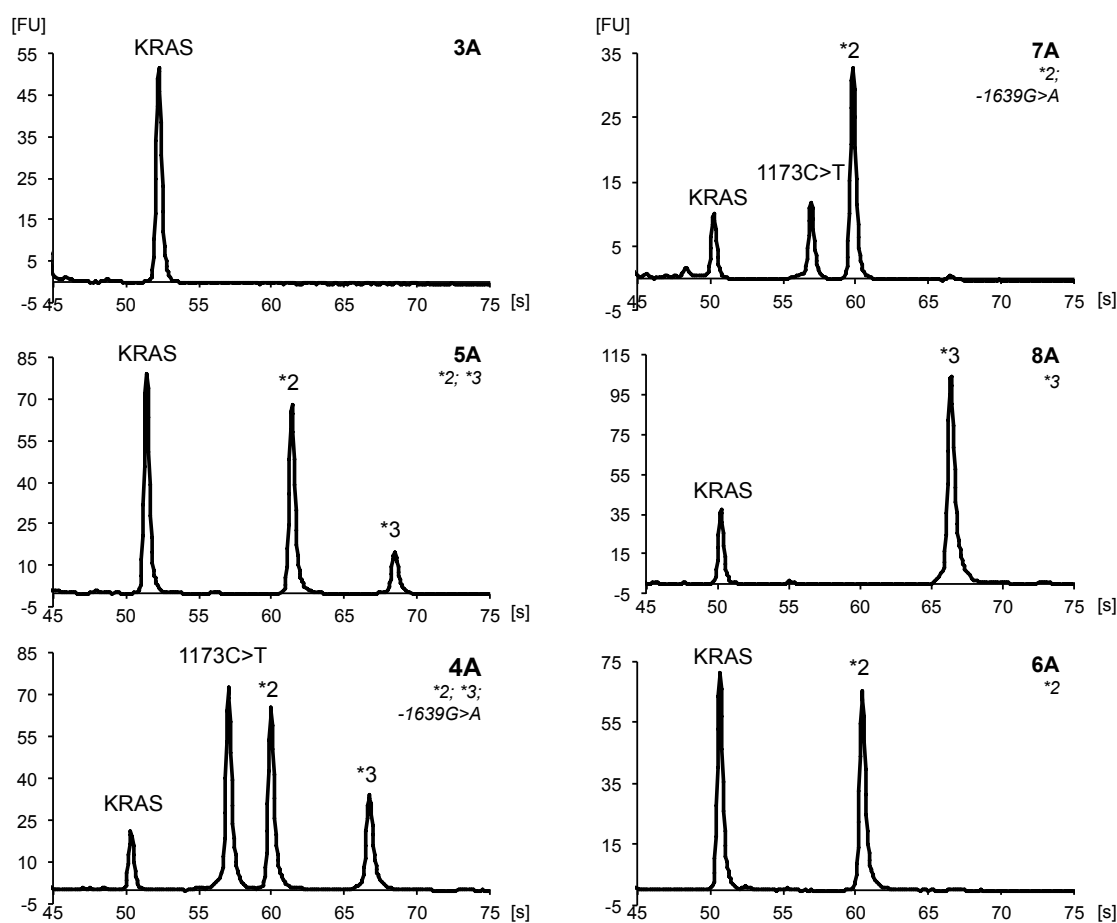


Figure 4-2. Validation of multiplex allele-specific PCR reaction for warfarin genotyping. The optimized PCR reaction was applied for six pre-genotyped patient samples and analyzed using microchip electrophoresis. Patient IDs associated with each sample, as well as the genotype as determined by the conventional assay, are displayed in the top right corner of each electropherogram. *KRAS* serves as the internal control to indicate successful PCR. The *KRAS* product (95 bp) is separated first, followed by *VKORC1* 1173C>T (170 bp), *CYP2C9* *2 (206 bp), and *CYP2C9* *3 (286 bp). These results confirm successful allele-specific amplification for all six samples.

4.4.2.1 DFA system

Initially, HIA-based detection was optimized on the DFA system (described in **Chapter 2**) with a PMMA multiwell device. In addition to buffer composition and reaction duration, a key parameter for achieving successful sequence-specific detection was the speed of the rotating magnetic field (RMF). When the RMF was too slow, the beads would be pulled to the side of the microwell, interfering with image analysis. At high RMF speeds, the variability in disperse samples was high. A mid-speed RMF was demonstrated to be optimal, as shown in **Figure 4-3**.

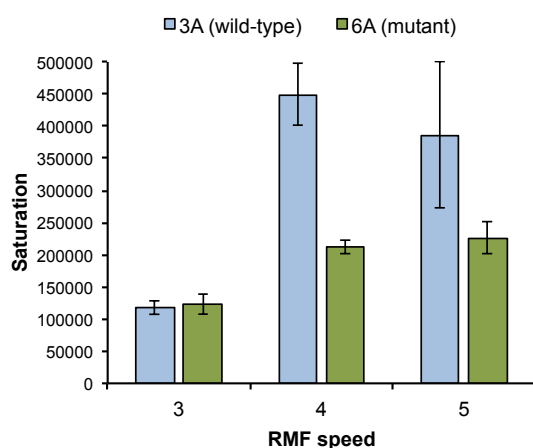


Figure 4-3. RMF speed optimization for HIA-based detection of CYP2C9*2. PCR products from samples with (6A) and without (3A) the CYP2C9 *2 mutation were tested in a series of assays with increasing RMF speeds. The RMF levels here represent relative speeds. At a low RMF speed (level 3), there is no discrimination between genotypes. At a high RMF speed (level 5), there is larger variation in less aggregated samples. Optimal results are obtained using a mid-speed RMF (level 4).

Under the optimized set of conditions, two pre-genotyped DNA samples (one with all three mutations and another with no mutations) were tested. As displayed in **Figure 4-4**, the results showed significant discrimination between positive (mutant) and negative (wild-type) genotypes based on aggregation, as quantified by image saturation. A saturation value of ~300,000 was consistently observed as an appropriate threshold value to objectively distinguish aggregated reactions from disperse reactions. This threshold

was plotted with the results in **Figure 4-4**, demonstrating the potential of using this assay and analysis method to determine sample genotypes.

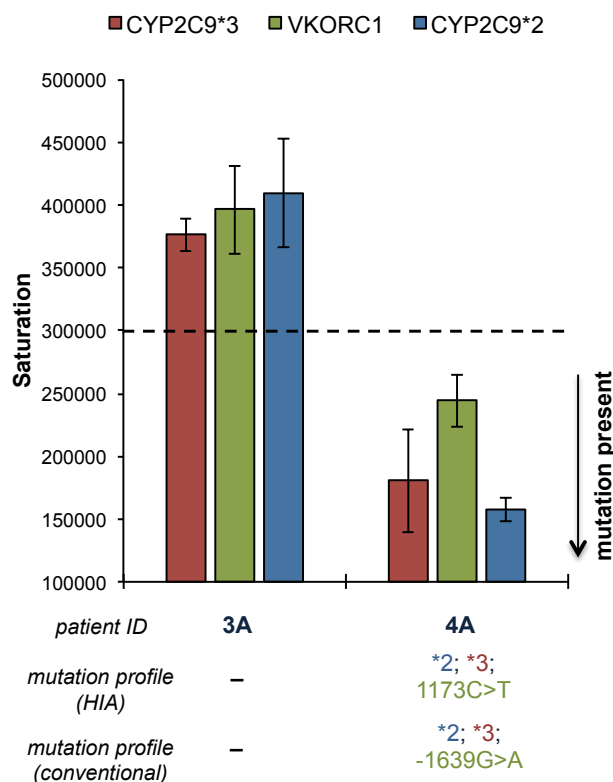


Figure 4-4. Warfarin genotyping assay on a PMMA microdevice with the DFA system. HIA assays for the detection of all three mutations were optimized such that all assays could be performed simultaneously on the same device. This is validated with two samples, one of which harbors all 3 mutations (4A) and the other of which harbors no mutations (3A). A threshold of 300,000 (saturation) was set to differentiate between mutant genotypes (<300,00 saturation) and wild-type genotypes (>300,00 saturation). Data points represent n=3.

4.4.2.2 PeT platform

While the results obtained using the DFA system were promising, it was determined that for this assay to have the greatest impact, HIA detection would eventually need to be integrated with the preceding PCR step. Although an integrated PCR and HIA

microdevice had previously been developed (27) (**Chapter 2**), the increased multiplexing capabilities of the PeT microdevice (30-plex) were particularly advantageous for the warfarin genotyping assay, since four HIA reactions needed to be performed for each sample (one reaction corresponding to each amplicon). Additionally, tangential work in the Landers lab showed encouraging results from sensitive PCR assays on a PeT chip. These factors provided impetus to transition the warfarin genotyping assay onto the PeT platform described here (**Fig. 4-5**).

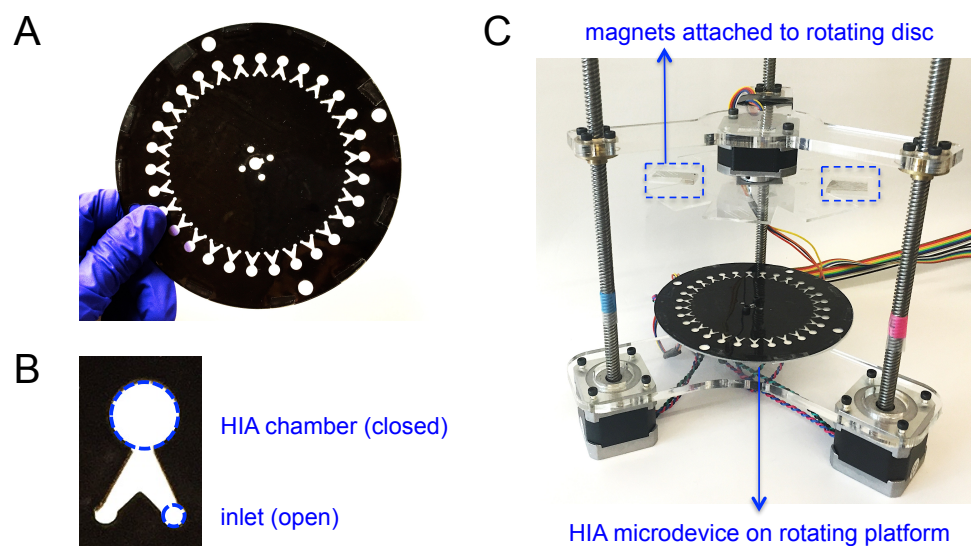


Figure 4-5. HIA microdevice and instrumentation. A) Photo: holding a HIA microdevice. Each microdevice features 30 HIA chambers. Around the border of the device are four open circles, which are used for alignment of the multiple layers of the device during fabrication. The features in the center of the microdevice are used to attach it to the rotating platform, as seen in (C). B) Zoomed-in photo of the microdevice architecture for a single HIA assay. Reagents are introduced through the inlet, and upon spinning of the device, they are loaded into the HIA chamber. C) Photo of the instrumentation set-up. The microdevice is fixed on a rotating platform. Above the chip is a bi-directional rotating disc with two magnets, which provides mixing of the magnetic beads during the HIA assay. The magnetic disc is attached to an adjustable z-axis, such that the height of the magnets above the microdevice can be varied as needed.

Bead aggregation assays have previously been demonstrated on PeT microdevices, using the microdevice design and instrumentation set-up applied in this work (see **Fig. 4-5**). The device supports high multiplexability, featuring 30 HIA chambers on one device. The instrumentation was engineered to include a spinning platform for the chip, which facilitates fluidic manipulation based on centrifugal force. Here, this was exploited to load the reagents into the HIA chambers. Above the chip is a rotating disc with attached magnets, which provides efficient mixing of the magnetic bead-bound probes with the sample during the HIA assay. Both the spinning chip platform and rotating magnetic disc are controlled by custom designed software that allows spin speed, direction, and duration to be programmed for the assay.

Adaptation of the HIA chemistry on this platform required optimization of the buffer composition, bead concentration, and sample (unpurified PCR product) concentration. These components were carefully considered and systematically adjusted, such that all four detection reactions could be performed simultaneously, on the same device and under the same conditions (i.e., rotating magnetic field speed and reaction time).

The reaction composition used in initial trials maintained the same mass of target and quantity of bead-bound probes as had been used in the HIA assay on the DFA system, even though the total volume of the reaction in a PeT chamber was reduced to 6 μ L (compared to 20 μ L in a PMMA well). To test the initial reaction composition, PCR product generated from a sample containing a mutation at all 3 loci, and PCR product generated from a sample containing no mutations were assayed. A negative PCR sample

(i.e., non-template control) was also tested, in order to investigate the specificity of the *KRAS* probes. As displayed in **Figure 4-6**, the results of *CYP2C9* *2, *CYP2C9* *3, and *VKORC1* (1173C>T) detection showed high variability and little discrimination between positive (mutant) and negative (wild-type) samples. The *KRAS* reactions, on the other hand, showed significant aggregation (low saturation) for the patient samples, and no aggregation (high saturation) in the non-template control; thus, it was determined that the *KRAS* reaction required no further optimization. The *KRAS* assay was repeated with additional samples to verify these results (**Fig. 4-6B**).

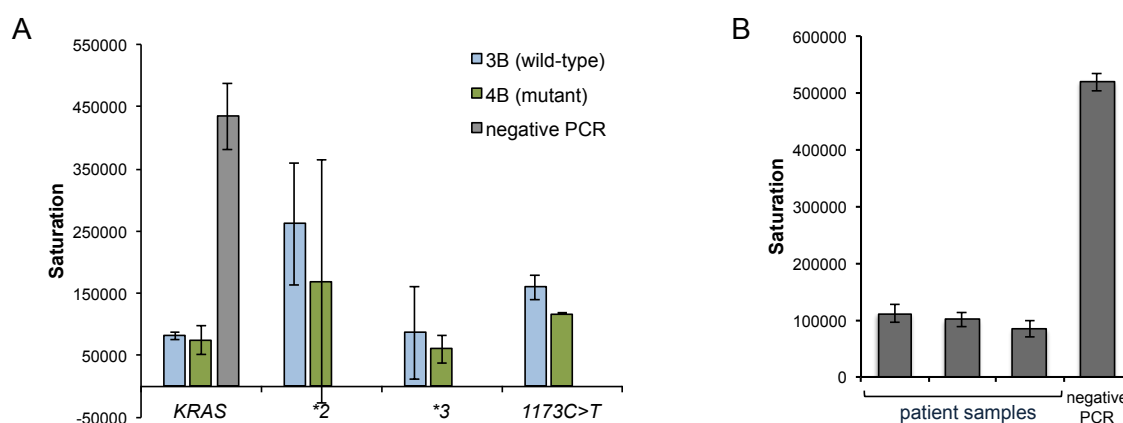


Figure 4-6. Initial HIA studies on a PeT device. A) Two patient samples - 4B [*CYP2C9**2, *CYP2C9* *3, *VKORC1* (1173C>T)] and 3B [no mutations] - were tested in initial reactions. A negative PCR sample was also tested to determine the specificity of *KRAS* (internal control) detection. *KRAS* detection was successful in initial studies, determined by high discrimination between positive samples and the negative PCR control sample. However, detection of the allele-specific amplicons had little discrimination between genotypes and high variability in results (as signified by large error bars). B) The *KRAS* assay was repeated with three patient samples for verification.

A key issue observed in initial trials was the lack of bead dispersion in negative samples, which was marked by lower saturation values relative to typical negative samples (e.g., the negative PCR control shown with *KRAS* detection in **Fig. 4-6**). In an attempt to reconcile this, all samples were diluted 1:2 in hybridization buffer, with the

driving hypothesis that less nucleic acid content would decrease non-specific interactions. The results of *CYP2C9* *2, *CYP2C9* *3, and *VKORC1* (1173C>T) detection reactions performed using the diluted PCR products are shown in **Figure 4-7A**. These results showed a substantial improvement for *CYP2C9* *3 detection, with high discrimination between positive and negative samples. *CYP2C9* *2 results were also improved, but the reproducibility (particularly in the negative sample) was not ideal. The results of *VKORC1* (1173C>T) detection showed a lack of discrimination due to non-specific bead aggregation in the negative (wild-type) sample, and this continued to be a trend observed in additional studies (**Fig. 4-7B**). To improve *VKORC1* (1173C>T) detection, formamide was added to the buffer, with the intention of reducing non-specific aggregation in the negative (wild-type) sample while maintaining high aggregation in the positive (mutant) sample. Indeed, it was determined that the addition of formamide at an optimal concentration allowed significant discrimination between samples with and without the

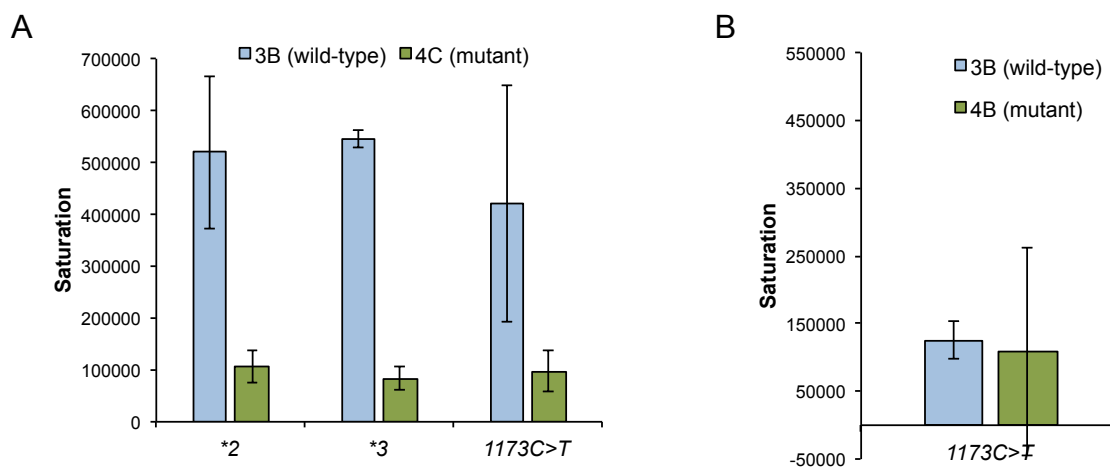


Figure 4-7. Exploring the effect of sample dilution on HLA results. A) Two patient samples - 4C [*CYP2C9**2, *CYP2C9* *3, *VKORC1* (1173C>T)] and 3B [no mutations] - were diluted 1:2 in hybridization buffer prior to HLA assays. The results of *CYP2C9* *2 and *CYP2C9* *3 detection assays were improved from initial studies. *VKORC1* (1173C>T) detection, however, continued to have little genotype discrimination and high variability in results (B).

VKORC1 (1173C>T) mutation (**Fig. 4-8**). Of note, the use of formamide in the hybridization buffer was effective only for *VKORC1* (1173C>T) detection; it was detrimental for the detection of *CYP2C9* *2 and *CYP2C9* *3, as shown in **Figure 4-8B**.

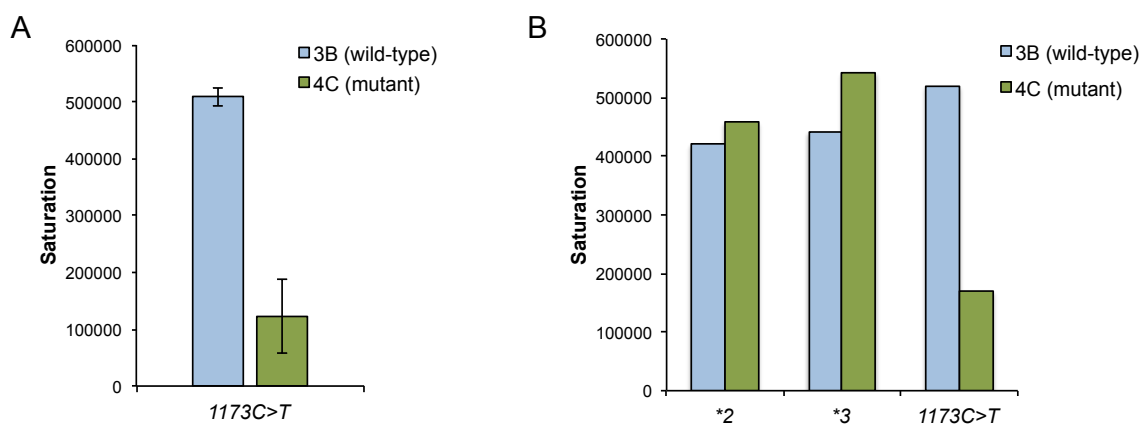


Figure 4-8. Effect of formamide added to the hybridization buffer. Two patient samples - 4C [*CYP2C9**2, *CYP2C9**3, *VKORC1* (1173C>T)] and 3B [no mutations] - were tested in HIA assays where the hybridization buffer consisted of 70% v/v formamide. A) Detection of *VKORC1* (1173C>T) shows optimal results with the formamide containing buffer. B) While detection of *VKORC1* (1173C>T) was optimal, the use of formamide was detrimental to genotype discrimination in *CYP2C9**2 and *CYP2C9**3 HIA assays.

Inconsistency in image analysis was believed to be the major source of low reproducibility in the results. Often, beads that had settled to the bottom of the chamber or were pulled to the top of the chamber around the meniscus of the reaction would be detected by image analysis as bead aggregation; however, visually, excess “clumped” beads could be distinguished from true bead aggregates. It was found that when the beads were diluted 1:4, the results were more robust and consistent, and image analysis was ultimately more reliable.

Following optimization, HIA assays for the detection of *CYP2C9* *2, *CYP2C9* *3, and *VKORC1* (1173C>T) were validated with three pre-genotyped DNA samples

(Fig. 4-9). To establish the reproducibility of each detection assay, three samples were analyzed for all three mutations in three replicates (i.e., on three separate chips). As shown in **Figure 4-9**, the results were highly reproducible, with inter-chip relative standard deviations mostly under 15%. To objectively differentiate an aggregated sample from a dispersed sample, a threshold value was established by averaging all saturation values from the HIA validation studies (**Fig. 4-9**). The threshold value, calculated to be 310,418 and rounded to 310,000 for simplicity, represents the midpoint between all aggregated and all dispersed samples in the validation studies. The threshold is plotted in **Figure 4-9** to demonstrate its utility in easily identifying samples with mutations as those that fall below the threshold value.

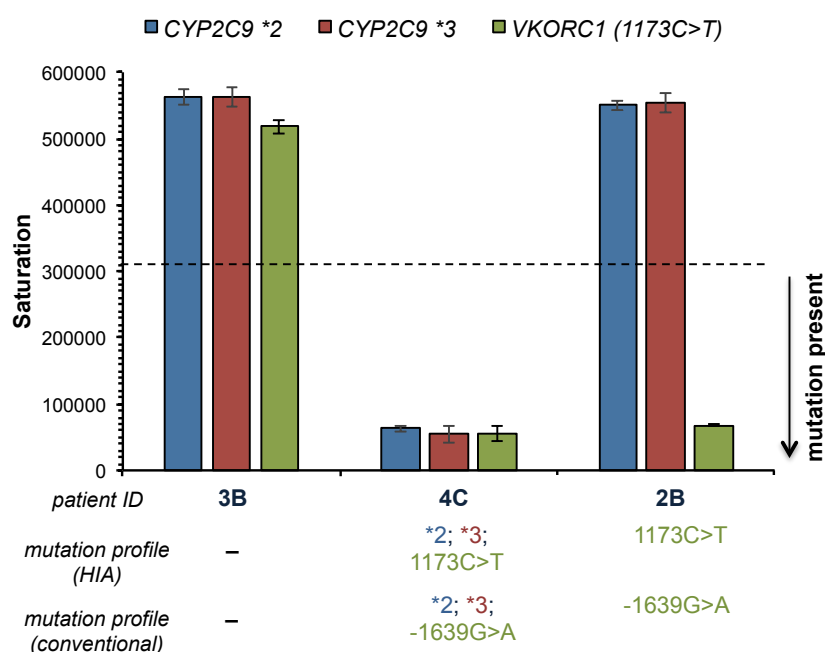


Figure 4-9. Optimized HIA-based warfarin genotyping assay on a PeT device. Three pre-genotyped samples were applied for HIA-based detection of CYP2C9*2, CYP2C9*3, and VKORC1 (1173C>T). All results represent the the average from 3 runs (i.e, 3 separate chips). By averaging all saturation values from these studies, a threshold value was obtained (310,000), which represents the midpoint between all aggregated and all dispersed samples. This threshold was used to objectively distinguish all mutant samples as those that fall below it.

4.4.3 Analysis of patient samples

Having established appropriate conditions for successful PCR and HIA detection, the complete genotyping assay was applied for the analysis of 23 patient samples. The established threshold value (310,000) was used to determine the mutation status at each locus. As seen in **Figure 4-10**, the use of the threshold allows simple genotype classification for each sample; any value that falls below the threshold is indicative of a mutation. The genotype of each sample as determined here was compared to the genotype reported based on the WARFGENO test (**Fig. 4-10** and **Table 4-2**). We report that the mutation profiles for all 23 patient samples obtained using our genotyping assay

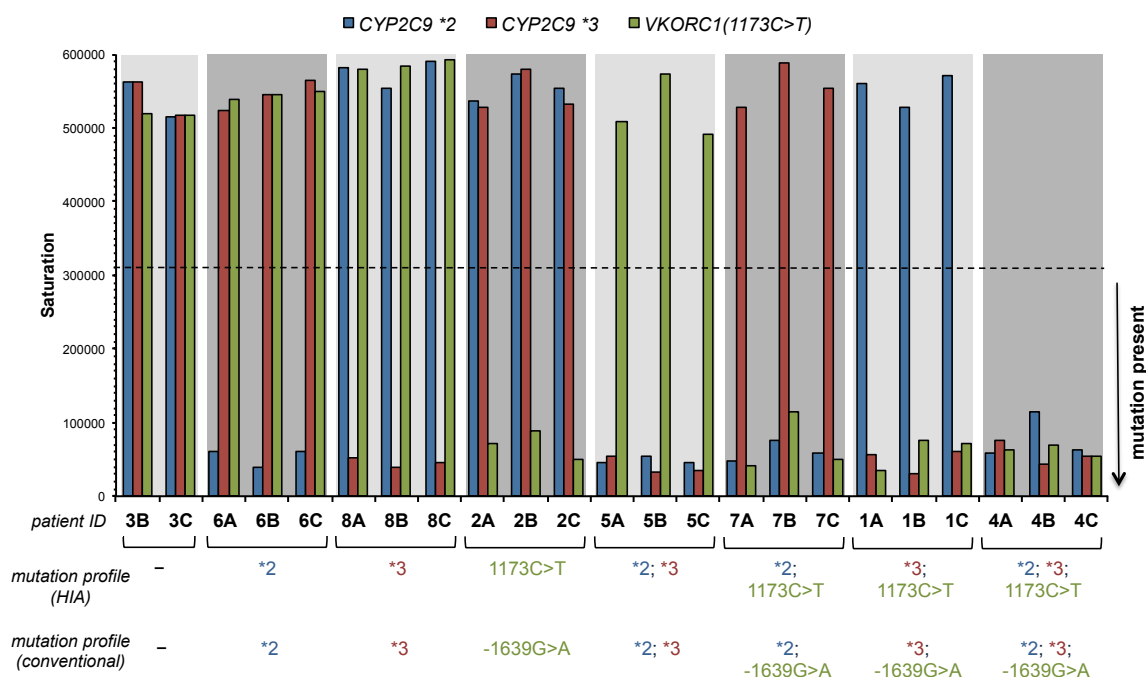


Figure 4-10. HIA-based genotyping of 23 patient samples. The optimized HIA assay was applied for the analysis of 23 pre-genotyped samples. The threshold value (310,000 saturation) was used to objectively determine sample genotypes, where a mutation was indicated by a saturation value below the threshold. The results of HIA-based genotyping were in 100% concordance with the conventionally-derived genotypes for all 23 samples.

matched the results of the WARFGENO test with perfect concordance. Of note, the 23 samples analyzed here represent all possible combinations of mutation profiles.

As reported in **Table 4-2**, all samples showed sufficient aggregation (i.e., saturation well above the threshold value) for *KRAS*, indicating successful PCR. Since the purpose of *KRAS* detection is to provide analytical quality control, we determined it was unnecessary to include *KRAS* results as a part of the mutation profile displayed in **Figure 4-10**.

	<i>KRAS</i>	<i>CYP2C9</i> *2			<i>CYP2C9</i> *3			<i>VKORC1</i>		
Patient ID	HIA result	HIA result	Mutation status (HIA)	Mutation status (conventional)	HIA result	Mutation status (HIA)	Mutation status (conventional)	HIA result	1173C>T Mutation status (HIA)	-1639G>A Mutation status (conventional)
1A	70657	559447	WT	WT	56584	MUT	MUT (homo)	35306	MUT	MUT (homo)
1B	59939	527161	WT	WT	29631	MUT	MUT (het)	76512	MUT	MUT (homo)
1C	145516	571634	WT	WT	60587	MUT	MUT (het)	71060	MUT	MUT (het)
2A	67816	535747	WT	WT	527046	WT	WT	71181	MUT	MUT (het)
2B	193413	573865	WT	WT	580443	WT	WT	89230	MUT	MUT (homo)
2C	112646	553185	WT	WT	533363	WT	WT	49390	MUT	MUT (het)
3B	100677	561849	WT	WT	562184	WT	WT	518379	WT	WT
3C	68920	515978	WT	WT	516363	WT	WT	516439	WT	WT
4A	72431	58946	MUT	MUT (het)	76139	MUT	MUT (het)	63106	MUT	MUT (homo)
4B	127903	115143	MUT	MUT (het)	43257	MUT	MUT (het)	68826	MUT	MUT (het)
4C	84202	62729	MUT	MUT (het)	54498	MUT	MUT (het)	55290	MUT	MUT (het)
5A	42822	45726	MUT	MUT (het)	53879	MUT	MUT (het)	509143	WT	WT
5B	70629	54471	MUT	MUT (het)	33766	MUT	MUT (het)	572715	WT	WT
5C	51413	45738	MUT	MUT (het)	33885	MUT	MUT (het)	490905	WT	WT
6A	114753	81826	MUT	MUT (het)	597814	WT	WT	557388	WT	WT
6B	44249	60688	MUT	MUT (het)	523468	WT	WT	538828	WT	WT
6C	42121	39494	MUT	MUT (het)	545783	WT	WT	544827	WT	WT
7A	45143	47085	MUT	MUT (het)	528937	WT	WT	42426	MUT	MUT (het)
7B	119695	74811	MUT	MUT (het)	587639	WT	WT	115265	MUT	MUT (het)
7C	64450	58801	MUT	MUT (het)	553244	WT	WT	49164	MUT	MUT (homo)
8A	35135	580857	WT	WT	52540	MUT	MUT (homo)	580695	WT	WT
8B	67897	554474	WT	WT	40247	MUT	MUT (het)	583727	WT	WT
8C	66503	591540	WT	WT	45963	MUT	MUT (het)	593232	WT	WT

Table 4-2. Genotyping results of 23 patient samples. All HIA results are reported in terms of saturation value. Using the threshold saturation value (310,000), genotypes were assigned as wild-type (WT; saturation<310,000) or mutant (MUT; saturation>310,000). The genotyping results as determined by the conventional test (WARFGENO, ARUP laboratories) are also reported. Mutant genotypes reported by the conventional test are distinguished as heterozygous (het) or homozygous (homo).

4.4.4 Transitioning PCR onto a PeT chip: establishing proof-of-concept for integration

With the goal of ultimately integrating PCR and HIA detection onto a single microdevice for sample-to-answer genotyping, we worked to adapt the multiplex allele-specific PCR reaction to be performed on a PeT chip (**Fig. 4-11**). An in-house engineered system, involving a pair of Peltier thermoelectric cooling modules clamped around the PCR reservoir, was used to provide efficient thermal cycling.

Key modifications of the conventional reaction for successful amplification on-chip included increased *Taq* polymerase, alteration of primer concentrations, and increased mass of template DNA. BSA, which has been shown to improve on-chip PCR efficiency (30), was also added to the reaction and had a positive effect on the amplification. Additionally, adjustments to the

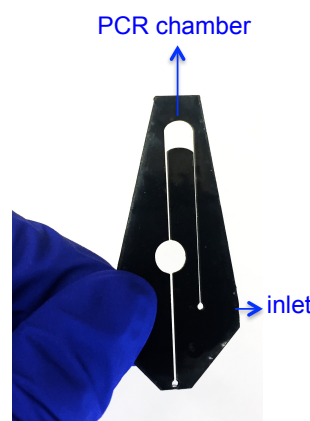


Figure 4-11. PeT microdevice for PCR. The inlet, where the PCR reaction is introduced onto the device, and the PCR chamber, are annotated. The circular chamber in the center of the device serves as a chamber for volume overflow.

thermal cycling parameters were made, including lower annealing temperatures, shorter holding times, and increased cycle number. Rapid temperature cycling was achieved using this platform (**Fig. 4-12**). Ultimately, successful multiplex allele-specific PCR was achieved on the chip, as determined using microchip electrophoresis for post-amplification analysis (**Fig. 4-13**), in ~40 minutes. While the amplicon concentrations were, in some cases (*3, in particular; refer to sample 8A in **Fig. 4-13**), lower than in conventional tube amplifications, this was determined not to be a problem for the

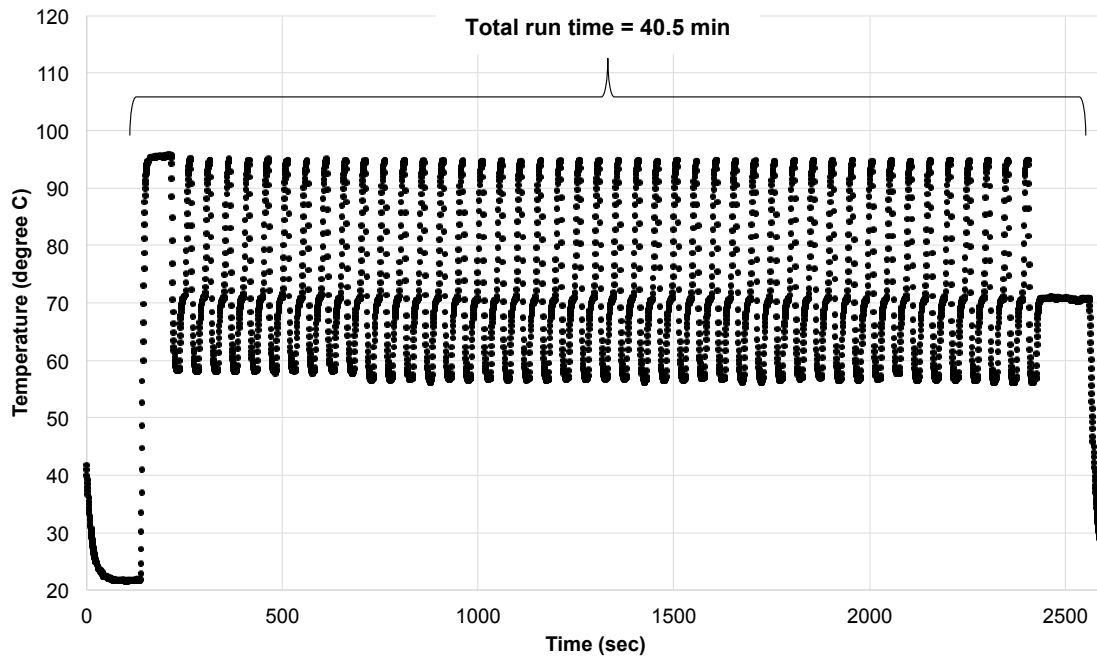


Figure 4-12. Thermal cycling profile for chip-based PCR. Temperature was monitored using a thermocouple in the PCR chamber. The complete PCR reaction on the device is completed in 40.5 minutes.

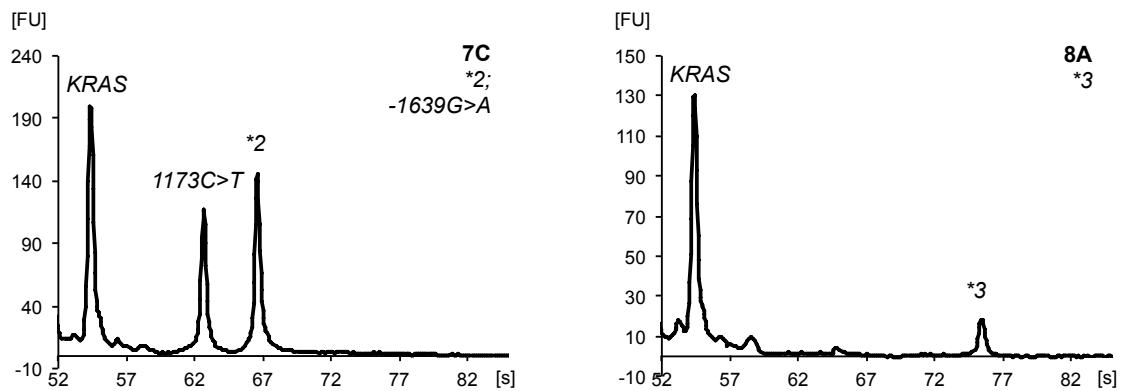


Figure 4-13. Validation of multiplex allele-specific PCR on a PeT microdevice. The optimized chip PCR reaction is demonstrated in two pre-genotyped patient samples and analyzed using microchip electrophoresis. Patient IDs associated with each sample, as well as the genotype as determined by the conventional assay, are displayed in the top right corner of each electropherogram. KRAS serves as the internal control to indicate successful PCR. The KRAS product (95 bp) is separated first, followed by VKORC1 (1173C>T) (170 bp), CYP2C9 *2 (206 bp), and CYP2C9 *3 (286 bp).

detection assay.

Following chip-based PCR, the product was taken out of the chip (using a micropipette to extract the product out through the inlet) and subsequently applied to a HIA detection chip for analysis. Based on the results of initial trials (**Fig. 4-14**), it was determined that re-optimization of the HIA assay parameters was required. This was unsurprising since samples derived from chip-based PCR have key differences from conventionally derived samples, including the presence of unreacted PCR master mix as a result of “dead volume” (excess volume in the channels on either side of the PCR

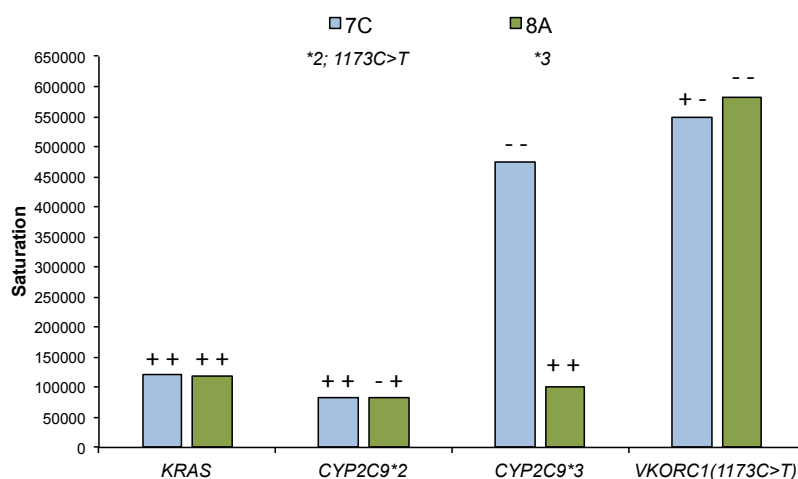


Figure 4-14. Initial HIA assays with PCR products generated on a PeT microdevice. Following chip PCR, products from sample 7A [CYP2C9*2; VKORC1 (1173C>T)] and 8A [CYP2C9 *3] were tested in HIA assays. Above each data point is a pair of symbols; the first symbol of the pair represents the theoretical result [positive (+) or negative (-)] based on the known genotype, and the second represents the experimental result [positive (+) or negative (-)]. Both samples (7A and 8A) should be positive for KRAS (+), and the HIA results are consistent with this, indicated by low saturation (+). This is also true for *2 detection in sample 7A and *3 detection in sample 8A, where the HIA results are consistent with the known mutant genotype (+ +). Correct results are also obtained for *3 detection in sample 7C and 1173C>T detection in sample 8A, where high saturation is achieved for wild-type genotypes (- -). However, the results of *2 detection in sample 8A are falsely positive (- +), and the results of 1173C>T detection in sample 7C are falsely negative (+ -). Thus, optimization of these reactions was necessary.

chamber). Key changes to the detection assays included higher dilutions of the samples as well as buffer modifications for VK detection.

The complete (albeit, not integrated) chip-based genotyping assay was demonstrated with three samples, chosen specifically to show wild-type and mutant genotypes for each of the alleles; included in this was a mutation-free sample. As shown in **Figure 4-15**, the mutation profiles of all three samples were correctly identified based on the results of the HIA assay.

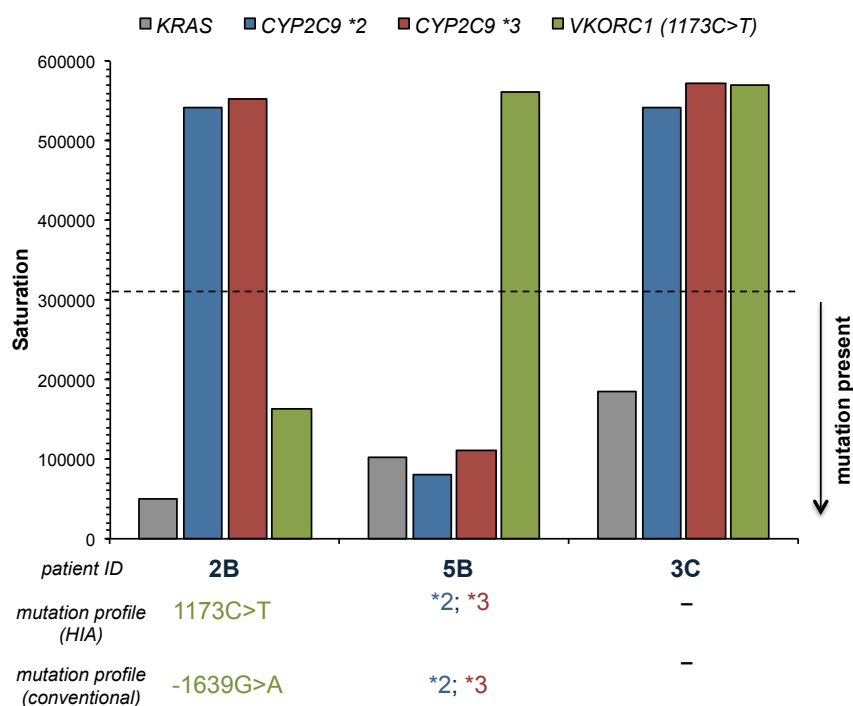


Figure 4-15. Optimized HIA-based warfarin genotyping assay from samples amplified on a PeT microdevice. Three pre-genotyped samples were applied for HIA-based detection of CYP2C9*2, CYP2C9*3, and VKORC1 (1173C>T) following amplification on a PeT microdevice. The previously determined threshold (310,000) was used to objectively distinguish all mutant samples as those that fall below it. The results for all three samples are consistent with the known genotypes.

4.5 Concluding Remarks

In this work, two powerful technologies – multiplex allele-specific PCR and HIA detection – were strategically combined to demonstrate a simple, rapid, and inexpensive approach to warfarin genotyping. This method was applied for the mutation analysis of 23 patient samples with a diverse combination of genotypes and show that our results are in 100% concordance with a validated test. Of note, this study represents the most extensive demonstration of clinical utility with the HIA method (i.e., largest patient sample size applied for HIA analysis).

Not only does this work represent the first instance of HIA on a PeT chip, it is also the first instance of showing multiplex allele-specific PCR for SNP detection on this microchip platform. By showing both chemistries (PCR and HIA) performed successfully on PeT chips, this work demonstrates the feasibility of their integration on a single chip. Further, because there are no additional analysis steps required following PCR (e.g., sample cleanup), the integration is anticipated to be relatively simple. An important feature of these PeT devices, and the primary motivation behind their use for this application, is the CD-like format, which allows simple fluid manipulation with centrifugal force. This provides an elegant platform for microfluidic integration, obviating the need for bulky and/or expensive peripheral equipment to drive fluid flow.

The intrinsic benefits of HIA technology contribute to key advantages of this genotyping method over standard methodologies for warfarin testing. First, the rapid nature of the assay allows a mutation profile comprising all 3 alleles affecting warfarin

sensitivity in approximately 15 minutes following PCR, and up to 7 patient samples can be analyzed on one chip in this timeframe. Using chip-based PCR, the time-to-result is ~50 minutes (following sample preparation). Another major advantage is the simplistic optical detection format, which requires only a camera and a laptop for analysis. This translates to simple operation as well as low cost. Further, it opens the possibility to eventually use a cell phone camera and associated “app” to perform the analysis.

A clear limitation of this method is the inability to differentiate between a heterozygous and homozygous mutant genotype. I point out that, for the purpose of demonstrating initial proof-of-principle with this platform, I intentionally maintained simplicity in the design. However, it is noteworthy that the T-ARMS assay from which the PCR reaction used here was adapted does provide bi-allelic amplification for heterozygous/homozygous differentiation (28). Thus, I purport the feasibility of using the full reaction, combined with HIA detection to generate a genotype that includes zygosity.

As the field of pharmacogenetics continues to gain momentum, it will be increasingly important to have the appropriate tools to translate this research into the clinic and allow it to drive better patient management decisions. By introducing a simple, inexpensive testing platform for rapid genotyping, this work represents a practical step in the shift towards a pharmacogenetic approach to patient care.

4.6 References

1. Shahin MH, Johnson JA. Clopidogrel and warfarin pharmacogenetic tests: what is the evidence for use in clinical practice? *Curr Opin Cardiol* 2013;28:305–14.
2. Budnitz DS, Pollock DA, Weidenbach KN, Mendelsohn AB, Schroeder TJ, Annest JL. National surveillance of emergency department visits for outpatient adverse drug events. *JAMA* 2006;296:1858–66.
3. Wysowski DK, Nourjah P, Swartz L. Bleeding complications with warfarin use: a prevalent adverse effect resulting in regulatory action. *Arch Intern Med* 2007;167:1414–19.
4. Jonas DE, McLeod HL. Genetic and clinical factors relating to warfarin dosing. *Trends Pharmacol Sci* 2009;30:375–86.
5. Higashi MK, Veenstra DL, Kondo LM, Wittkowsky AK, Srinouanprachanh SL, Farin FM et al. Association between CYP2C9 genetic variants and anticoagulation-related outcomes during warfarin therapy. *JAMA* 2002;287:1690–98.
6. Limdi NA, Wadelius M, Cavallari L, Eriksson N, Crawford DC, Lee MT et al. Warfarin pharmacogenetics: a single VKORC1 polymorphism is predictive of dose across 3 racial groups. *Blood* 2010;115:3827–34.
7. Gage BF, Lesko LJ. Pharmacogenetics of warfarin: regulatory, scientific, and clinical issues. *J Thromb Thrombolysis* 2008;25:45–51.

8. Klein TE, Altman RB, Eriksson N, Gage BF, Kimmel SE, Lee MT et al. Estimation of the warfarin dose with clinical and pharmacogenetic data. *N Engl J Med* 2009;360:753–64.
9. Finkelman BS, Gage BF, Johnson JA, Brensinger CM, Kimmel SE. Genetic warfarin dosing: tables versus algorithms. *J Am Coll Cardiol* 2011;57:612–18.
10. Shaw K, Amstutz U, Kim RB, Lesko LJ, Turgeon J, Michaud V et al. Clinical Practice Recommendations on Genetic Testing of CYP2C9 and VKORC1 Variants in Warfarin Therapy. *Ther Drug Monit* 2015;37:428–36.
11. Shi C, Yan W, Wang G, Wang F, Li Q, Lin N. Pharmacogenetics-Based versus Conventional Dosing of Warfarin: A Meta-Analysis of Randomized Controlled Trials. *PLoS One* 2015;10:e0144511.
12. Eckman MH, Rosand J, Greenberg SM, Gage BF. Cost-effectiveness of using pharmacogenetic information in warfarin dosing for patients with nonvalvular atrial fibrillation. *Ann Intern Med* 2009;150:73–83.
13. Epstein RS, Moyer TP, Aubert RE, O Kane DJ, Xia F, Verbrugge RR et al. Warfarin genotyping reduces hospitalization rates results from the MM-WES (Medco-Mayo Warfarin Effectiveness study). *J Am Coll Cardiol* 2010;55:2804–12.
14. Mega JL, Giugliano RP. Genotype-guided dosing of warfarin. *Clin Chem* 2014;60:920–22.
15. Johnson JA, Cavallari LH. Warfarin pharmacogenetics. *Trends Cardiovasc Med* 2015;25:33–41.

16. Kimmel SE. Warfarin pharmacogenomics: current best evidence. *J Thromb Haemost* 2015;13 Suppl 1:S266–71.
17. Nutescu EA, Drozda K, Bress AP, Galanter WL, Stevenson J, Stamos TD et al. Feasibility of implementing a comprehensive warfarin pharmacogenetics service. *Pharmacotherapy* 2013;33:1156–64.
18. Meckley LM, Neumann PJ. Personalized medicine: factors influencing reimbursement. *Health Policy* 2010;94:91–100.
19. Zhuang B, Han J, Xiang G, Gan W, Wang S, Wang D et al. A fully integrated and automated microsystem for rapid pharmacogenetic typing of multiple warfarin-related single-nucleotide polymorphisms. *Lab Chip* 2015;16:86–95.
20. Spohn G, Geisen C, Luxembourg B, Sittlinger K, Seifried E, Bonig H. Validation of a rapid and inexpensive allele-specific amplification (ASA)-PCR genotyping assay for vitamin K antagonist pharmacogenomics. *Mol Diagn Ther* 2011;15:13–19.
21. Zhu J, Zhang W, Li Y, Zhang W, Wang H, Zheng W et al. ARMS test for diagnosis of CYP2C9 and VKORC1 mutation in patients with pulmonary embolism in Han Chinese. *Pharmacogenomics* 2010;11:113–19.
22. Aomori T, Yamamoto K, Oguchi-Katayama A, Kawai Y, Ishidao T, Mitani Y et al. Rapid single-nucleotide polymorphism detection of cytochrome P450 (CYP2C9) and vitamin K epoxide reductase (VKORC1) genes for the warfarin dose adjustment by the SMart-amplification process version 2. *Clin Chem* 2009;55:804–12.

23. Sebastian T, Cooney CG, Parker J, Qu P, Perov A, Golova JB et al. Integrated amplification microarray system in a lateral flow cell for warfarin genotyping from saliva. *Clin Chim Acta* 2014;429:198–205.
24. Maurice CB, Barua PK, Simses D, Smith P, Howe JG, Stack G. Comparison of assay systems for warfarin-related CYP2C9 and VKORC1 genotyping. *Clin Chim Acta* 2010;411:947–54.
25. Strachan BC, Sloane HS, Lee JC, Leslie DC, Landers JP. Investigation of the DNA target design parameters for effective hybridization-induced aggregation of particles for the sequence-specific detection of DNA. *Analyst* 2015;140:2008–15.
26. Sloane HS, Kelly KA, Landers JP. Rapid KRAS Mutation Detection via Hybridization-Induced Aggregation of Microbeads. *Anal Chem* 2015;87:10275–82.
27. Strachan BC, Sloane HS, Houpt E, Lee JC, Miranian DC, Li J et al. A simple integrated microfluidic device for the multiplexed fluorescence-free detection of *Salmonella enterica*. *Analyst* 2016;141:947–55.
28. Poe BL, Haverstick DM, Landers JP. Warfarin genotyping in a single PCR reaction for microchip electrophoresis. *Clin Chem* 2012;58:725–31.
29. Owen RP, Gong L, Sagreiya H, Klein TE, Altman RB. VKORC1 pharmacogenomics summary. *Pharmacogenet Genomics* 2010;20:642–44.
30. Zhang C, Xing D. Miniaturized PCR chips for nucleic acid amplification and analysis: latest advances and future trends. *Nucleic Acids Res* 2007;35:4223–37.

5 Final Remarks

5.1 Summary

The work presented in this dissertation demonstrates the promise and potential of nucleic acid analysis via optical detection of bead aggregation. In **Chapter 2**, “dual force aggregation” (DFA) instrumentation was engineered to maximize the utility of bead aggregation assays [i.e., Chaotrope Driven Aggregation (CDA) for genomic DNA quantification and Hybridization-Induced Aggregation (HIA) for sequence-specific DNA detection]. The DFA platform allowed multiplex analysis and facilitated efficient interaction of the DNA sample and magnetic beads for optimal results. In addition to the sensitive quantification of genomic DNA, the DFA instrumentation was integral to the development of sequence-specific assays with clinical value described in **Chapters 3** and **4**. **Chapter 2** also presented the development of a microdevice for integrated PCR amplification and HIA detection, representing a promising step forward in the development of a system with sample-in-answer-out capabilities.

In a novel extension of the HIA method, **Chapter 3** described the detection of single base mutations in a gene segment, and specifically, the detection of *KRAS*

mutations in lung and colorectal cancers. Importantly, it was shown that the HIA methodology was capable of revealing a single base mismatch in a gene segment using only a digital photo of the reaction well for analysis. This is a substantial analytical achievement that presents a vast advantage over other genotyping technologies that typically require highly-sophisticated detection methods, often involving fluorescent labels and complex optics to achieve the sensitivity required to detect a single base change.

The clinical utility of HIA technology was demonstrated further in **Chapter 4** with the development of a rapid genotyping assay for warfarin dosing. Here, HIA detection was combined with a multiplex allele-specific PCR reaction. Both the HIA detection and the PCR reaction were successfully transitioned onto a PeT microdevice, showing the potential for integration. The application of HIA on multiple platforms (i.e., PMMA chip with DFA instrumentation and PeT chip with a centrifugal platform) demonstrates the versatility and robust nature of this technology.

Ultimately, this work provides evidence that simple, rapid, and inexpensive analysis can be achieved without compromising the analytical performance necessary for clinical utility. This has important implications for the potential to integrate genetic

testing into our clinical paradigm in a practical format such that the benefits of precision medicine can be realized.

5.2 Future Prospects

The successful demonstration of HIA-based DNA detection with single base mutation discrimination capabilities suggests that the analysis of any gene segment could be possible with this technique, given the appropriate assay design and experimental conditions. As such, the potential applications of HIA analysis in molecular diagnostics are overwhelmingly extensive. An important subfield of molecular diagnostics where HIA might be particularly valuable is infectious disease diagnostics. This encompasses the detection of pathogens as well as associated gene markers for antimicrobial resistance and virulence (1). For applications such as this, speed and translatability to resource-limited settings is crucial and, thus, the HIA technology would be a well-suited analytical tool.

To ultimately have the greatest impact at the point-of-care, HIA will need to be integrated in a testing format with sample-in-answer-out capabilities. This will allow an

actionable result to be delivered directly following the input of a raw sample with little to no effort required by the user. The work presented in this dissertation where on-chip PCR amplification was followed immediately by HIA detection in both a sequential (**Chapter 4**) and integrated (**Chapter 2**) format suggest promise for the realization of a fully automated HIA detection platform.

Having shown the value of bead aggregation for nucleic acid-based molecular diagnostics, future work could involve the extrapolation of this approach for other important analytes. In particular, aggregation assays using antibody-conjugated beads could provide a useful tool for protein detection. Like nucleic acids, proteins represent an enormous class of biomarkers with substantial clinical value.

Additionally, antibody-conjugated beads could facilitate the immunoisolation of cells or extracellular vesicles based on its particular molecular profile. Specifically, exosomes (nanometer-sized extracellular vesicles) are ideal candidates for facilitating cancer diagnosis, prognosis, and prediction of therapeutic response. First, they are readily accessible in nearly all body fluids and thus can be tested for in a non-invasive manner, and second, they originate within the tumor cells themselves, and therefore their cargo is a direct reflection of the pathological state of the host tumor (2). The mere fact

that exosome production is increased in cancer allows for exosome quantification to be useful for cancer detection and assessment of disease progression. Indeed, studies have demonstrated elevated levels of exosomes in the plasma of cancer patients as compared to control groups (3) and even noted a positive correlation between the abundance of tumor exosomes and cancer stage in the case of ovarian cancer (4). Therefore, a simple method for determining the relative abundance of exosomes in a sample could serve as a powerful diagnostic tool.

Currently, nanoparticle tracking analysis is required for exosome characterization. Alternatively, total protein quantification or the detection of exosome specific protein markers (typically with a Western blot) can be performed to indirectly determine exosome abundance. Prior to characterization, exosomes must be isolated. The standard method for the isolation of exosomes in a biological sample is differential centrifugation, which involves a series of sequential centrifugations, including lengthy, high-speed ultracentrifugation steps (requiring forces of 100,000xg) to sediment the small (~30-100 nm), membrane-bound vesicles (5). The emergence of isolation reagents (e.g., ExoQuick, System Biosciences) has simplified this process somewhat, reducing the overall labor intensity (6,7); however, this approach still involves a time-consuming

procedure (including overnight incubation) and is limited by the high cost of the isolation reagent itself. An alternative method for exosome isolation is immunoaffinity capture, which takes advantage of exosome-specific surface antigens to isolate only the subset of particles expressing that particular marker. Magnetic beads functionalized with an exosome-specific antibody, then, can be used to selectively capture exosomes directly from serum samples (8). At the macro-scale, efficient immunocapture requires a long incubation period (typically many hours). The transition of the assay onto a microscale platform such as those described in this dissertation could allow a significant reduction in the incubation period, increasing the overall speed of analysis. Furthermore, it is possible that in addition to exosome capture, the interaction of antibody-conjugated beads with exosomes could induce bead aggregation in a manner analogous to HIA, facilitating exosome characterization through simple optical analysis.

Only recently has there been effort in the field to develop innovative technologies for exosome analysis that exploit the advantages of microfluidics (9-12). Thus, this is an area that is ripe for development and holds enormous value for ongoing exosome research and future diagnostic strategies.

Overall, bead aggregation assays hold a great deal of potential to deliver important molecular analyses in a manner that is rapid, inexpensive, and simple to execute.

5.3 References

1. Picard FJ, Bergeron MG. *Drug Discov. Today*. 2002;7:1092-1101.
2. Brinton LT, Sloane HS, Kester M, Kelly KA. Formation and role of exosomes in cancer. *Cell Mol Life Sci*. 2014
3. Rabinowits G, Gercel-Taylor C, Day JM, Taylor DD, Kloecker GH. Exosomal microRNA: a diagnostic marker for lung cancer. *Clin Lung Cancer*. 2009;10:42-6.
4. Taylor DD, Gercel-Taylor C. MicroRNA signatures of tumor-derived exosomes as diagnostic biomarkers of ovarian cancer. *Gynecol Oncol*. 2008;110:13-21.
5. Thery C, Amigorena S, Raposo G, Clayton A. Isolation and characterization of exosomes from cell culture supernatants and biological fluids. *Curr Protoc Cell Biol*. 2006;Chapter 3:Unit 3.22.
6. Taylor DD, Zacharias W, Gercel-Taylor C. Exosome isolation for proteomic analyses and RNA profiling. *Methods Mol Biol*. 2011;728:235-46.

7. Rekker K, Saare M, Roost AM, Kubo AL, Zarovni N, Chiesi A, Salumets A, Peters M. Comparison of serum exosome isolation methods for microRNA profiling. *Clin Biochem.* 2014;47:135-8.
8. Tauro BJ, Greening DW, Mathias RA, Ji H, Mathivanan S, Scott AM, Simpson RJ. Comparison of ultracentrifugation, density gradient separation, and immunoaffinity capture methods for isolating human colon cancer cell line LIM1863-derived exosomes. *Methods.* 2012;56:293-304.
9. He M, Crow J, Roth M, Zeng Y, Godwin AK. Integrated immunoisolation and protein analysis of circulating exosomes using microfluidic technology. *Lab Chip.* 2014;14:3773-80.
10. Kanwar SS, Dunlay CJ, Simeone DM, Negrath S. Microfluidic device (ExoChip) for on-chip isolation, quantification and characterization of circulating exosomes. *Lab Chip.* 2014;14:1891-900.
11. Zhang P, He M, Zeng Y. Ultrasensitive microfluidic analysis of circulating exosomes using a nanostructured graphene oxide/polydopamine coating. *Lab Chip.* 2016
12. Zhao Z, Yang Y, Zeng Y, He M. A microfluidic ExoSearch chip for multiplexed exosome detection towards blood-based ovarian cancer diagnosis. *Lab Chip.* 2016;16:489-96.